Design of Dataflow Monitoring and Searches for $B \to \omega\gamma$, $B \to \phi\gamma$ and $B \to \phi K^0_S\gamma$ at BABAR

James Swain

Thesis submitted for the degree of Doctor of Philosophy

The University of Edinburgh

Si tacuisses, philosophus mansisses [1]

Abstract

In May 2003 PEP-II achieved instantaneous luminosities in excess of $6 \times 10^{33}\,\mathrm{cm}^{-2}\mathrm{s}^{-1}$, twice the design luminosity. To permit *BABAR* to operate in this challenging environment, development work on the data acquisition system continued after detector commissioning. A vital part of this process is understanding the performance of the data acquisition system. Considerable effort was invested in the design and implementation of an application capable of collecting performance statistics from hundreds of CPUs in the data acquisition system during data collection. The monitoring application and some examples of its operation are presented in this thesis.

Also presented here are the searches for the exclusive radiative one-loop decays, $B \to \omega\gamma$, $B \to \phi\gamma$ and $B^0 \to \phi K_S^0\gamma$, using a sample of 89 million $B\overline{B}$ events. No significant signal is seen in any of the channels. Upper limits on the branching ratios, $\mathcal{B}$, were found to be $\mathcal{B}(B \to \omega\gamma) < 3.0 \times 10^{-6}$, $\mathcal{B}(B \to \phi\gamma) < 2.9 \times 10^{-6}$, and $\mathcal{B}\left(B^0 \to \phi K_S^0\gamma\right) < 3.8 \times 10^{-6}$, at the 90% confidence level.

Declaration

This work represents the efforts of many members of the *BABAR* collaboration at SLAC, in California. I have been an integral part of the small team of people who maintain and expand the data collection systems of the *BABAR* detector. I have received guidance from several collaborators involved in the study of rare radiative one-loop decays at *BABAR*. The writing of this thesis is entirely my own work.

Acknowledgements

As with any major endeavour, this thesis was not created in a vacuum but rather in a fertile academic environment with the assistance of many people. I cannot hope to mention every person who has played a part but some individuals are worthy of specific mention.

The continuous presence, whether physical or mental, in the life of any Ph.D. student is that of his supervisor. Steve Playfer has been instrumental in shaping my experience as a postgraduate student. I am most grateful for his guidance and insights throughout the writing of this thesis and during the execution of the analyses that it describes.

Almost as omnipresent has been Philip Clark, a former postgraduate student, and now lecturer, at the University of Edinburgh. Throughout my PhD he has been an invaluable source of information and advice, as well as a good friend.

During the time I worked for the *BABAR* online dataflow group Chris O'Grady assumed the rôle of mentor and introduced me to the disciplined world of real-time programming. He and Amedeo Perazzo were directly responsible for allowing me to attend the Computing in High Energy and Nuclear Physics Conference (2001) in Beijing. Without them there would have been no monitoring application to write a paper on, and thus no paper to present.

Whilst serving as Deputy Run-Coordinator for the *BABAR* collaboration I had the opportunity to work with a wide range of collaboration members and PEP-II personnel. In particular I am grateful to Eli Rosenberg, Francois LeDiberder, Livio Piemontese, and William Wisniewski who all served as Run-Coordinators during my time as deputy. I am sure that their individual and distinct managerial styles will stay with me for a very long time to come. I am also grateful to Steve Sekula for doing an excellent job during those six months. These five people, along with the other denizens of IR-2 made a stressful job genuinely enjoyable.

The analyses presented in this thesis have benefited from the input of a wide range of collaborators. Dieter Best, Mark Convery and Hirohisa Tanaka, from the Radiative Penguin AWG provided the foundations upon which the analysis is based. Francesca Di Lodovico and Jane Tinslay advised and assisted me with all manner of issues whilst serving the University of Edinburgh as postdoctoral researchers. Jane also agreed to read through this thesis and provided valuable feedback.

Even with all of these people, I doubt I would have completed this Ph.D. without the love and encouragement of my parents, Jennie and Grant, and my partner, Rebecca.

Finally, I am grateful to the Particle Physics and Astronomy Research Council of the United Kingdom for the support provided for the first three years of my graduate studies.

Contents

List of Tables

List of Figures

1

Introduction

CP violation was observed in the neutral Kaon system by Christenson, Cronin, Fitch, and Turlay in 1964 [2]. More recently, the *BABAR* collaboration observed CP violation in the B meson system in 2001 [3]. CP violation is important because it is one of the ingredients required to generate the observed matter anti-matter asymmetry in the universe, the other ingredients being baryon-number violation, C violation and a departure from thermal equilibrium [5]. CP violation in the three-generation Standard Model is well understood, but it has been known for some time that it is impossible to generate a baryon asymmetry of the observed magnitude from Standard Model CP violation alone. New sources of CP violation beyond the Standard Model may be instrumental in explaining the observed asymmetry [6].

The *BABAR* collaboration was formed to systematically study CP violation in the B meson system. The collaboration aims to measure and over-constrain the parameters governing the weak decay process. If these parameters are found to have values that are inconsistent with the Standard Model, or if there is no single set of values consistent with all the measurements, then the existence of physics beyond the Standard Model is confirmed.

The *BABAR* detector is situated at the Stanford Linear Accelerator Center, California, where collisions are provided by PEP-II. By May 2003 PEP-II was achieving instantaneous luminosities in excess of $6 \times 10^{33}\,\mathrm{cm}^{-2}\mathrm{s}^{-1}$, twice the design luminosity. High luminosity coupled with long periods of uninterrupted running for PEP-II and *BABAR* has produced a sizable dataset, permitting old measurements to be repeated with much greater precision, and making the observation of rare decay modes feasible for the first time. However, the increasing luminosities make increasing demands on the *BABAR* data acquisition systems.

To permit upgrades to the data acquisition system to be planned, and to ensure the system is performing as expected, some form of monitoring is required. Three members of the *BABAR* Online Dataflow group spent approximately one year designing and implementing an application capable of monitoring the hundreds of CPUs of the data acquisition system in real-time during data taking. This thesis describes the design of this application, and gives some examples of its usage.

Following this, the searches for three rare radiative one-loop decay modes are presented. These decays are examples of Flavour Changing Neutral Currents, coupling the b quark to the s or d quark. The low branching ratios of these channels, of the order 10^{-6}, means that a large data set is needed to perform a meaningful study. These modes are all hitherto unseen, but are potential sources of both direct and indirect CP violation, as well as providing insights of their own into New Physics and super-symmetry.

This thesis will begin by briefly describing the *BABAR* detector, before moving on to detail the design of the data acquisition system monitoring application. The study of radiative one-loop B meson decays will be motivated by demonstrating the calculation of some Cabbibo-Kobayashi-Maskawa matrix elements from the branching fractions of these decays. Finally, the searches for three radiative one-loop B meson decays will be presented.

2

BaBar and the B Factory

2.1 Introduction

A description of the *BABAR* detector and an evaluation of its performance has been published in *Nucl. Instr. and Methods* [7] and the full details of the design are in the Technical Design Report [8]. Similar documents exist describing PEP-II [10, 11]. Presented here is a summary of the detector components necessary for understanding the rest of this thesis.

2.2 PEP-II

PEP-II is called a B Factory since it is designed to produce B mesons at a high rate, continuously, over a long period of time. The integrated luminosities for the best periods of data-taking[1] are presented in table 2-1. By the summer of 2002 *BABAR* had collected 82 fb^{-1} of data on the $\Upsilon(4S)$ resonance and 9.1 fb^{-1} of data taken *off-peak*, at an energy below the $\Upsilon(4S)$ threshold. This is the data set used for the analyses presented later in this thesis.

Time period	Integrated Luminosity (pb^{-1})
shift (8 hrs)	116
day	346
week	1967
month	7041

Table 2-1. *BABAR luminosity records.*

When PEP-II is running on-peak, electrons and positrons are collided with an energy of 10.58 GeV, in the centre of mass frame. The dominant process is $e^+e^- \rightarrow e^+e^-$, *i.e.* Bhabha scattering, which produces a distinctive signature of two stiff back-to-back tracks in the trigger system. The *BABAR* level 1 hardware trigger (see section 3.2.2) is designed to prescale Bhabha triggers, reducing the total number of these triggers while retaining some fraction for detector studies. The Bhabha prescale factor can be altered as the instantaneous luminosity increases, to keep the number of Bhabhas collected per unit time relatively constant.

[1] Records as of March 22, 2003

When an $\Upsilon(4S)$ is produced it decays almost exclusively to a $B\overline{B}$ pair ($> 96\%$) [9]. The mass of the $\Upsilon(4S)$ is so close to the $B\overline{B}$ production threshold that the B mesons are nearly at rest in the centre of mass frame, and their subsequent decays will produce an isotropic distribution of daughter particles. The decay products of other processes will have significant momentum in the centre of mass frame and will tend to result in jet-like distributions of final state particles. This behaviour is very useful for distinguishing background events from signal events.

2.2.1 An Asymmetric Collider

This thesis describes measurements of the Branching Fractions of rare decay, but *BABAR* was designed to measure CP violation in the B meson system by measuring time-dependent neutral B meson mixing. In a symmetric collider, where the centre of mass frame and the laboratory frame are the same, it is very difficult to distinguish the B decay vertices. In the PEP-II collider the B meson pair is boosted in the laboratory frame, making the difference in the lifetime of the mesons equivalent to a measurable distance inside the *BABAR* detector. PEP-II has a high energy ring containing electrons with energy 9 GeV and a low energy ring containing positrons with energy 3.1 GeV which gives the $\Upsilon(4S)$ resonance a boost of $\beta\gamma = 0.56$ in the laboratory frame. The asymmetry in the beam energies is reflected in the geometry of the interaction region; the interaction point is off-centre with respect to the *BABAR* detector. This boost is not necessary for rare decay studies, although the separation may make it easier to distinguish between the decay products from the interesting B meson and its partner.

2.2.2 Machine Backgrounds

During the first year of running, three primary causes of steady state PEP-II machine background were identified.

1. Synchrotron radiation generated by the bending magnets and focusing quadrupole in the incoming beam lines.
2. Beam-gas events (interactions between beam particles and residual gas in the rings), which are the primary source of radiation damage.
3. Electromagnetic shower debris, which is dominated by energy degraded positrons and electrons from radiative Bhabha scattering striking machine components close to the interaction point.

The last of these scales with instantaneous luminosity to become dominant at higher luminosities.

Although the accelerator physicists work hard to reduce the background it can never be eliminated, so an acceptable background rate must be determined. The input factors to this decision are (in order of decreasing importance)

1. Radiation hardness of the Silicon Vertex Tracker and Electromagnetic Calorimeter (see sections 2.3.1 and 2.3.4).
2. Drift Chamber currents (see section 2.3.2).
3. Level 1 trigger rates and the occupancies of the remaining subsystems.

2.3 The *BABAR* Detector

The side-on schematic of the *BABAR* detector in figure 2-1 shows five sub-detectors and a magnet. From the interaction point (IP) outward these are the Silicon Vertex Tracker (SVT), the Drift Chamber (DCH), the Detector of Internally Reflected Čerenkov Radiation (DRC or DIRC), the Electromagnetic Calorimeter (EMC), the Super-conducting Solenoid and the Instrumented Flux Return (IFR). These subsystems are described in the following sections, and their importance to the study of radiative penguin decays is indicated.

2.3.1 The Silicon Vertex Tracker

To permit useful measurements of $B^0\overline{B}^0$ mixing, it is necessary to measure the decay vertices with high precision. The *BABAR* SVT has a position resolution of better than 50 μm, improving to $< 20\,\mu$m in the center of the innermost layers. For particles with transverse momentum less than 100 MeV/c the SVT also provides the only tracking information. The vertex information has been successfully used in studies of radiative penguin decays to reduce backgrounds, but this technique has not been used in the analyses presented in this thesis.

2.3.1.1 Construction

Side and end view schematics of the SVT are shown in figures 2-2 and 2-3. The SVT is formed from five layers of double sided silicon detectors with 90° stereo. These are supported on kevlar ribs mounted on the end cones located forward and backward of the IP. This assembly is then enclosed in a carbon fibre support tube. Readout is performed by radiation hard integrated circuits (ICs). The ICs are mounted on hybrid circuits providing power and communication with the Data Acquisition System. These circuits also link the ICs to the cooling system. The SVT is sensitive to variations in temperature and so must be cooled whenever the readout electronics are on.

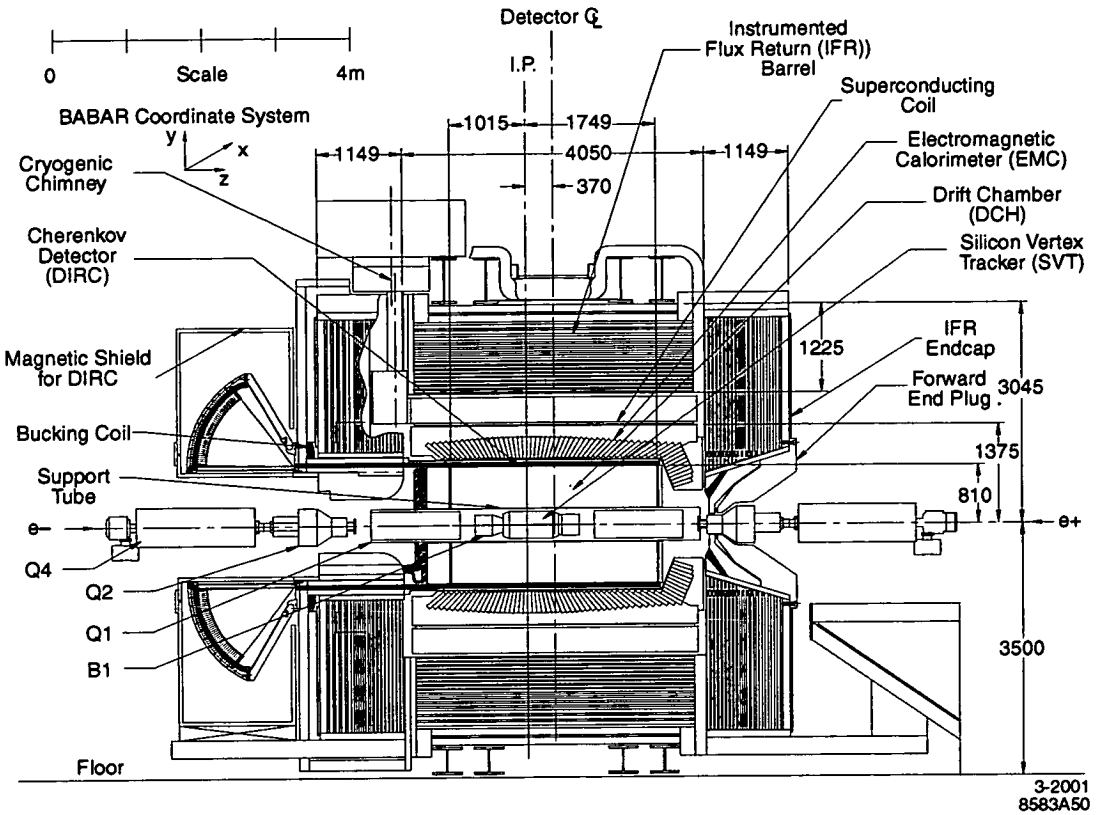

Figure 2-1. *Schematic of the BABAR detector.*

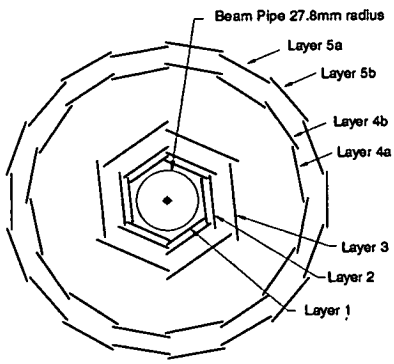

Figure 2-2. *End view of the SVT.*

2.3.1.2 SVT Radiation Protection

The SVT receives a high radiation dose by virtue of being the detector component closest to the IP. Unfortunately the SVT is also highly inaccessible so reliability is very important. Initially it was hoped that the SVT would survive the whole ten year life of the *BABAR*

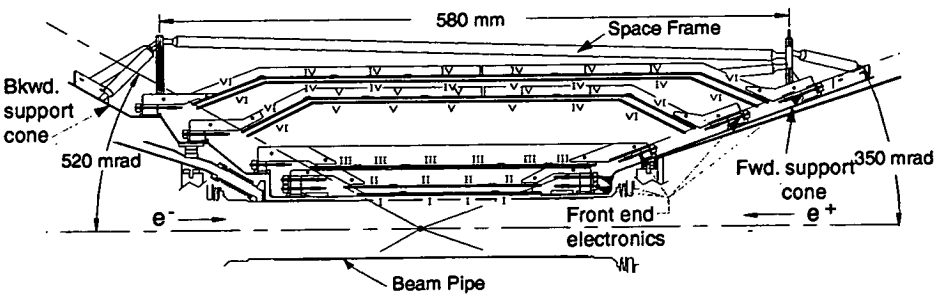

Figure 2-3. *Side view of the SVT.*

experiment, but it has become obvious that this is unrealistic. The radiation near the IP is non-uniform in azimuth, peaking in the bending plane of the machine. This is causing an accelerated degradation in performance of the mid-plane sections of the SVT. In 2004 the SVT will need to be removed so that the mid-plane sections can be replaced.

In an effort to improve the longevity of the SVT, *BABAR* imposes a radiation budget on PEP-II, requiring that time be spent tuning the collider to reduce background radiation. To administer the dose budget the SVT has a series of twelve PIN diodes mounted around it, monitoring the radiation dose. A voltage is applied across each diode and the resulting leakage current is proportional to the dose received by the diode. The diodes are arranged in two rings, one at the front and one at the rear of the SVT, with six diodes equally spaced in each. The arrangement is such that four diodes lie in the mid-plane of the detector where the radiation is at its highest. In addition to providing information about the instantaneous and integrated doses received by the SVT some of these diodes are read out by an abort module, which interlocks the PEP-II abort system and the SVT power. Most aborts occur during beam injection, although aborts also occur when the beams become unstable.

2.3.2 The Drift Chamber

The DCH is *BABAR*'s principal tracking device and provides high reconstruction efficiency for tracks with transverse momentum greater than 100 MeV/c. For decay and interaction vertices outside the SVT volume the DCH is the sole source of reconstruction information. Hence, it must be possible to make a measurement of longitudinal position with a precision $\approx$ 1 mm.

2.3.2.1 Construction

The Drift Chamber is formed from forty layers of wires arranged into ten super-layers. The chamber is composed of hexagonal cells, with a 20 μm gold-plated tungsten-rhenium sense

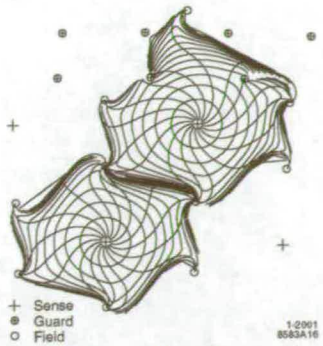

Figure 2-4. *The isochrones of two DCH cells in layers 3 and 4 of an axial super-layer. The isochrones are 100* ns *apart, and circular near the sense wires. Close to the field wires they become irregular and extend into the gap between super-layers.*

wire in the centre surrounded by 120 μm or 80 μm gold-plated aluminium field wires (figure 2-4). The chamber is filled with Helium and Isobutane in a 4:1 mix that provides good spatial and dE/dx resolution while limiting the amount of material inside the DCH. The chamber is 2.8 m long, formed from a beryllium cylinder of radius 23.6 cm and a two layer carbon fibre cylinder of radius 80.9 cm, with aluminium end-plates (figure 2-5).

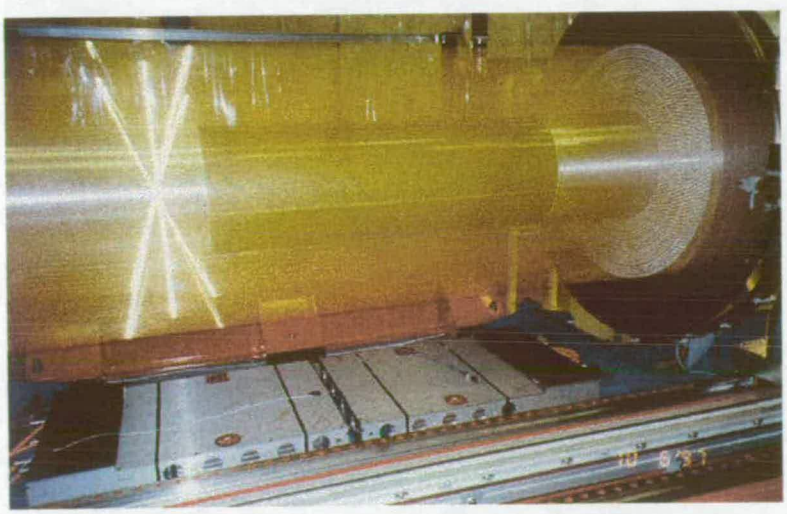

Figure 2-5. *Photograph of the DCH during construction.*

2.3.2.2 Performance

For the study of radiative penguin decays, which all contain charged tracks, a quality tracking system is vital. During the first year of operation the tracking capabilities of the DCH and SVT were closely studied and a summary of those studies is presented here.

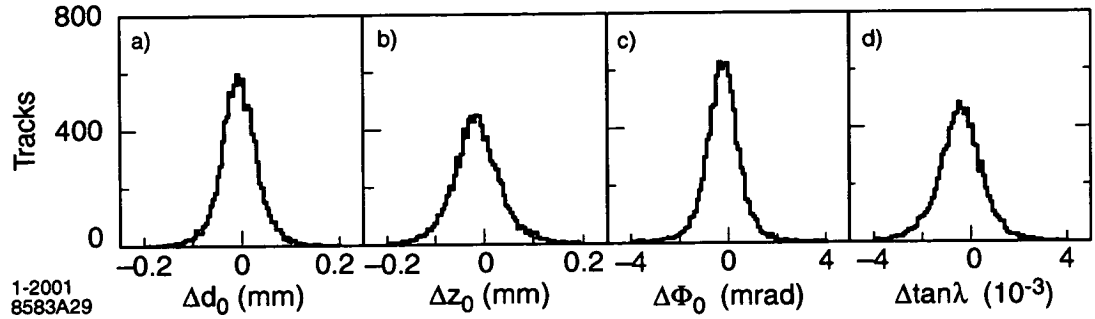

Figure 2-6. *Track parameter resolutions as found from the comparison of the two halves of cosmic ray muon tracks with transverse momentum above 3* GeV/c.

Figure 2-6 summaries various track parameter resolutions:

1. d_0, radial distance of closest approach to the IP.
2. z_0, longitudinal distance of closest approach to the IP.
3. Φ_0, azimuth of the track.
4. λ, dip angle relative to the transverse plane.

These are measured offline using e^+e^- and $\mu^+\mu^-$ pair events, multi-hadron events, and cosmic ray muons recorded during normal data-taking.

The upper and lower halves of the cosmic ray track passing through the DCH and SVT are fit as two separate tracks and the resolution is then derived from the difference in the measured parameters for the two track halves. Based on the full-width at half-maximum of the distributions shown in figure 2-6 the resolutions for single tracks are parameterised as

$$\sigma_{d_0} = 23\,\mu\text{m} \quad \sigma_{z_0} = 29\,\mu\text{m} \quad \sigma_{\Phi_0} = 0.43\text{mrad} \quad \sigma_{\tan\lambda} = -0.53 \times 10^{-3} \tag{2.1}$$

The d_0 and z_0 resolutions depend on p_t, and these dependencies are shown in figure 2-7.

$K - \pi$ separation is very important for radiative penguin studies. The DRC provides *BABAR* with an innovative dedicated particle identification system (see section 2.3.3), but for low momentum particles, and those which fly outside the detection region of the DRC, the DCH must supply all the necessary information. $K - \pi$ separation is accomplished using a measurement of the energy loss, dE/dx (figure 2-8). The DCH was designed to allow $K - \pi$ separation of tracks up to 700 MeV/c, and this goal has been achieved with a dE/dx resolution of 7.5%.

Position and angle measurements for those charged tracks that pass through the SVT are dominated by the SVT measurements while the DCH contributes primarily to the p_t measurement. The p_t resolution is also determined from cosmic rays, and is shown in figure 2-9. For

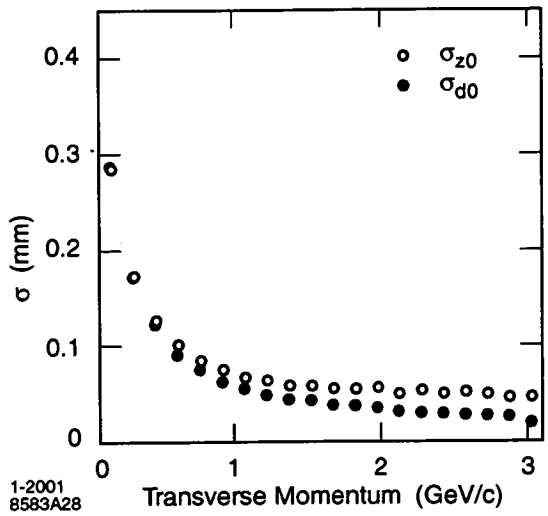

Figure 2-7. *d_0 and z_0 resolution for tracks in multi-hadron events as a function of p_t.*

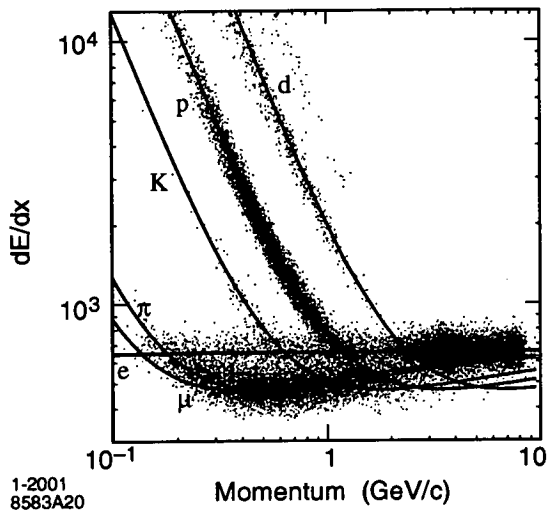

Figure 2-8. *dE/dx in the DCH as a function of track momentum. The curves show the Bethe-Bloch predictions derived from selected control samples of particles of different masses.*

low momentum tracks the momentum resolution is limited by multiple scattering in the SVT, the support tube, and the inner cylinder of the DCH. The p_t dependence of the resolution is essentially linear and the data are well represented by the function,

$$\sigma_{p_t}/p_t = (0.13 \pm 0.01)\,\% \times p_t/\,\mathrm{GeV} + (0.45 \pm 0.03)\,\% \qquad (2.2)$$

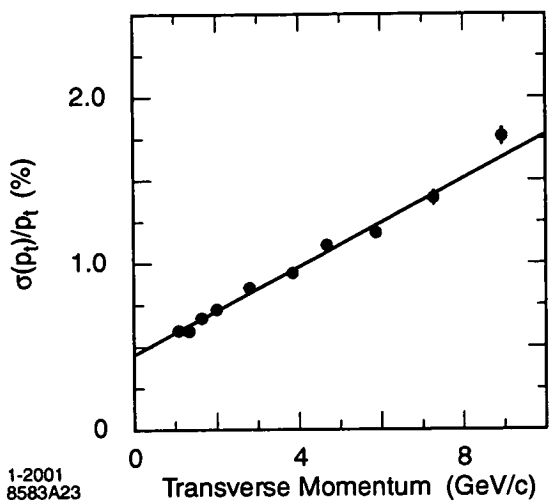

Figure 2-9. *Resolution in p_t determined from cosmic ray muons passing through the DCH and SVT.*

2.3.3 The Detector of Internally Reflected Čerenkov Light

The Detector of Internally Reflected Čerenkov Light is a novel type of Čerenkov detector devoted to particle identification. The DRC plays a crucial rôle in distinguishing kaons from pions. Since the study of radiative penguins often involves one or both of these, the DRC is very important to the analyses presented in this thesis.

2.3.3.1 Construction

Figure 2-10 shows a side view schematic of the DRC. The radiating medium is quartz, in the form of one hundred and forty-four long, straight bars (figure 2-11), arranged in a dodecagon barrel. The bars are 1.7 cm thick, 3.5 cm wide and 4.9 m long, extending through the steel of the backward barrel flux return. Čerenkov photons are internally reflected inside the quartz bars and thus brought outside the magnet and flux return. Only the backward end of the DRC is instrumented. The forward ends of the bars are mirrored, so that photons are reflected back toward the instrumented end, preserving the Čerenkov angle. A trapezoidal piece of quartz glued to the backward ends of the bars folds one half of the image onto the other to reduce the area which must be instrumented. Quartz wedges interface with the *standoff-box*, which is filled with six thousand litres of purified water, where the image is expanded before being detected by an array of eleven thousand photo-multiplier tubes (PMTs). Water was selected since it is cheap and has a refractive index ($n \approx 1.346$) which is reasonably close to that of the quartz bars ($n \approx 1.473$), minimising internal reflection at the boundary. Furthermore, the chromaticity indices of water and quartz are close, effectively eliminating dispersion at the

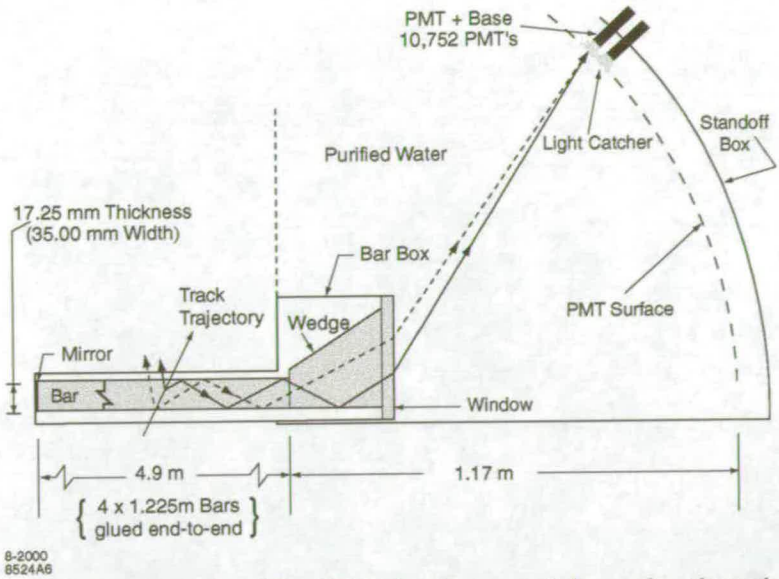

Figure 2-10. *Side schematic of the DRC showing a particle passing through one of the quartz bars and the resulting Čerenkov radiation being internally reflected along the bar and then expanding in the stand-off box before being detected in the photo-multiplier tubes.*

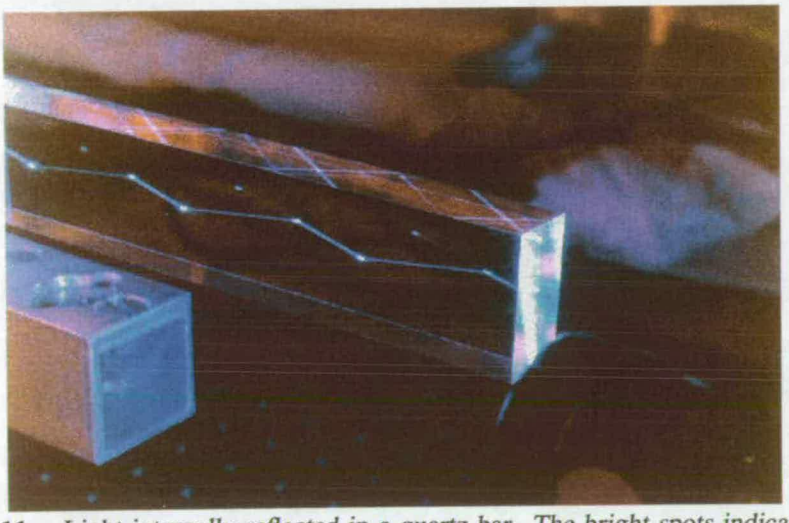

Figure 2-11. *Light internally reflected in a quartz bar. The bright spots indicate that the internal reflection is not total.*

water-quartz interface and ensuring that the refraction angle is almost constant with respect to photon energy.

2.3.3.2 Performance

The Čerenkov angle, θ_C, is given by

$$\cos\theta_C = \frac{1}{n\beta} \tag{2.3}$$

where $n = 1.473$ is the refractive index of the radiating medium, the quartz bars of the DRC, and $\beta = v/c$ is the particle velocity. In the absence of correlated systematic errors the resolution of the Čerenkov angle should scale as

$$\sigma_{C,track} = \frac{\sigma_{C,\gamma}}{\sqrt{N_{pe}}} \tag{2.4}$$

where $\sigma_{C,\gamma}$ is the single photon Čerenkov angle resolution and N_{pe} is the number of photons detected. $N_{pe} \approx 28$ for a $\beta = 1$ particle entering normal to the centre of a bar. Figure 2-12 shows that N_{pe} increases by over a factor of two in the forward and backward directions.

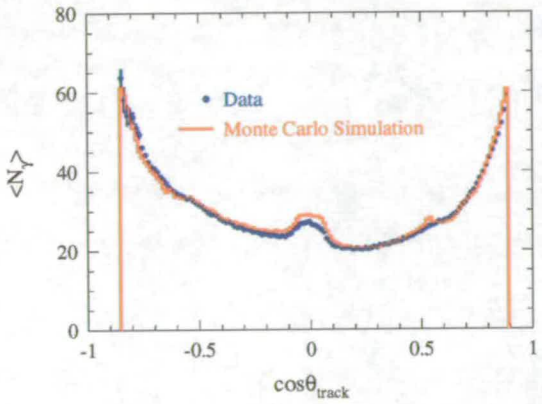

Figure 2-12. *Number of detected photons in di-muon events vs track polar angle.*

The single photon angular and time resolutions are found, from the data shown in figure 2-13, to be

$$\sigma_{C,\gamma} = 10.2\,\text{mrad} \quad \sigma_{t_\gamma} = 1.7\,\text{ns} \tag{2.5}$$

The angular resolution is in good agreement with expectations, and the time resolution is close to the intrinsic transit time spread of the PMTs, 1.5 ns.

Figure 2-14 shows the $K - \pi$ separation as a function of momentum. When the DRC was designed it was hoped that the $K - \pi$ separation would be $4\,\sigma$ for all tracks from the pion Čerenkov threshold up to 4.2 GeV/c. However, the $K - \pi$ separation falls below $4\,\sigma$ at about 3 GeV/c, dropping to $2.5\,\sigma$ at 4.2 GeV/c.

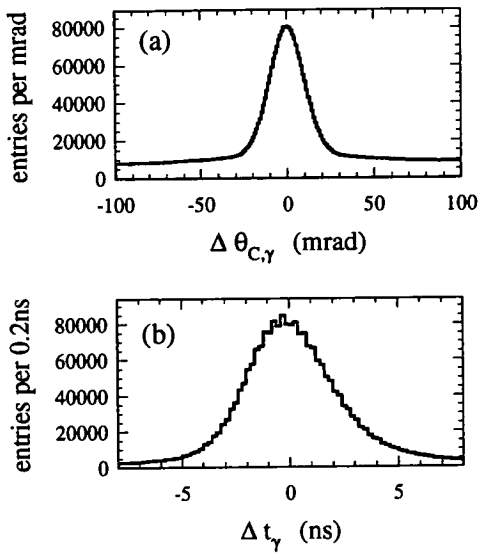

Figure 2-13. *The difference between (a) the measured and expected Čerenkov angle for single photons, and (b) the measured and expected photon arrival time, for single muons in $\mu^+\mu^-$ events.*

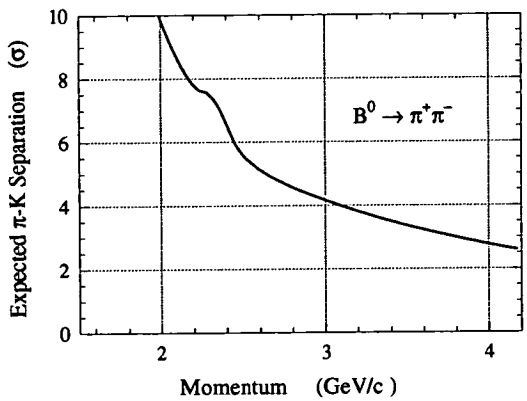

Figure 2-14. *Expected $K - \pi$ separation in $B^0 \rightarrow \pi^+\pi^-$ events vs track momentum inferred from the measured Čerenkov angle resolution and number of photons per track in di-muon events.*

2.3.4 The Electromagnetic Calorimeter

The Electromagnetic Calorimeter detects electromagnetic showers over the energy range 20 MeV to 9 GeV. This coverage permits the detection of low energy neutral pions and eta mesons as well as the high energy photons from radiative one-loop events. Clearly the calorimeter is of fundamental importance to the study of radiative one-loop decays where event selection typically starts with a high energy photon and π^0s are involved in many decays.

2.3.4.1 Construction

Formed from six thousand five hundred and eighty trapezoidal Thallium doped Caesium-Iodide (CsI(Tl)) crystals, the EMC is built in two sections, a barrel (five thousand seven hundred and sixty crystals) and a forward endcap (eight hundred and twenty crystals) as shown in figure 2-16. A side view schematic of a single crystal is shown in figure 2-15. Each crystal is read out by two silicon large-area diodes. This provides both a mechanism for reducing electronic noise, by averaging the response of two healthy diodes; and protection from failing electronics, since the diodes are deep within the detector and replacement is not an option.

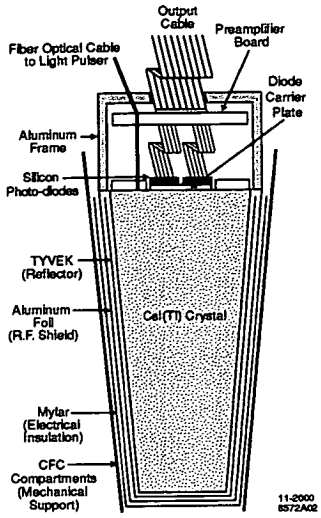

Figure 2-15. *Schematic of an EMC crystal, facing downward.*

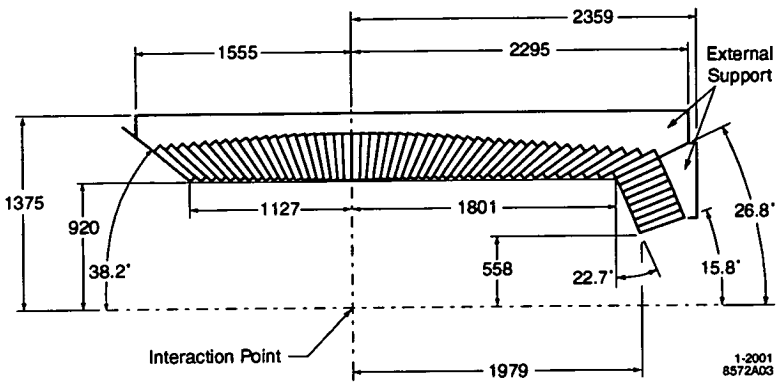

Figure 2-16. *Cross-sectional view of the EMC. There are one hundred and twenty identical strips around the barrel. The number of crystal around a ring of the endcap decreases to one hundred for the middle rings and eighty for the innermost rings.*

2.3.4.2 Calibration Systems

The EMC is unique among the detectors in that it is equipped with three separate calibration systems, in addition to any calibrations performed by data analysis. All the subsystems have charge injection mechanisms that allow the response of the readout electronics to a known input to be monitored. However, the EMC also has two external calibration systems intended to monitor crystal degradation.

The radioactive source calibration utilises a series of thin metal pipes that pass across the front of the whole detector. Fluorine atoms within liquid fluorinert are bombarded with neutrons to produce metastable O^{16*} atoms that decay, emitting 6.1 MeV photons, as the fluid is pumped across the face of the detector. The resulting signal is read out through the usual data-taking electronics. After analysis this calibration provides a set of constants, one for each crystal, indicating the required conversion from diode current to absolute energy. This calibration requires a significant period without beams, and is performed when the opportunity arises.

The final calibration system is a light pulser, built in part by Philip Clark as a postgraduate student at the University of Edinburgh [12]. The light pulser consists of a pair of Xenon flash lamps (one for endcap and one for barrel) that illuminate two bundles of optical fibres. The fibres then inject light into the back of every crystal in the EMC, and the resulting signals are read out through the normal data-taking electronics, utilising a specialist readout module to provide triggers. Since the Xenon flash lamps have an intensity variation of about 1% between flashes, true changes in crystal performance (typically less than 1%) would be smeared out. The pulse to pulse variation is removed by simultaneously reading out the intensity measured

in a reference crystal, which is maintained at constant temperature and humidity and shielded from radiation. Longer term variations in the system are removed by calibrating the reference crystal with a pair of radioactive sources. The light pulser requires only a few minutes to collect sufficient statistics to measure short term variations in the crystal readout, and to highlight noisy or dead crystals. Once a day a global calibration is performed, where every system is calibrated simultaneously during a short period of no beam. The light pulser is used for the EMC global calibration.

2.3.4.3 Performance

The energy resolution of a homogeneous crystal calorimeter is given by

$$\frac{\sigma_E}{E} = \frac{a}{\sqrt[4]{E}} \oplus b \tag{2.6}$$

where E is the energy of the photon in GeV, σ_E is the rms error and a is an energy dependent term arising from the fluctuations in photon statistics and, to a lesser extent, electronic noise. The constant term, b, which dominates at energies over 1 GeV, arises from non-uniformity in light collection, uncertainties in the calibration and leakage or absorption in the material surrounding the crystals.

The energy resolution is measured using different methods in different energy regions. At lowest energy the radioactive source is used to measure the resolution directly giving $\sigma_E/E = 5.0 \pm 0.8\%$ at 6.31 MeV. At the highest energy Bhabha scattering gives a resolution of $\sigma_E/E = 1.9 \pm 0.07\%$ at 7.5 GeV. At about 500 MeV the decay $\chi_{c1} \to J/\psi\gamma$ is used, while at energies below 2 GeV the decays $\pi^0 \to \gamma\gamma$ and $\eta \to \gamma\gamma$ are used. The data are combined to produce the plot in figure 2-17.

Fitting to the energy dependency yields the relation

$$\frac{\sigma_E}{E} = \frac{(2.32 \pm 0.30)\,\%}{\sqrt[4]{E}} \oplus (1.85 \pm 0.12)\,\% \tag{2.7}$$

where E is in units of GeV.

Figure 2-18 shows the neutral pion mass peak. The reconstructed neutral pion mass is 135.1 MeV/c^2 and is stable to better than 1% over the full photon range. The width is found to be 6.9 MeV/c^2.

2.3.5 The Super-conducting Magnet

To obtain a momentum measurement of charged tracks from the tracking detectors, the inner detectors are subjected to a 1.5 T magnetic field provided by a super-conducting solenoid. The field strength was selected to provide the desired momentum resolution for charged

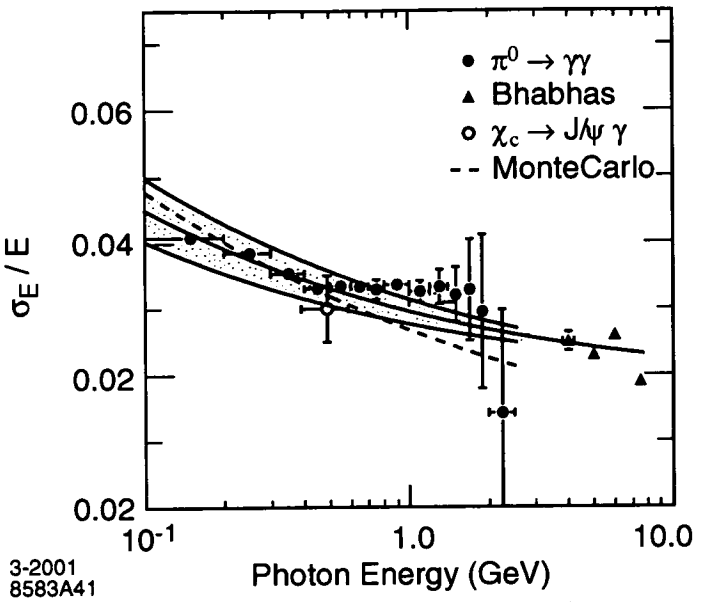

Figure 2-17. *Energy resolution for the EMC measured for various processes. The solid curve is a fit to equation 2.6, with the rms error of the fit denoted by the shaded area.*

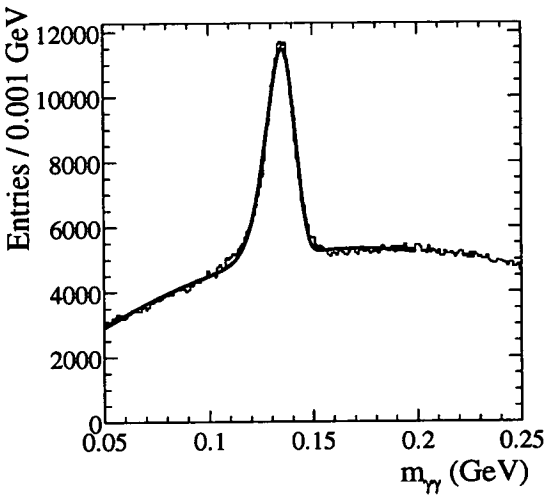

Figure 2-18. *Invariant mass of two photons in the $B\overline{B}$ system. The solid line is a fit to data. The photons are required to have an energy greater than 30* MeV.

particles, and the other solenoid parameters are determined by geometry considerations. The inner radius of the solenoid, 1.4 m, is set by the size of the inner detectors and the required clearances. The outer radius, 1.73 m, is limited by the need to fit a magnetic flux return around the solenoid in the IR-2 hall where the beam line is only 3.5 m above the floor. Due to complicated geometry at the interaction point, which is necessary to allow the high and low

energy beams to be separated after interacting, the beam axis of PEP-II is not parallel with the magnetic field, although the beams are parallel to one another.

2.3.6 The Instrumented Flux Return

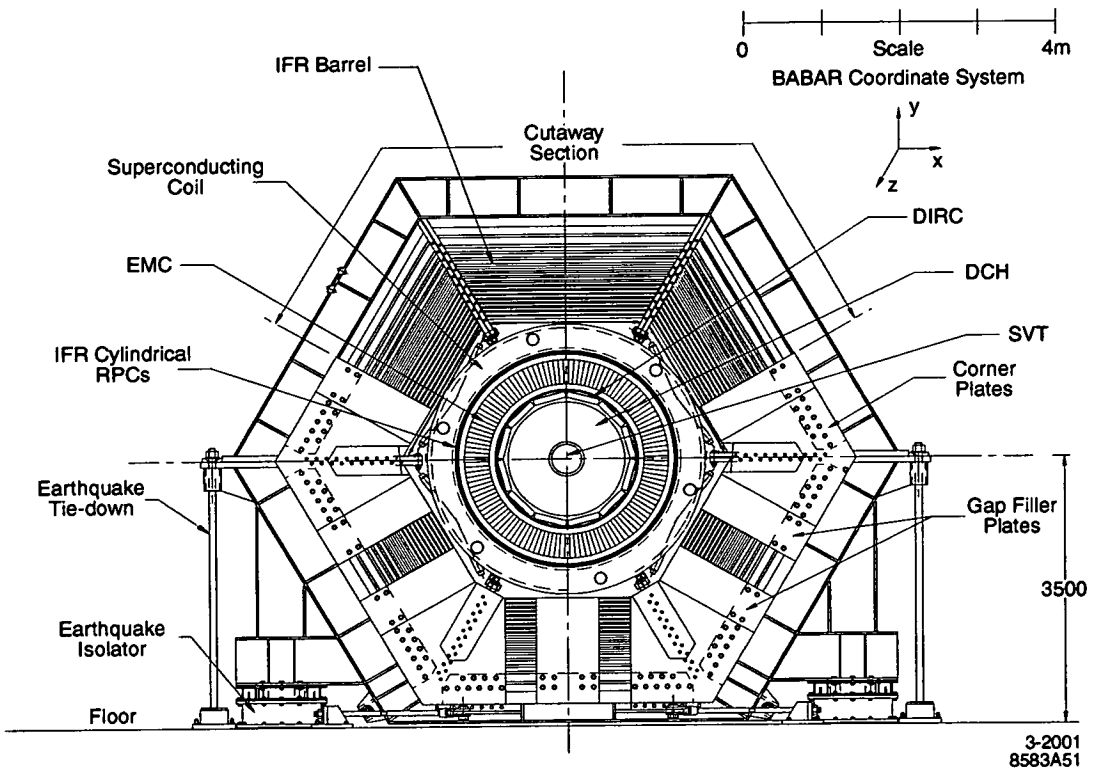

Figure 2-19. *End view of BABAR showing the IFR barrel layers in the cutaway section at the top. The IFR consists of this barrel as well as two endcaps which form the movable* doors *of the detector.*

The flux return assembly provides the external flux path for the magnetic field from the superconducting solenoid, as well as providing the seismic and gravitational load path for the barrel detector. The steel of the Instrumented Flux Return is formed into sheets separated by 30 mm gaps (see the top of figure 2-19). The gaps are then filled by resistive plate chambers which detect streamers from ionising particles using external capacitive readout strips. The IFR is intended to identify muons and detect some neutral hadrons. It is not used in the analyses presented in this thesis.

2.4 Chapter Summary

PEP-II is an asymmetric B Factory designed to produce a great many $B\overline{B}$ pairs to permit the study and accurate measurement of CP violation in the B meson system. Although specifically designed to examine $B\overline{B}$ mixing, the BABAR detector can also be used to search for rare decays, and the large data-set accumulated makes studies of such decays feasible. The Drift Chamber, Electromagnetic Calorimeter and Detector of Internally Reflected Čerenkov Radiation are all critical to the study of radiative penguin decays, but without a robust Data Acquisition system the high luminosities achieved by PEP-II would go to waste.

3

Monitoring Online Dataflow

3.1 Introduction

The high luminosities of the PEP-II *B* Factory present challenges to the detector hardware and Data Acquisition system. This chapter describes these challenges, and the steps taken to confront them, from the perspective of the Online Dataflow portion of the *BABAR* Data Acquisition system. To provide context, the *BABAR* front-end electronics and trigger systems, which are described in detail in [7], are outlined before a full description of Online Dataflow hardware and software is given. The development of an application monitoring Dataflow performance is then described. Output from this application has been used to detect and diagnose problems with the Dataflow system and refine models projecting the future performance. Finally, an example is given of a Dataflow upgrade, allowing the system to deal with increasing luminosity.

3.2 The Data Acquisition System

As shown in figure 3-1, Online Dataflow (ODF) is one link in a chain of systems that convey data from the detector to the *BABAR* database, where it awaits processing before being made available to the collaboration for physics analysis. The inputs to ODF are the detector front-end electronics and the Level 1 trigger while the output of ODF provides input to the Level 3 trigger. Also shown on this simplified block diagram are the Online Detector Controls, which control the operation of the *BABAR* detector.

3.2.1 Front-End Electronics

The Front-End Electronics (FEE) are unique to each detector subsystem, but they must all present the same interface to the Data Acquisition (DAQ) system and so they share a common architecture. Figure 3-2 illustrates the path taken by signals from the detector into the DAQ system. Each FEE chain consists of an amplifier, a digital converter, a trigger latency buffer and an event buffer. The trigger latency buffer is used to store the data during the Level 1 trigger processing. If the event is accepted, the data for that event are transferred from the latency buffer into the event buffer and from there into Online Dataflow. When *BABAR* is taking data, amplification, digitisation, and data readout occur simultaneously and continuously.

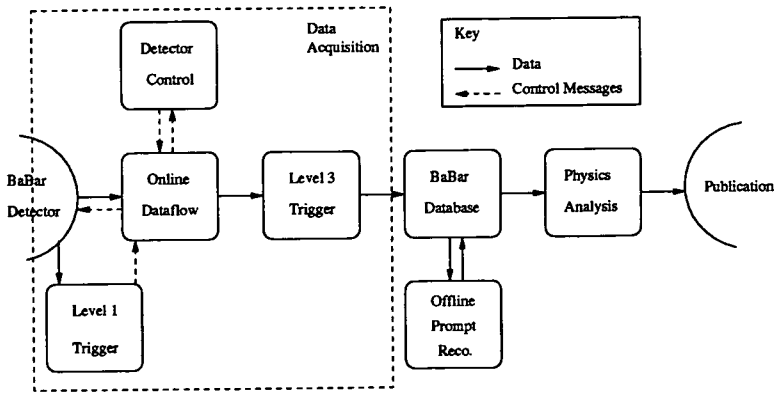

Figure 3-1. *BABAR Dataflow.*

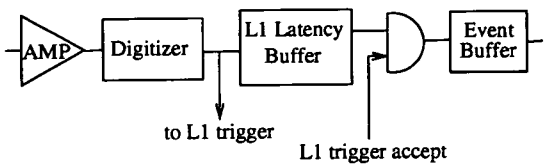

Figure 3-2. *Schematic of the Front-End Electronics. Analogue signals from the detector enter at the left and digital data pass out to Online Dataflow at the right.*

For most of the subsystems the FEE chain is entirely on the detector. However, data from the EMC are continuously transferred away from the detector with both the trigger latency buffer and the event buffer located inside ODF hardware.

3.2.2 Level 1 Trigger

The trigger is responsible for the selection of events of interest from amongst the various backgrounds. The Level 1 (L1) trigger primarily identifies physics event topologies, and thus reduces beam-induced backgrounds to a level acceptable to ODF and the Level 3 trigger. To illustrate the challenge, table 3-1 shows cross-section, production rate, and L1 trigger rate for the principal physics processes at *BABAR*. The values shown are for on-peak running at 10.58 GeV and a luminosity of $3 \times 10^{33}\,\mathrm{cm}^{-2}\mathrm{s}^{-1}$. The e^+e^- cross-section refers to events with either the e^-, or the e^+, or both, inside the EMC detection volume. The total L1 trigger rate from these processes is only 170 Hz, while the typical L1 trigger rate is 1 kHz. The remaining triggers come from cosmic rays and beam effects; the former providing a reasonably constant number of triggers, the latter being proportional to the beam currents.

The L1 trigger is implemented using dedicated processors. Figure 3-3 illustrates the path taken by data through the L1 trigger. Input to the Electromagnetic Trigger (EMT), Drift Chamber Trigger (DCT) and Instrumented Flux-Return Trigger (IFT) comes from the cor-

Event Type	Cross Section(nb)	Production Rate(Hz)	L1 Trigger Rate(Hz)
b $\bar{b}$	1.1	3.2	3.2
other q $\bar{q}$	3.4	10.2	10.2
e^+e^-	$\approx$53	159	156
$\mu^+\mu^-$	1.2	3.5	3.1
$\tau^+\tau^-$	0.9	2.8	2.4

Table 3-1. *Trigger rates for the dominant production processes at BABAR.*

responding detector subsystem. These three subsections of the L1 trigger produce trigger primitives; tracks in the DCH and IFR, and electromagnetic showers in the EMC. The primitives are combined within the the Global Trigger (GLT) before being sent to the Fast Control and Timing System (FCTS). The FCTS can optionally mask or prescale any trigger; for example, a fraction of Bhabha events are selected for calibration and diagnostics. The trigger definition logic, masks, and prescale factors can be configured on a run-by-run basis. Whenever a valid trigger remains the FCTS generates a L1 Accept message which is then distributed to the detector FEE, initiating the transfer of data from the trigger latency buffer into the event buffer.

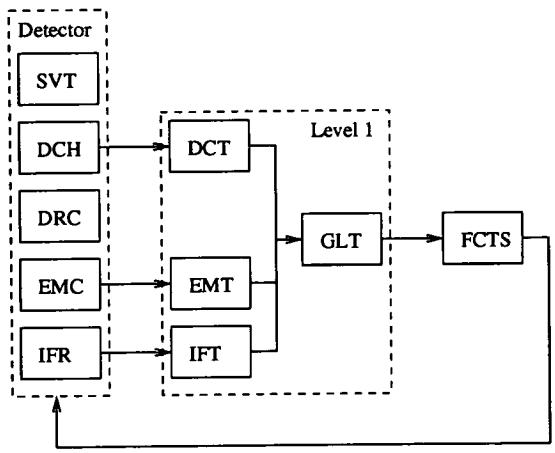

Figure 3-3. *Path taken by the data through the Level 1 trigger.*

The L1 trigger processing must be completed before the FEE trigger latency buffer is overwritten. The latency buffer capacity is 12.8 μs. The DCH and EMC send data to the DCT and EMT about 2 μs after an e^+e^- collision. The DCT and EMT processing times are 4-5 μs, and it then takes a further $\approx$ 3 μs to issue a L1 accept. The L1 accept takes $\approx$ 1 μs to propagate through the system. The total time taken is thus $\approx$ 11 μs.

3.2.3 Level 3 Trigger

The Level 3 (L3) trigger reconstructs, classifies, and filters the events using a system of algorithms that refine and augment the selection processes used in L1. Unlike L1, L3 is implemented entirely in software running on commercially available workstations. ODF and L3 are closely integrated, linked together into a single application, running on the same processor and communicating using shared memory. ODF presents L3 with complete events that are then subjected to the L3 trigger algorithms.

3.3 Introduction to Dataflow

Online Dataflow is responsible for transporting data from the FEEs to the L3 workstations and building the segments of data into complete events. This process is initiated by the L1 trigger and is regulated by *back-pressure* where each section of the process asserts a `busy` signal when it can no longer accept any more data. The individual links in the Dataflow chain are connected by first-in-first-out (FIFO) buffers to absorb event-by-event variations in processing time. The data are pushed into the FIFO by the previous link in the chain provided that the `busy` signal has not been asserted.

As shown in figure 3-4, ODF is logically split into five *levels*, each of which performs a distinct task

Control Generates commands that move the Dataflow system through the states of a finite state machine.

Source The master crate of ODF that distributes commands and Level 1 trigger signals to the other crates of the Dataflow system. The master crate contains the Fast Control and Timing System for *BABAR* and has the capacity to maintain multiple subsets of crates (partitions) allowing the Dataflow system to be *partitioned* for calibrations and development.

Segment A single (slave) readout module (ROM) in a slave crate into which the fibres from the FEE connect and on which sub-system specific signal extraction software is run.

Fragment The master ROM that collects the output of the slave ROMs across the VME[1] backplane and then transmits the data across a network.

Event The L3 farm node which collects the twenty-three fragments and builds them into a single event[2].

[1] Versa Module Europa; a bus specification

[2] In the caption to figure 3-4 the farm is described as 32 Sun workstations. This has since been changed to any number of x86 processors running Linux. The system is described as it was when the author of this thesis was working for ODF.

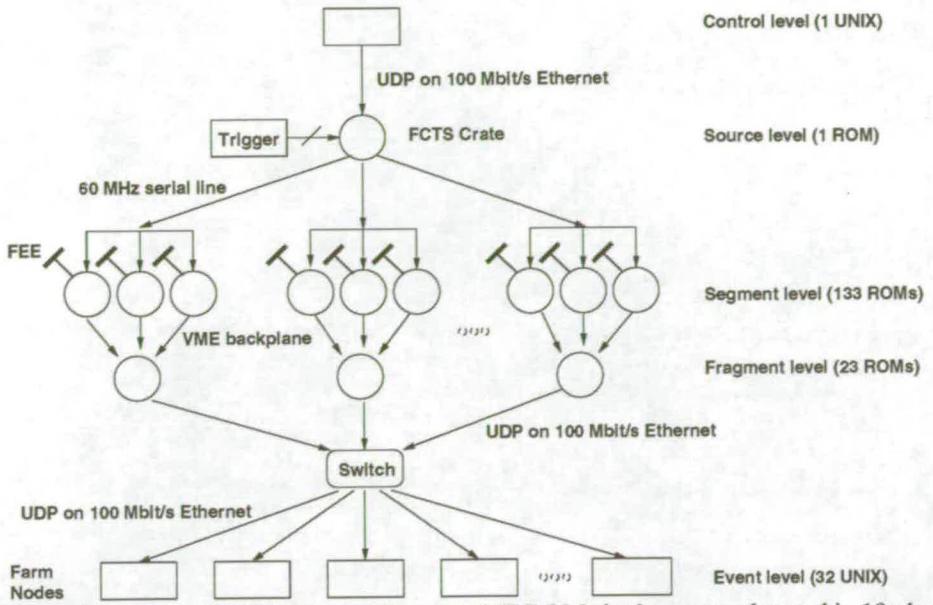

Figure 3-4. *BABAR ODF platform. There are 157 ROMs in the system located in 19 physical VME crates divided into 24 logical crates by virtue of split back-planes. The UNIX farm consists of 32 Sun workstations. The network is a switched 100* Mbits/s *Ethernet. The switch is a CISCO Catalyst 6500.*

3.3.1 Readout Modules

The readout modules are formed from three components as shown in figure 3-5. A Controller Card interfaces with the backplane of the VME crate that houses the module. The fibre optic cable from the FEE terminates on a specially designed Personality Card and data processing is performed on a single-board computer.

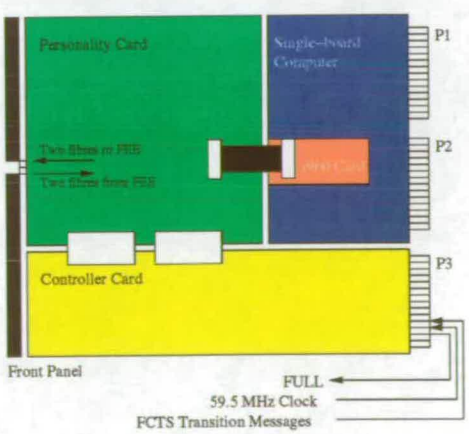

Figure 3-5. *Schematic of a BABAR readout module showing the three components.*

There are two flavours of personality card, triggered and untriggered. The Untriggered Personality Card provides a continuous readout of the FEE into a trigger latency buffer on the card itself (see section 3.2.2). Only the EMC makes use of Untriggered Personality Cards to provide input to the EMT. A Triggered Personality Card pulls data from the buffer across the fibre connections only when an L1 accept is received. The L1 accept causes both types of personality card to transfer the data across a PCI[3] bridge into memory on the single-board computer. When the data arrive in the memory of the single-board computer they are subjected to various subsystem specific algorithms to extract the relevant information.

3.3.2 Event Building

Each ROM receives data from a small section of the detector. These segments of data are passed across the VME backplane to the master ROM and collected into a fragment. Fragments from several events are then batched together by the master ROM and transmitted across a private subnet, using the User Datagram Protocol (UDP)[4], to one of the L3 workstations. All the master ROMs use the unique time-stamp of each fragment batch to determine which workstation will receive the data. This ensures that all the fragments from one event end up on the same machine while the loading of the farm nodes is evenly distributed. Once the farm node has received fragments from all the master ROMs the fragments are built into events. This final stage of ODF is performed on the L3 farm node within the same application as the L3 algorithms are run. The event is built in shared memory to reduce the number of copy operations required.

3.3.3 UNIX Timers

Some actions performed by the Dataflow system are required to occur regularly with a predetermined frequency, so the *BABAR* Dataflow software provides a class[5] called `odfTimer` that fires with a configurable frequency, and initiates the requested action. The original timing mechanism used on the UNIX portion of the Dataflow system, the L3 farm nodes, was flawed. This was discovered during the testing phase of the VMON development and had to be rectified before VMON could be deployed. Before discussing the faults with the old timer, and the eventual solution, it is necessary to describe some fundamentals of the UNIX environment

[3]Peripheral Component Interconnect

[4]The User Datagram Protocol (UDP) and Transport Control Protocol (TCP) are the most commonly used protocols for transporting data over networks. For detailed descriptions see [13].

[5]Like almost all *BABAR* software, ODF software is written in C++.

3.3.3.1 Processes and Threads

Most modern operating systems allow multiple applications to be run on a single CPU, apparently simultaneously. Each time a new application is started the operating system creates a new *process*[6] and allocates it a share of the system resources. The operating system protects processes from each other to prevent data corruption and resource theft. Part of the operating system, called the *scheduler*, apportions CPU time to each of the processes. The act of creating a process, allocating resources and establishing the necessary protections is computationally expensive. Furthermore, the operating system protection makes it very hard for processes to pass information amongst themselves; to pass a message between processes requires the use of the operating system itself as an intermediary, which is computationally expensive.

The difficulties associated with using processes have prompted some operating system designers to develop a more streamlined alternative called *threads* (in Linux) or *lightweight-processes* (in Solaris). Like processes, threads provide a way to interleave several different sets of operations allowing them to execute simultaneously on a multi-processor system, and giving the impression that they are executing simultaneously on a uni-processor system. However, unlike processes, threads do not receive dedicated resources. Multiple threads within a single process share resources. Inter-thread communication is much simpler than inter-process communication; it is as simple as changing a common variable. Of course, this convenience comes with the risk of data corruption.

For improved portability of Dataflow software, *BABAR* ODF wraps the platform dependant threads in a class called `odfTask`. In fact the Dataflow tasks are a little more complex than simple threads. Work to be done by a task is packaged up in a class and an instance of that class is appended to a queue associated with the task selected to perform the work. After the work has been completed the task moves on to the next item in the queue.

3.3.3.2 Thread Safety

Clearly there is great capacity for interference between threads since any variable that is visible to multiple threads may be changed at unpredictable times. In a single CPU computer only one thread can be executing at a time. The scheduler is responsible for selecting which thread will execute based on the relative importance of the threads that are ready to do work and the length of time they have been waiting. Problems typically arise when the thread that is currently executing is *pre-empted* by a thread of greater importance.

When a thread is pre-empted it stops executing instructions and the contents of all the registers on the CPU, collectively called the *context*, are stored in memory. The previously saved context of the higher priority thread is then restored by being copied into the CPU registers before the CPU starts executing instructions for this new thread. After some period of time the

[6] Some operating systems call processes *tasks*.

pre-empted thread will be permitted to continue executing and its context will be restored to the CPU registers. Unfortunately any variables visible to both threads may have been altered. Within the context of the pre-empted thread it appears as if the variable has spontaneously changed between the execution of one instruction and the next. Any section of code that depends on a variable remaining the same over several instructions is vulnerable, for example any `if` conditional that checks a variable visible to multiple threads is at risk, since the variable may change between the check and any subsequent action.

It is possible to construct methods that will function flawlessly even if the executing thread is pre-empted, such methods are *thread-safe*. The non-trivial case is one where a function invokes inter-thread communication through the deliberate manipulation of shared data. A range of techniques are available to ensure thread-safety, each with strengths and weaknesses that usually reduce to balancing speed and safety. It is possible to use methods that are not thread-safe in a multi-threaded environment, but all such methods must be confined to a single thread, ensuring that they run sequentially and cannot pre-empt one another.

3.3.3.3 Signals

Creation of a new thread is an example of a *synchronous event*. The parent and child are synchronised because the execution point of both threads at the moment of creation is known in advance. Other examples of synchronous events usually involve calling a function that then waits for some external condition to be satisfied before returning. A thread that is waiting for external stimuli is said to be *blocked*.

Events in the real world are *asynchronous*. There is no way of determining in advance what instruction a thread will be executing when an event occurs, or even which thread will be running on the CPU. A common method for handling asynchronous events in the UNIX environment is through the use of *signals*. Signals are very simple messages, often just a single identifying integer, that are generated by the operating system in response to an event. A set of complex rules [14] governs which process will receive a given signal, but the precise outcome tends to be implementation dependant and sometimes unpredictable.

3.3.3.4 Dataflow Timer Design

The original Dataflow UNIX timer was written for Solaris and was built around the `sleep` system call, which simply blocks the calling process for a specified time. The function call returns when the operating system generates a signal, but this design has two problems.

Firstly, another signal from some other thread can terminate the `sleep` prematurely. The function's return code will indicate that this has occurred, but there is no way of determining how much time remains until the `sleep` would have terminated normally. Thus a timer based on the `sleep` system call can only guarantee that the action will be started between the time that `sleep` is called and the time that `sleep` was requested to terminate, but cannot

guarantee a minimum delay. Secondly, the signal generated when `sleep` terminates can be caught by some other thread, with unpredictable results.

The solution to both these problems was to develop a new timer based on a different system call, `pthread_cond_timed_wait`[7]. This system call also blocks the calling thread for a specified time, but when it terminates it does not generate a signal and if it terminates prematurely it records the amount of time remaining until its requested termination. It is simple to wrap the system call `wait` inside a loop and restart it until the specified time has passed.

To permit the `odfTimer` to call methods that are not thread-safe it must be possible for a programmer to specify the thread that the action will be executed in, the action thread, as well as the period of the timer and the action itself. At least one other thread must exist, since calling `wait` from the action thread would cause it to block, preventing it from performing any other work, so the constructor the `odfTimer` creates a private thread. A private class contains the call to `wait` and the timer is started by queueing an instance of this class to the private thread. Once the required period of time has passed the private class, running in the private thread, appends an instance of the action class to the queue of the action thread. Once the action thread has completed the action, the timer is restarted and the process continues.

Once the timer is started it can be difficult to stop cleanly. A naive approach to destroying the timer might propose sending a signal the timer to interrupt the call `wait` to return and then calling the `odfTimer` destructor to terminate the private thread and release any resources. However, following this prescription would result in an application that would function correctly for a short period of time before crashing, because this design contains several *race conditions*.

Race conditions occur whenever the order of thread execution becomes important; one thread is racing another to complete its task. Often they involve the destruction of an object by one thread that is being used by another. If the thread that is using the object finishes before the other thread runs then the application will function correctly, but if the thread using the object is pre-empted, and the object is destroyed, any subsequent attempt to use the object will crash the application. Race conditions are particularly troublesome because the errors they cause are very hard to reproduce since they depend on the loading of the CPU, the timing of asynchronous events and even the position of data files on the workstation harddrive.

The proposed destruction sequence above assumes that the `odfTimer` is currently blocked in the `wait`, which is not always true. The timer may have returned from the wait and already queued the action to the action thread. Following the above prescription will destroy the timer, but when the action completes and the action thread tries to restart the timer it will access an invalid pointer and crash the application.

The destruction of the `odfTimer` is actually quite convoluted. First a flag indicating that the timer should not be restarted must be set. Since this flag is visible to multiple threads a *lock* must be obtained before it is altered or checked, preventing any other thread reading or writing

[7]Henceforth called `wait`.

the flag. This guarantees thread-safety. Setting the flag ensures that if the action is already queued to the action thread no attempt will be made to restart the timer. Next a special class indicating that the timer must be destroyed is queued to the action thread. This synchronises the threads by ensuring that any further steps towards the destruction of the timer only take place after the action thread queue has been drained of anything that would try to access the timer. Finally, the `odfTimer` destructor is queued back to the private thread and the timer is destroyed. This final step is necessary because it is possible that the timer restart had been queued to the private thread, but not yet initiated, when the `odfTimer` destruction sequence was begun..

The final `odfTimer` avoids the pitfalls of the original timer and provided a time granularity of approximately 10 ms on a SUN SPARC 5. Although only a few tens of lines of code long the timer required several man months of effort, mostly resolving race conditions.

3.4 Vertical Monitoring of the Dataflow System

3.4.1 Introduction

Maintenance and modelling of the Dataflow system requires effective monitoring of the ODF platform at the level of individual CPUs (ROMS and farm nodes) whilst BABAR is collecting data. To achieve this goal a monitoring tool, called Vertical Monitoring (VMON), was designed and implemented over an eighteen month period, before being deployed in March 2001. VMON is formed from two distinct pieces of software, a *client* and a *server*. The client is run on every CPU of the Dataflow system whenever BABAR is collecting data. It accumulates statistics relating to the CPU performance such as the event size and the CPU processing time per event. The clients all transmit their data to a single server running on a workstation that is not being used for data collection. The server coordinates the activity of the clients, whilst providing the user interface and the long-term storage of monitoring data.

3.4.2 System Requirements

The monitoring application was designed to fulfil the following requirements

Generation The generation of VMON data is performed on the CPUs of the ODF platform and thus has the potential to impact data-taking. This is not permissible, so VMON has tight memory and CPU usage constraints.

Transmission The transmission of VMON datagrams will be across the data-taking subnet so has the potential to limit the transport of data across that network. This is not permissible, so VMON has to operate within a budget of two Ethernet packets per CPU.

Reception ODF use of UDP for data transport is motivated by the ability to seamlessly integrate broadcasts, better real-time behaviour (compared to TCP), and the existence of a connectionless protocol[8], but UDP gives responsibility for reliably collecting network data to the receiving application. There is no built-in re-transmission of lost packets and ODF does not not provide this either. UDP is made more reliable by using a clean, isolated, subnet, but sending a large number of packets at the same time will result in lost data. For the VMON application the transmission of packets from different CPUs is staggered to reduce packet collisions.

Display The Display of VMON data should be rapid on a human time scale[9], but cannot affect the recovery of datagrams from the network socket. Anything not read from the socket is lost.

Archive For VMON to be used to troubleshoot ODF, information collected from the ROMs and farm nodes must be stored for later analysis.

Recovery The recovery of the archived data must be trivial, and rapid on a human time scale.

3.4.3 Design

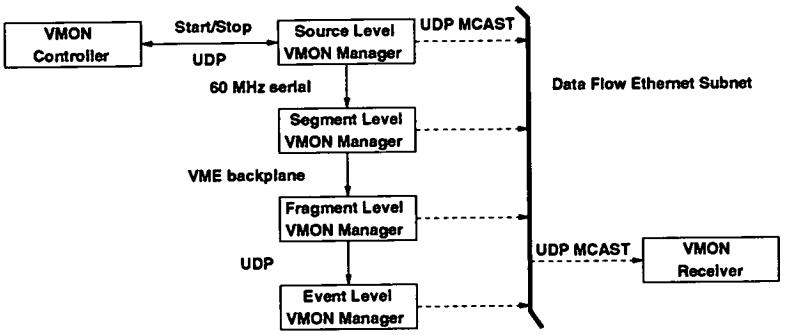

Figure 3-6. *VMON Design. For simplicity only one CPU for each level is shown. Continuous lines indicate the flow of control messages. Dashed lines indicate the flow of VMON data.*

The main components of VMON are a *controller*, a *receiver*, and a *manager*. In network programming terminology the controller and receiver are two threads within the VMON server application, while the manager acts as the VMON client application. The diagram in figure 3-6 gives an overview of VMON's design.

[8]The choice is largely driven by the broadcast requirement, since TCP cannot do this but the connectionless protocol is an added advantage. A connectionless protocol has no long-term relationship between the UDP client and server. UDP avoids the overhead of setting up and tearing down the connection and so requires fewer packets to exchange a request and reply.

[9]For this project Chris O'Grady (SLAC), the project leader, defined the human time scale to be 10 Hz. For the GUI this implies that the time between pressing a button and the screen updating should be no longer than 100 ms.

The controller attaches to the Dataflow partition in order to send messages to the managers. These are shipped through the different levels of the system as normal ODF messages in a path parallel to the L1 message path. The two most frequently used messages are to start and stop monitoring of the partition. By automatically detecting the creation and the destruction of the ODF partition the controller can start and stop the monitoring process as required, allowing VMON to continuously monitor ODF whenever the *BABAR* detector is operating in the standard data collection mode.

The manager runs in each CPU of the Dataflow system. It receives messages from the controller and sends UDP datagrams containing the monitoring information to the receiver. The Receiver, which is based on the `select` system call[10], collects these packets and places them in a circular buffer for other threads in the VMON server to analyse.

The basic piece of VMON data is called an *entry*. Entries can be persistent, i.e. they survive between manager transmissions, or transient, i.e. the memory reserved for them is freed after they have been transmitted. Persistent entries typically contain the actual VMON data while transient entries are used for text messages generated by the manager itself. Persistent entries have a name that, together with an ODF machine identifier, uniquely identifies them. Particular attention has been given to the `fill` method of the various entries. This method

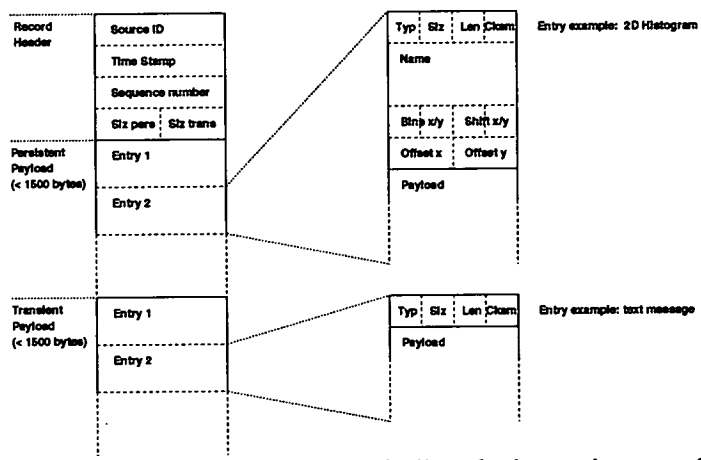

Figure 3-7. *VMON Record Data Format. Typically only the persistent payload is sent out, while the transient one is reserved for exceptional occurrences.*

is critical since it is called for every L1 accept, and so has the potential to impact *BABAR* data collection. The `fill` code has been optimised at the level of the number of instructions. [11]

Different entries can be allocated in a memory buffer called a *record* (Figure 3-7). The record is lock protected at creation time to make the allocation code thread-safe. Each record has a header containing the machine ID, a time stamp, a sequence number, and the size of the

[10]The `select` system call listens for incoming data packets on a network socket. For full details see [13] section 6.3.

[11]The `fill` method for one dimensional histograms takes 6 instructions.

memory allocated for the entries. One record can be as large as two ethernet packets where one packet is used for allocating persistent entries and the other for transient entries.

The frequency with which the manager transmits the packets is regulated by the controller messages. If all the CPUs transmit at the same time, network buffer overflows reduce the number of packets that are successfully delivered. Hence, it is important to ensure that the transmissions are staggered in time. The amount of delay has been determined empirically by measuring the percentage of dropped packets as a function of the staggering time. The effective delay of each manager has been chosen to depend on the machine identity in order to uniformly distribute the transmissions over time.

VMON monitors quantities such as optical fibre data sizes, the processing speed of feature extraction code, the size of the output data, VME DMA[12] rates, other event building performance parameters, the processing speed of the L3 trigger, and errors generated by the system.

3.4.4 Input Data Buffer

The main component of the VMON Receiver is the Input Data Buffer (IDB), shown in figure 3-8. The IDB provides the following features

Buffer Storage space where the receiver saves the incoming records.

Common Entry Point The interface for all VMON objects that request records.

Snapshot The state of the system at a given time.

History The buffer is overwritten by new records, but there is sufficient space to maintain a short history.

The IDB contains a circular buffer where the receiver saves the VMON records. There is no need to lock the IDB for writing since only the receiver ever writes to the buffer. The record is placed directly in the right location when it is received from the network, no extra copy is required. When a record is saved in the circular buffer the IDB updates another circular buffer, called the record table, with a pointer to the saved record. There are as many record tables as machine IDs. When an object requests the records of a specified machine, the IDB interrogates the appropriate record table and returns the pointers to the correct locations. For performance reasons, the IDB does not provide a locking mechanism; the objects which read the IDB are required to check if the record they were analysing was overwritten whilst being read.

[12]Direct Memory Access

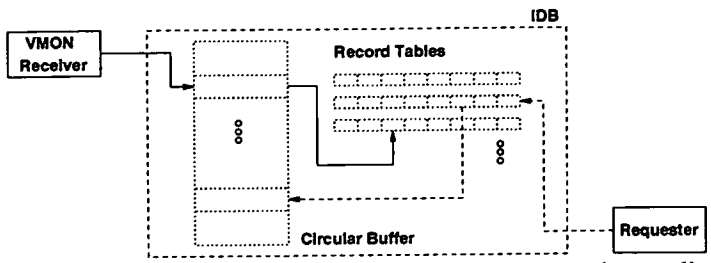

Figure 3-8. *The VMON Receiver writes serially to the IDB (continuous lines). A generic requester can ask for the records that are present in the IDB for a specified machine (dashed lines).*

3.4.5 Archiving

For VMON to be useful for continuous monitoring the data collected must be archived. A combination of compression and selection is used to reduce the large volume of data available to a more reasonable size. By introducing the constraint that all VMON data be integrated over time, within the manager, we can decouple the archive frequency, that is the frequency with which the archiver reads the IDB, from the transmission frequency of the manager. We do not lose information by archiving at a lower rate, the archived data just has a larger granularity.

Most of the data sent from the CPUs is in the form of histograms, most of which are one dimensional histograms with about ten bins. We can reduce the volume of data by an order of magnitude by storing only the mean of the change in the histograms between samples. With two dimensional histograms the mean of the projection onto each axis is stored.

3.4.5.1 Floating point numbers

To limit CPU usage, it was decided during the design phase that the VMON archiver would not employ a sophisticated compression algorithm to reduce disk usage. However, the disk space required can be halved and recovery performance doubled by creating a special form of the floating point number, which occupies only two bytes instead of the standard four. This will reduce the range and precision, but the requirements for VMON are easily satisfied.

The Institute of Electrical and Electronics Engineers (IEEE) published the current standard for binary floating-point arithmetic (IEEE-754-1985). This standard describes the single and double precision floating-point numbers used on modern CPUs. Floating-point numbers are stored in the form

$$n = \pm (1.m) \times 2^e \tag{3.1}$$

where m is the *mantissa* and e is the *exponent*, both expressed in binary. Since every number, except zero, will have a 1 before the decimal point in the mantissa the one is implicit. A single-precision binary floating-point number must fit in 32 bits, while the double precision takes 64 bits. The range of the floating-point representation can be increased by allocating

more of the bits to be exponent, but only at the expense of precision, which is determined by the number of bits used for the mantissa. The IEEE has decided that the right balance is to use 8(11) bits for the exponent and 23(52) bits for the mantissa of single(double)-precision numbers. In both cases the least significant bit indicates the sign of the entire number, and is followed by the exponent with the mantissa taking the most significant bits. To avoid any untidiness dealing with negative numbers, the exponent is stored in *excess notation.* An offset is added to the exponent to ensure that all exponents are positive. For single-precision numbers this offset is 127, while for double-precision numbers it is 1023.

The compressed floating point number was designed to conform as closely as possible to the IEEE 754 standard while using only 16 bits. This would use the first bit for the sign, the following seven bits for the exponent in excess 63 notation and the final eight bits for the mantissa, with the leading one implicit. The range and accuracy of the compressed floating-point number is compared with the single- and double-precision version in table 3.4.5.1.

Bits	Range	Accuracy
16	$6 \times 10^{-20} \rightarrow 2 \times 10^{19}$	4×10^{-3}
32	$6 \times 10^{-39} \rightarrow 2 \times 10^{38}$	1×10^{-7}
64	$1 \times 10^{-308} \rightarrow 9 \times 10^{307}$	2×10^{-16}

Table 3-2. *Comparison of the range and precision for the compressed binary floating-point representation with the single- and double-precision versions.*

The floating-point format also has the capacity to store error values by setting all the bits of the exponent to zero, an invalid value in excess notation for all floats except zero, and storing an error value in the mantissa. The storage of zero as sixteen 0s is compatible with this scheme if zero is not an error value.

It should be noted that this data format is intended for disk storage only and is converted back to double-precision floating point for processing and display. Rather than add full functionality to this type, effort was concentrated on reducing the number of instructions used to convert between the archive floating point number and the double precision - an operation that occurs many times in the archive creation and recovery.

3.4.5.2 Archiver File Format

As important as compressing the archive data and sacrificing detail for disk space is the ordering of data in an archive file. The format of the file is critical both in maximising disk usage and allowing rapid recovery of data. Decisions about the file format influenced the archiver design and placed constraints on the transmitting CPUs. For example, the design of the archive file relies on the assumption that the number and types of persistent entries sent by any one CPU remain constant while the archiver is running. This assumption allows the archive file to be split into two independent sections, a meta-data header and bulk data body

with the objective of reducing the size of the disk write each time the archiver samples the IDB.

The meta-data header at the start of the file describes the elements contained in the bulk data, generating CPU, type of data etc. The first word of the file indicates the size of this description, allowing it to be read into memory. This description contains all the information needed to calculate the (constant) size of each bulk data write. Using the archive rate, the position of data from a specific time can be calculated relative to the file head. It is possible that the requested rate may not be achieved, or the archive task may get swapped out by another process or thread, so each data write needs a time stamp.

The use of a meta-data header reduces the amount of data that must be written each time the IDB is sampled to a time-stamp and the numerical values calculated from the VMON records. However, this optimisation comes at a price, the system only works if the elements contained in the bulk data write are always written in the same order, and no elements are added or removed. If a manager stops sending data the file must be padded with error values and if a manager starts transmitting after the meta-data has been written the file must be closed and a new one begun.

It should be noted that archive speed and simplification of the recovery client have been chosen over disk space considerations. There is no attempt to perform compression of the data at writing time, not even a simple zero suppression. Such things would change the bulk data size from disk write to disk write and thus prevent random access of the archive file[13].

3.4.5.3 Recovery

Archiving data is pointless without some mechanism for recovering this data and displaying it. Two requirements must be considered when designing the recovery mechanism.

1. Rapid recovery of the specific data required.
2. Usability of the interface.

Recovery speed is very important. The archiver writes about 10 kbytes to disk every write when running on the full BABAR DAQ system. If it is run at the design frequency of 1 Hz then this produces files of about 1 Gbytes in a twenty-four hour period. Reading the whole file should be as rapid as possible, but with files of this size it is even more important to be able to utilise random access to extract only the information required.

Due to the fixed size of bulk data writes it is possible to calculate how far through the file it is necessary to move the file read pointer to obtain data from the requested time interval. After moving to the calculated offset, which happens instantaneously on a human time scale,

[13]Compression of the output file was retrofitted to the application by the use of a UNIX pipe which applies gzip compression to the file as it is being written to disk. The file must be unzipped before being recovered.

the performance is limited by the disk speed, not by the processing power. Typically, it takes seven seconds to retrieve any amount of information from one hour's worth of data.

3.4.6 Graphical User Interface

All the VMON components described in the previous sections have a common GUI called `vmondisplay`. Early on in the design process the decision was made to write the VMON display application in C++ using the ROOT libraries for the user interface and for data display [15]. Since the version of ROOT that was evaluated (2.23.12) was not thread-safe, all ROOT activity had to be confined to one thread. This was implemented by queueing all the display activities to the same thread. Figures 3-9 and 3-10 show examples of VMON output. Figure 3-9 is an example of a two dimensional histogram as it appears in the real-time display while figure 3-10 is typical of the display of a quantity recovered from the archive.

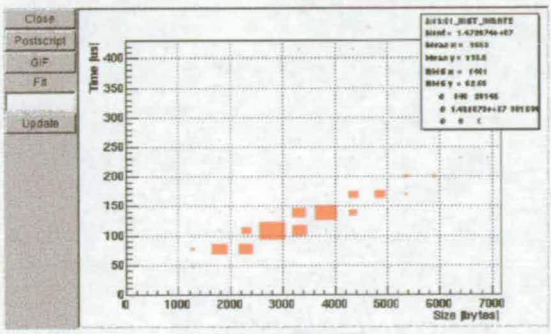

Figure 3-9. *Example of a two dimensional VMON histogram. Input event size vs processing time for one ROM.*

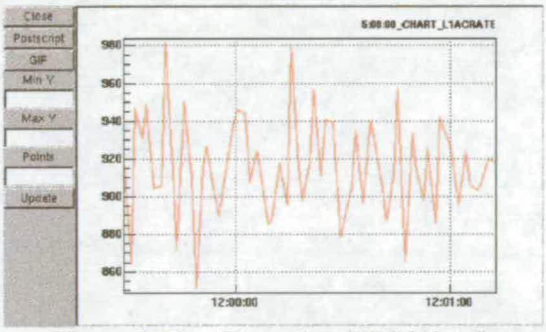

Figure 3-10. *Example of VMON strip chart. L1 Accept rate.*

3.4.7 VMON in Action

To demonstrate how VMON can be used to diagnose problems associated with the Data Acquisition system two examples are given. In each case the VMON output used by Dataflow experts to identify the cause of the problem is shown alongside the equivalent display during normal running.

3.4.7.1 DCH FEE Reset

Periodically the DCH FEE would reset themselves. For a long time the only way to detect this problem was through the data quality monitoring displays. These displays present data distributions averaged over an entire run of data-taking, so using these plots to identify precisely when the fault occurred is impossible. However, the precise timing of each incident

is needed to allow logs to be checked so that the cause of the reset may be identified; VMON was used to provide the precise timing required.

Figures 3-11 and 3-13 were extracted from a VMON archive that spans a DCH FEE reset. Alongside each is the same histogram taken from another archive that was created during a period of smooth running on a different day. Figures 3-11 and 3-12 show the data damage suffered by events as a function of time. Each of the thirty-two lines corresponds to one bit of the thirty-two bit *damage word* accompanying each event. Each bit indicates a different error condition that can occur during the Data Acquisition process. Under normal conditions (figure 3-12) there are no errors and none of the error bits are set for any event. Each of the lines is flat. When there are problems, one or more of the error bits is set for one or more of the events in a sample, and there is a spike on one or more of the lines. Figure 3-11 features two such spikes on several lines. This indicates that an error occurred just before 01:30. The specific damage bits that are set are only crude indicators of where within the system the problem might lie, and other VMON histograms must be examined to identify the source of the errors.

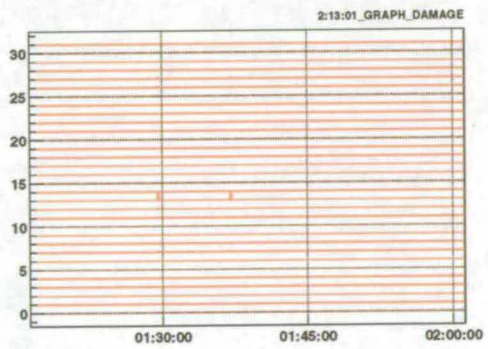

Figure 3-11. *Number of events with any one of 32 damage bits set vs time.*

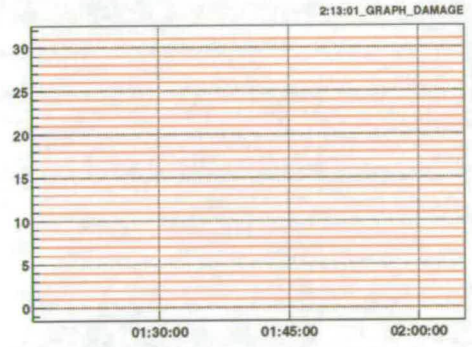

Figure 3-12. *During normal running no damage bits are set.*

Figures 3-13 and 3-14 show the event size, in bytes, for the same DCH crate as a function of time. Figure 3-14 shows a period of normal running. The event size smoothly varies over time, decreasing with luminosity. The sharp rise at 01:30 is caused by a PEP-II top off. Running stops and when it resumes the event size is 20% larger due to the increase in luminosity. The two spikes around 01:50 are produced by periods of shortlived high backgrounds. Figure 3-13 shows the analogous plot taken from the VMON archive spanning the DCH FEE reset. The step in the event size at 01:30 is the result of part of the DCH ceasing data transmission. This is the signature of the DCH FEE reset.

Using the precise timing obtained from the VMON archive, DCH log files were examined and faulty hardware identified. Prior to the deployment of VMON this problem plagued *BABAR* for two years, defying all other attempts at resolution.

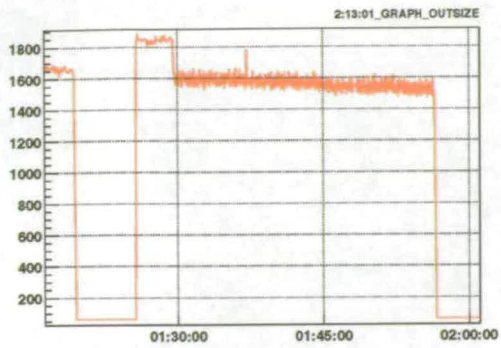

Figure 3-13. *Event size from the DCH vs time shows a sharp drop at the time of the error.*

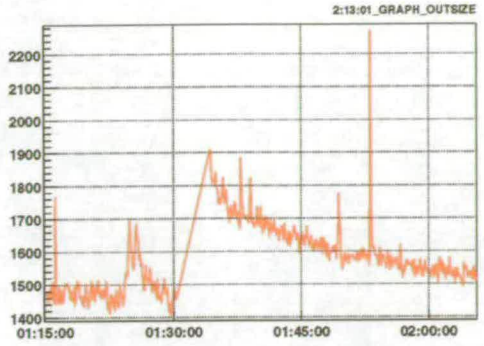

Figure 3-14. *During stable running the event size decreases slowly over time. This particular plot has spikes indicating occasionally background bursts.*

3.4.7.2 High Deadtime

Deadtime occurs when the Data Acquisition system cannot record data because it is still handling the previous event. During normal running the Data Acquisition system has close to zero deadtime, but occasionally the deadtime rises to very high levels, inhibiting data-taking. High deadtime is usually caused by poor beam conditions, but occasionally a fault within the DAQ system will also produce high deadtime. Prior to the deployment of VMON it was not always easy to identify the root cause of a period of high deadtime.

Figures 3-15, 3-17 and 3-19 are extracted from a VMON archive spanning one such period of high deadtime. Figures 3-15 and 3-16 show the deadtime fractions for each of the thirty-two crates of the DAQ system, as a function of time. Figure 3-16 is extracted from a VMON archive created during a period of smooth running. Each of the lines is flat, except for a couple of small peaks around 18:15, probably associated with trapped events, which have such large events sizes that they briefly fill up the Dataflow buffering. Figure 3-15 shows a significant period of deadtime shortly after 18:00, following a shorter period of deadtime before 17:40. Multiple crates have significant deadtime for about ten minutes.

The cause of the deadtime is explored by examining the L1 accept rate, which is shown in figures 3-17 and 3-18. Figure 3-18 shows a period of smooth running, spanning a PEP-II top-off starting just before 17:45. Other than the step caused by the top-off, the histogram simply smoothly decreases with the luminosity. Figure 3-17 also spans a PEP-II top-off, which was probably an attempt to improve the beam conditions. The histogram shows numerous spikes before and after this top-off indicating bursts of triggers from high-multiplicity events. This histogram confirms that the DAQ system really was busy collecting data, and the deadtime was not an artifact of some other hardware fault[14]

[14]For example, timing errors in the *BABAR* DAQ system can cause the system to register 100% deadtime even with a very low L1 accept rate.

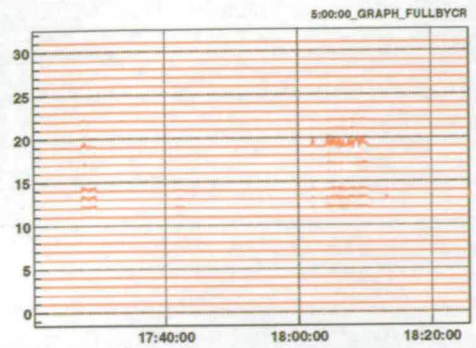

Figure 3-15. *The fraction of dead-time for each Dataflow crate vs time.*

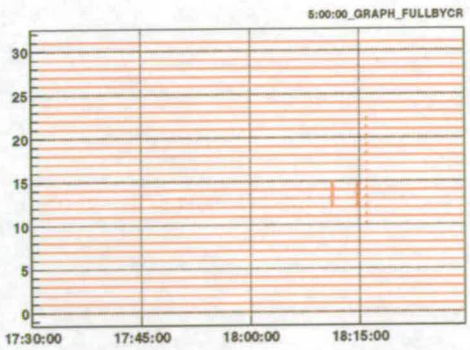

Figure 3-16. *During stable running the dead-time is close to zero.*

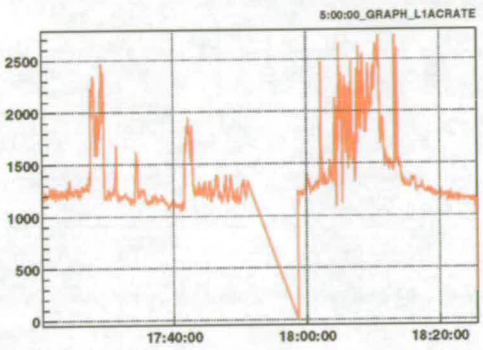

Figure 3-17. *Level 1 accept rate vs time.*

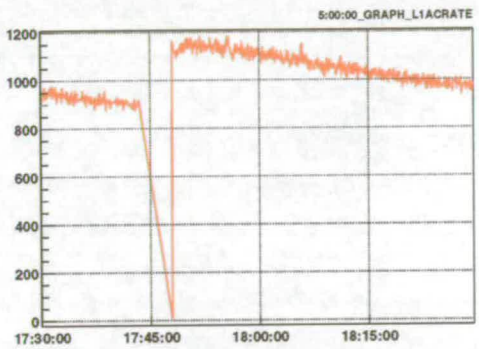

Figure 3-18. *During stable running the L1 Accept rate decreases slowly over time.*

Confirmation that these periods of high deadtime are caused by beam conditions is found from figure 3-19. Figures 3-19 and 3-20 show the total event size as a function of time. Figure 3-20 again shows the PEP-II top-off and a smooth decrease in event size with luminosity. In contrast, figure 3-19 shows large spikes coincident with the spikes in the L1 accept rate. Large, high-multiplicity events are being recorded by the *BABAR* detector, filling the Dataflow buffers and choking data collection.

The ability to quickly verify that *BABAR* is functioning normally when high deadtime prevents efficient data collection allows the PEP-II operators to focus their attention on the true cause of problems.

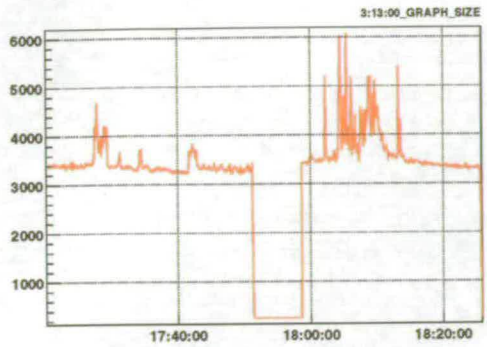

Figure 3-19. *Event size from one crate during the period of high dead-time.*

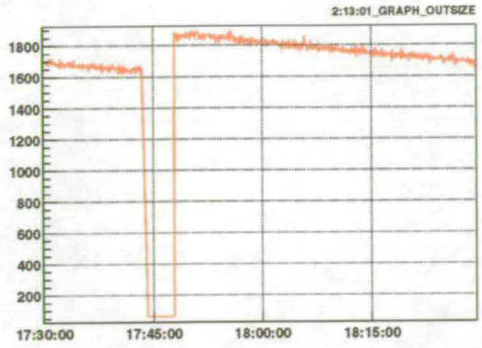

Figure 3-20. *During stable running the event size would decrease slowly over time.*

3.4.8 Evaluation

Presently VMON is used to monitor many different quantities in the 190 CPUs of *BABAR* ODF at a frequency of 1 Hz. It archives this information at 0.2 Hz.[15] At an L1 rate of 3 kHz no visible impact on data acquisition has been observed.

The GUI startup time is less than four seconds on a Sun Ultra5 workstation. The response time for interactive plots is immediate on a human timescale. The CPU usage of the GUI is typically 3%. The memory usage is 36 Mbytes, mostly used by the IDB and by the ROOT libraries. Designing and implementing VMON has required the equivalent of one and a half man years of labour.

3.5 High Luminosity Dataflow

ODF can be pictured as a production line that takes the raw fragments of events from the detector FEEs and pushes complete events into L3. At any given instant, there will be several events in the dataflow system each at a different stage of assembly. Under stable conditions the rate at which Dataflow can run is limited by the slowest member of the production line. A program (*The Model*) has been written which shows how long the event takes to pass though each stage of the process.

The VMON application described in section 3.4 was instrumental to the creation of this model since it is the only application that can measure the performance of each section of the ODF system. The parasitic nature of the monitoring is particularly important because during normal data-taking the event size varies, allowing many of the performance parameters to be plotted

[15] This archive rate has been chosen because most of the other *BABAR* monitoring systems have a precision larger than 5 seconds.

SYS	FESZ	FEXSZ	GLNK	I960	PCIN	MPCN	CPUN	VME	PCI0	MPC0	CPU0	NET	SWTC
SVT	1170	1161	76	34	13	31	96						
								139	26	140	**292**	**348**	
								70	17	93	**222**	**232**	
DCH	8776	2249	**243**	95	75	163	**279**						
								136	34	180	**351**	**450**	
DRC	2485	1251	20	69	24	54	159						
								150	28	150	**308**	**375**	
EMC	9600	140	0	78	73	150	**215**						
								140	11	56	178	140	
	6500	95	0	55	50	102	144						
								95	7	38	151	95	
IFR	3800	824	19	72	32	69	52						
	2700	450	19	64	22	47	52						
	3300	463	19	68	27	57	52						
								88	16	88	**217**	**219**	
EMT	5900	1525	80	63	50	110	172						
								61	11	61	174	152	
DCT	1227	340	19	27	11	23	30						
	507	694	16	33	6	16	98						
	397	283	13	17	4	10	51						
								73	10	53	164	132	
GLT	610	830	73	6	8	20	20						
								41	6	33	133	83	
BBR	984657	51726											26

Figure 3-21. *Projection of the typical time(μs) to process an event with Low energy ring current 4500* mA *and High energy ring current 1500* mA *which are the predicted currents in December 2005.*

against event size, permitting a crude extrapolation to the larger event sizes expected at higher luminosity.

As the luminosity goes up two parameters affecting ODF change: the rate of L1 accepts increases, requiring ODF to run at a higher rate; and the backgrounds increase, making each individual event larger. The increased event size causes some ODF activities to slow down at the same time as the system requirements call for these same activities to complete in less time.

Figure 3-21 is a table showing the projected typical processing time for an event with the beam conditions expected in December 2005. The table reads from left to right beginning with the event size (in bytes) before and after feature extraction and then giving the time taken (in μs) to pass through each stage of ODF. The table is split into subsystem and split again for those subsystems that have ROMs with different behaviour. For example the EMC is split into barrel and endcap sections. The key point to note is that the rate at which ODF can transport events is limited by the largest time in the table. The numbers in underlined, bold, red text are all those points that prevent ODF from running at the target 5 kHz.

The strategy pursued, once each process in the ODF system has been characterised, is to focus on the member of the production line that is predicted to run the slowest at the target luminosity.

3.5.1 Examples of ODF Bottlenecks

Two examples of bottlenecks in Dataflow are presented, along with the proposed solutions.

3.5.1.1 Master ROM

Some of the Master ROMs will limit the rate at which ODF can run in the future. In figure 3-21 the SVT, DCH and IFR all have CPU0 times over 200μs. The proposed solution is to split crates, that is to add extra (logical) VME crates and move some of the slave ROMs from each of the existing crates to the new crates. Since the new crates each contain fewer slave ROMs there will be less data to transport, reducing the CPU usage in each master ROM significantly. This solution is not infinitely scalable since the number of crates the Dataflow system can contain is limited to thirty-two.

3.5.1.2 Level 3

It became clear in 2001 that Offline Prompt Reconstruction would not survive an increase in the L3 output rate. The trigger needs to be made more efficient so that the fraction of useful events increases. It was estimated that, in the long term, the processing power of the L3 farm needs to increase by a factor of ten.

A simple way to increase the processing power of a farm of machines is to add more nodes. Unfortunately, the number of nodes was fixed by the number of bits in an unsigned integer (thirty-two on a PowerPC) since unsigned integers were used as bit masks representing the farm. These bit masks were all identified and replaced by a general bit mask class using an array of unsigned integers, leaving no software limit on the number of farm nodes. In the longer term the complete solution is expected to involve moving to the Intel architecture to allow cheaper, faster CPUs to be purchased to replace the existing SUN Ultra5 workstations.

3.6 Chapter Summary

The high luminosity of the PEP-II B Factory permits the *BABAR* detector to produce a large data set, but without a robust Data Acquisition system to transport this data into storage, this high luminosity would be wasted. To permit the maintenance and development of such a system a monitoring application was written and deployed. This application has proved invaluable for identifying faults and bottlenecks within the Dataflow system.

4

Motivation for the Study of Radiative Penguin Decays

4.1 Introduction

The study of radiative penguin decays in the B meson system provides the opportunity to calculate some interesting theoretical parameters from experimental results. This chapter will first introduce the Cabibbo-Kobayashi-Maskawa (CKM) matrix, which is central to the Standard Model description of rare B decays, then give a pair of examples, showing that CKM matrix elements can be calculated from the inclusive penguin decay $b \to s\gamma$ and the exclusive decay $B \to \omega\gamma$.

4.2 The Cabibbo-Kobayashi-Maskawa Matrix

Presented by Kobayashi and Maskawa in 1973 this 3×3 unitary matrix relates the weak eigenstates (d', s', b') and the mass eigenstates (d, s, b) of the $\frac{-e}{3}$ quarks.

$$\begin{pmatrix} d' \\ s' \\ b' \end{pmatrix} = \begin{pmatrix} V_{ud} & V_{us} & V_{ub} \\ V_{cd} & V_{cs} & V_{cb} \\ V_{td} & V_{ts} & V_{tb} \end{pmatrix} \begin{pmatrix} d \\ s \\ b \end{pmatrix} \tag{4.1}$$

There are several parameterisations of the CKM matrix. The form recommended by the Particle Data Group [9] was proposed by Chau and Keung in 1984, and uses three angles, $\theta_{12}, \theta_{23}, \theta_{13}$, and a phase δ [1].

$$\begin{aligned} V_{CKM} &= \begin{pmatrix} 1 & 0 & 0 \\ 0 & c_{23} & s_{23} \\ 0 & -s_{23} & c_{23} \end{pmatrix} \begin{pmatrix} c_{13} & 0 & s_{13}e^{-i\delta} \\ 0 & 1 & 0 \\ -s_{13}e^{i\delta} & 0 & c_{13} \end{pmatrix} \begin{pmatrix} c_{12} & s_{12} & 0 \\ -s_{12} & c_{12} & 0 \\ 0 & 0 & 1 \end{pmatrix} \\ &= \begin{pmatrix} c_{12}c_{13} & s_{12}c_{13} & s_{13}e^{-i\delta} \\ -s_{12}c_{23} - c_{12}s_{23}s_{13}e^{i\delta} & c_{12}c_{23} - s_{12}s_{23}s_{13}e^{i\delta} & s_{23}c_{13} \\ s_{12}c_{23} - c_{12}c_{23}s_{13}e^{i\delta} & -c_{12}s_{23} - s_{12}c_{23}s_{13}e^{i\delta} & c_{23}c_{13} \end{pmatrix} \end{aligned} \tag{4.2}$$

where, c_{ij} and s_{ij} are shorthand for $\cos\theta_{ij}$ and $\sin\theta_{ij}$. In this parameterisation the angles are defined and labelled in a way that identifies them with the mixing of two specific generations.

[1] θ_{12} can be identified with the Cabibbo angle in the limit $\theta_{23} = \theta_{13} = 0$ when the third generation decouples and the situation reduces to the usual Cabibbo mixing

If one of the angles vanishes so too does the mixing between those two generations. The Chau-Keung parameterisation also allows the identifications

$$V_{ud} = c_{12} \quad V_{us} = s_{12} \quad V_{ub} = s_{13}e^{i\delta} \quad V_{cb} = s_{23} \quad V_{tb} = c_{23} \tag{4.3}$$

to an excellent approximation, since c_{13} deviates from one only in the sixth decimal place. A non-zero magnitude of the phase, δ, generally breaks CP invariance for the weak interaction.

The *BABAR* collaboration makes use of the Wolfenstein approximation to the CKM matrix. Using $\lambda \equiv s_{12}$, the sine of the Cabibbo angle, as an expansion operator this gives

$$V_{CKM} = \begin{pmatrix} 1-\lambda^2/2 & \lambda & A\lambda^3(\rho - i\eta) \\ -\lambda & 1-\lambda^2/2 & A\lambda^2 \\ A\lambda^3(1-\rho-i\eta) & -A\lambda^2 & 1 \end{pmatrix} + \mathcal{O}(\lambda^4). \tag{4.4}$$

where A, ρ, η are real numbers, which were expected to be of order 1.

4.2.1 Unitarity Triangle

If the unitarity condition is applied to pairs of rows or columns of the CKM matrix then nine unitarity conditions are produced, six of which can be represented as triangle in the complex plane.

$$V_{cd}V_{ud}^* + V_{cs}V_{us}^* + V_{cb}V_{ub}^* = 0 \tag{4.5}$$
$$V_{cd}V_{td}^* + V_{cs}V_{ts}^* + V_{cb}V_{tb}^* = 0 \tag{4.6}$$
$$V_{ud}V_{td}^* + V_{us}V_{ts}^* + V_{ub}V_{tb}^* = 0 \tag{4.7}$$
$$V_{us}^*V_{ud} + V_{cs}^*V_{cd} + V_{ts}^*V_{td} = 0 \tag{4.8}$$
$$V_{ub}^*V_{us} + V_{cb}^*V_{cs} + V_{tb}^*V_{ts} = 0 \tag{4.9}$$
$$V_{ub}^*V_{ud} + V_{cb}^*V_{cd} + V_{tb}^*V_{td} = 0 \tag{4.10}$$

It turns out that the current experimental bounds on the CKM matrix elements result in very flat triangles for relations 4.5, 4.6, 4.8 and 4.9. The triangle used to study unitarity in the B meson system is derived from relation 4.10.

The corresponding triangle is shown in figure 4-1 along with a rescaled form with two vertices fixed at (0,0) and (0,1). This is achieved by dividing equation 4.10 through by $|V_{cb}^*V_{cd}|$ and choosing a phase convention where $V_{cb}^*V_{cd}$ is real. The coordinates of the remaining vertex conveniently become the Wolfenstein parameters $(\bar{\rho}, \bar{\eta})$, where

$$\bar{\rho} = \rho\left(1 + \frac{\lambda^2}{2} + \mathcal{O}\left(\lambda^4\right)\right), \quad \bar{\eta} = \eta\left(1 - \frac{\lambda^2}{2} + \mathcal{O}\left(\lambda^4\right)\right) \tag{4.11}$$

The three angles of the unitarity triangle, α, β and γ are, given by

$$\alpha = \arg\left(-\frac{V_{td}V_{tb}^*}{V_{ud}V_{ub}^*}\right), \quad \beta = \arg\left(-\frac{V_{cd}V_{cb}^*}{V_{td}V_{tb}^*}\right), \quad \gamma = \arg\left(-\frac{V_{ud}V_{ub}^*}{V_{cd}V_{cb}^*}\right).$$

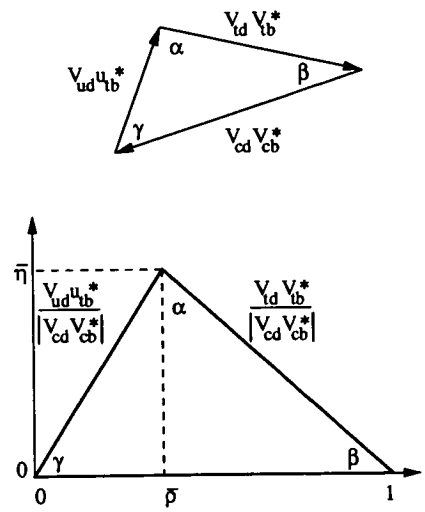

Figure 4-1. *The unitarity triangle before and after rescaling.*

4.2.2 Experimental Constraints

The CKM matrix elements have been constrained by experimental results to the ranges of values given in equation 4.12 [9]. The unitarity constraints connect different elements so that fixing a value for one may limit the ranges of others.

$$\begin{pmatrix} 0.9741 - 0.9756 & 0.219 - 0.226 & 0.0025 - 0.0048 \\ 0.219 - 0.226 & 0.9732 - 0.9748 & 0.038 - 0.044 \\ 0.004 - 0.014 & 0.037 - 0.044 & 0.9990 - 0.9993 \end{pmatrix} \tag{4.12}$$

These constraints are typically presented graphically by indicating the experimentally allowed regions for $(\bar{\rho}, \bar{\eta})$ on the complex plane [16]. Figure 4.2.2 shows the current experimental constraints on the off-axis vertex of the unitarity triangle.

The allowed region for $(\bar{\rho}, \bar{\eta})$ has been constrained by ϵ_k, measured from CP violation in Kaon decays; Δm_s and Δm_d, measured in $B\overline{B}$ mixing; and V_{ub} obtained from $b \rightarrow u$ decays. The recent measurements of $sin2\beta$ from BABAR[3] and BELLE[4] are in good agreement with these existing constraints.

4.3 Radiative Penguin Decays

Flavour Changing Neutral Currents (FCNC) are second order weak processes. In the Standard Model there is no direct coupling between the b and the s or d quarks. A sequence of two charged currents forming a virtual loop can produce an effective FCNC with a branching

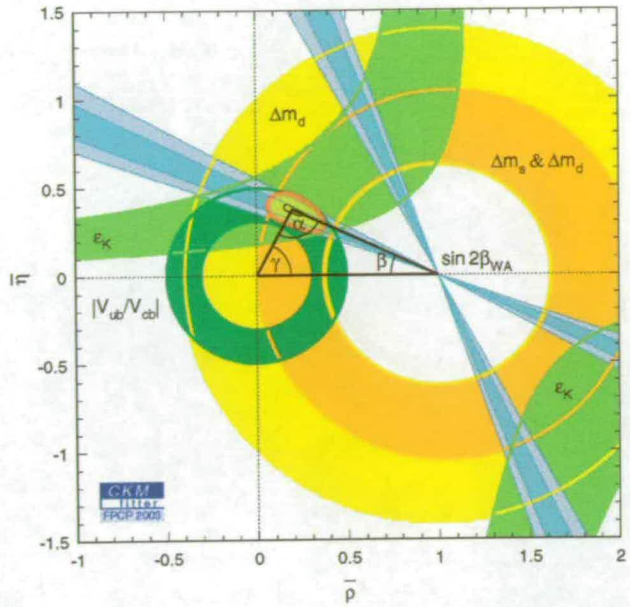

Figure 4-2. *Experimentally allowed regions for $(\bar{\rho}, \bar{\eta})$ on the complex plane.*

fraction $\mathcal{O}\left(10^{-4}\right)$. An example of a virtual loop is shown in figure 4-3. The b quark couples to a W boson and an up-type quark, usually a top quark, then the up-type quark and W boson couple to an d quark, forming the loop and completing the transition. To conserve momentum a particle must be emitted from the loop. A radiative penguin decay[2] is a special case where the particle radiated is a real photon. In a two-body exclusive decay, such as $B \to \omega\gamma$, the photon will have a well defined energy ($E_\gamma \approx \frac{m_b}{2}$), broadened by the Fermi motion of the b quark in the B meson, giving these decays a distinctive event signature.

As can be seen from the diagram, the amplitude for a radiative penguin decay will depend on CKM matrix elements. Standard Model loops involve the heaviest particles (t, W, Z), which means $b \to s\gamma$ is sensitive to $|V_{ts}|$, but such a decay will also be sensitive to extensions to the standard model involving heavy charged Higgs Bosons or super-symmetric particles. In fact the first distinct signs of super-symmetry could come from deviations from Standard Model predictions in the $b \to s$ transitions [18], manifested as an enhanced branching fraction for $B \to \rho\gamma$, or as large direct CP violation effects in $B \to K^*\gamma$ and $B \to \rho\gamma$, for example.

4.4 Feynman Diagrams

The Feynman Diagrams for the decay modes considered in this thesis are shown in figures 4-3, 4-4 and 4.4.

[2]The name *penguin* was applied to one-loop Feynman diagrams by John Ellis in 1977. The story behind this can be found in [17] and elsewhere.

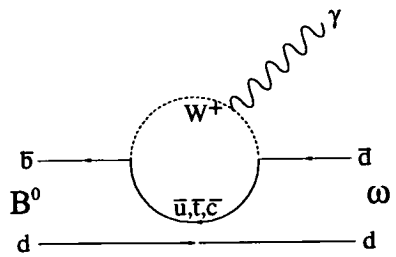

Figure 4-3. *Feynman diagram for* $B \to \omega\gamma$.

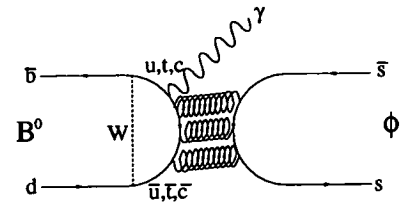

Figure 4-4. *Feynman diagram for* $B \to \phi\gamma$.

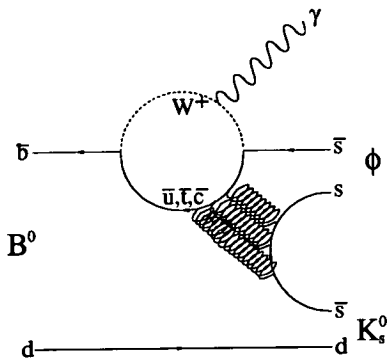

Figure 4-5. *Feynman diagram for* $B \to \phi K\gamma$.

4.5 Calculation of $|V_{ts}|$ from the Inclusive decay $b \to s\gamma$

This section gives a short summary of the theoretical calculation of one CKM element from the experimentally determined branching fraction $\mathcal{B}(b \to s\gamma)$. More details can be found in [19] - [29]

Penguin processes are described using the operator product expansion formalism. The heavy degrees of freedom are integrated out to produce an effective Hamiltonian which depends on the underlying theory. For the Standard Model

$$\mathcal{H}_{eff}(b \to s\gamma) = \frac{-4G_F}{\sqrt{2}} \lambda_t \sum_{i=1}^{6} C_i(\mu)\, \mathcal{O}_i(\mu) + C_{7\gamma}(\mu)\, \mathcal{O}_{7\gamma}(\mu) + C_{8G}(\mu)\, \mathcal{O}_{8G}(\mu) \quad (4.13)$$

where $\lambda_t \equiv |V_{tb}V_{ts}^*|$ contains the relevant CKM matrix elements, C_i are the Wilson Coefficients, $\mathcal{O}_i$ are the local operators with dimension < 6 and μ is the renormalisation scale.

The operators from equation 4.13 can be split into three classes

1. Current-Current operators

$$\mathcal{O}_1 = (\bar{s}_i c_j)_{V-A} (\bar{c}_j b_i)_{V-A}$$
$$\mathcal{O}_2 = (\bar{s}c)_{V-A} (\bar{c}b)_{V-A}$$

2. QCD Penguin Operators

$$\mathcal{O}_3 = (\bar{s}b)_{V-A} \sum_q (\bar{q}q)_{V-A}$$
$$\mathcal{O}_4 = (\bar{s}_i b_j)_{V-A} \sum_q (\bar{q}_j q_i)_{V-A}$$
$$\mathcal{O}_5 = (\bar{s}b)_{V-A} \sum_q (\bar{q}q)_{V+A}$$
$$\mathcal{O}_6 = (\bar{s}_i b_j)_{V-A} \sum_q (\bar{q}_j q_i)_{V+A}$$

3. Magnetic Penguin Operators

$$\mathcal{O}_{7\gamma} = \frac{e}{8\pi^2} m_b \bar{s}_i \sigma^{\mu\nu} (1+\gamma_5) b_i F_{\mu\nu}$$
$$\mathcal{O}_{8G} = \frac{g}{8\pi^2} m_b \bar{s}_i \sigma^{\mu\nu} (1+\gamma_5) T^a_{ij} b_j G^a_{\mu\nu} \tag{4.14}$$

These operators can be used with the effective Hamiltonian, and the requirement that the amplitude in the full theory is reproduced by the corresponding amplitude in the effective theory, to find the Wilson Coefficients.

The most important feature of the Operator Product Expansion is the factorisation of short-distance and long-distance effects. The Wilson coefficients describe features of the theory at scales $> \mu$ while the operators describe features at scales $< \mu$. For sufficiently large μ the Wilson coefficients can be calculated perturbatively so μ is usually chosen to be $\mathcal{O}(M_W)$ and then evolved down to $\mathcal{O}(m_b)$ using renormalisation group equations.

The branching fraction for $B \to X_s\gamma$ is conventionally written in terms of the branching fraction for $B \to Xl\nu_l$.

$$\mathcal{B}(B \to X_s\gamma) = \left[\frac{\Gamma(B \to X_s\gamma)}{\Gamma(B \to Xl\nu_l)}\right]^{th} \mathcal{B}(B \to Xl\nu_l) \tag{4.15}$$

with the theoretical part expressed as

$$\left[\frac{\Gamma(B \to X_s\gamma)}{\Gamma_{SL}}\right]^{th} = \frac{|\lambda_t|^2}{V_{cb}^2} \frac{6\alpha}{\pi f(z)} F\left(|D|^2 + A\right) \tag{4.16}$$

where $f(z)$ is the phase space factor in $\mathcal{B}(B \to Xl\nu_l)$ and $\alpha = e^2/4\pi$. The function F includes the QCD correction to the semileptonic decay width, and the argument $|D|^2 + A$ contains the Wilson coefficients (D), the bremsstrahlung corrections (A) and the virtual corrections (also A) needed for the cancellation of infrared divergences. This factor has been calculated at next-to-leading order [24] to give the the inclusive decay branching fraction in terms of the semileptonic branching fraction and a ratio of CKM matrix elements

$$\mathcal{B}(B \to X_s\gamma) = \frac{|\lambda_t|^2}{V_{cb}^2} \times \mathcal{B}(B \to Xl\nu_l) \times (3.58 \pm 0.30) \times 10^{-3} \tag{4.17}$$

Using the ratio

$$\frac{|\lambda_t|^2}{V_{cb}^2} = \frac{|V_{tb}V_{ts}^*|^2}{V_{cb}^2} = 0.976 \pm 0.010 \tag{4.18}$$

and taking $\mathcal{B}(B \to Xl\nu_l) = 0.1087 \pm 0.0018 \pm 0.0030$ [30], equation 4.15 yields the prediction

$$\mathcal{B}(B \to X_s\gamma) = (3.80 \pm 0.34) \times 10^{-4} \tag{4.19}$$

From the experimentalists perspective, the more interesting calculation takes the branching fractions as input and calculates the CKM matrix element ratio. The current experimental values are given in table 4.5. Taking the unofficial world average gives

Experiment	$\mathcal{B}(b \to s\gamma) \times 10^{-4}$ $mean \pm stat \pm syst \pm model$
CLEO 1995 [32]	$2.32 \pm 0.57 \pm 0.35$
ALEPH 1998 [33]	$3.11 \pm 0.80 \pm 0.72$
BELLE 2001 [34]	$3.36 \pm 0.53 \pm 0.42^{+0.50}_{-0.54}$
CLEO 2001 [35]	$3.21 \pm 0.43 \pm 0.27^{+0.18}_{-0.10}$
BABAR 2002 [36]	$3.88 \pm 0.36 \pm 0.37^{+0.43}_{-0.23}$
BABAR 2002 [37]	$4.3 \pm 0.5 \pm 0.8 \pm 1.3$
Unofficial World Average [38]	$3.47 \pm 0.23 \pm 0.32 \pm 0.35$

Table 4-1. *Branching Fraction measurements for $b \to s\gamma$.*

$$\frac{|\lambda_t|^2}{V_{cb}^2} = \frac{|V_{tb}V_{ts}^*|^2}{V_{cb}^2} = 0.89 \pm 0.08 \tag{4.20}$$

Measurements of $\mathcal{B}(b \to s\gamma)$ are already limited by statistics and theoretical uncertainties, but the uncertainty on this measurement must improve by an order of magnitude to compete with the existing constraints on the CKM matrix elements.

4.6 Determination of Wolfenstein Parameters ρ and η

The parameters ρ and η, which appear in the Wolfenstein approximation to the CKM matrix, can be determined from the exclusive radiative B decays $B \to V + \gamma$ where $V = K^*, \rho, \omega$. The calculation is dependent on reliable estimates of the short-distance (SD) and long-distance (LD) contributions to the decay amplitudes.

The magnetic operator, $\mathcal{O}_{7\gamma}$, is responsible for the SD-contribution in the decays $B \to K^*\gamma$, $B \to \rho\gamma$ and $B \to \omega\gamma$. If only these contributions are considered then relationships between the exclusive decays rates can be found, for example

$$\frac{\Gamma(B \to \rho\gamma)}{\Gamma(B \to K^*\gamma)} \simeq \kappa_{u,d}\left[\frac{|V_{td}|}{|V_{ts}|}\right]^2 \tag{4.21}$$

where $\kappa_i \equiv [F_s(B_i \to \rho\gamma)]^2 / [F_s(B_i \to K^*\gamma)]^2$ and the form factors F_s have been calculated [21]. The ratio in equation 4.21 is dependent on CKM matrix elements and form factors but is independent of both the t mass and the renormalisation scale, μ. Assuming the SD-physics dominates, and that the form factors for the decays $B^0 \to \rho^0\gamma$ and $B \to \omega\gamma$ are the same, relationships between various decay rates can be established

$$\Gamma(B^\pm \to \rho^\pm\gamma) = 2\Gamma(B^0 \to \rho^0\gamma) = 2\Gamma(B \to \omega\gamma) \tag{4.22}$$

It should be noted that the equality between the ρ and ω decay rates receives SU(3)-breaking corrections that may be as large as 20% [31]; these are neglected in equation 4.22.

The decays $B \to X_s\gamma$ and $B \to K^*\gamma$ are consistent with the SD-contributions being dominant and it is believed that the CKM-suppressed exclusive decays are also dominated by SD-physics, however the LD-contributions need to be calculated on a case-by-case basis. In $B \to V\gamma$ decays the dominant LD-contributions come from the four-Fermion operators $\mathcal{O}_1$ and $\mathcal{O}_2$ and these contributions can be estimated using the light-cone QCD sum rule approach. Since parity conserving and parity violating amplitudes turn out to be close, the ratio of LD- and SD- contributions reduces to a number.

For $B^\pm \to \rho^\pm\gamma$

$$\frac{\mathcal{A}_{long}}{\mathcal{A}_{short}} = R_{L/S}^{B^\pm \to \rho^\pm\gamma} \cdot \frac{V_{ub}V_{ud}^*}{V_{tb}V_{td}^*} \tag{4.23}$$

where $R_{L/S}^{B^\pm \to \rho^\pm\gamma}$ has been evaluated [22], at the scale $\mu = 5\,\text{GeV}$, to be -0.30 ± 0.07. The analogous LD-contributions to the neutral B decays $B^0 \to \rho^0\gamma$ and $B \to \omega\gamma$ are much smaller since they are colour suppressed. In fact the ratio of LD to SD contributions, $R_{L/S}^{B^0 \to \rho^0\gamma} \simeq R_{L/S}^{B \to \omega\gamma}$, is at most 0.05. A rough estimate of the ratio $\mathcal{A}_{long}/\mathcal{A}_{short}$ may be obtained by taking the central value from the CKM fits, giving $|V_{ub}|/|V_{td}| \simeq 0.39$, resulting in

$$\left|\frac{\mathcal{A}_{long}}{\mathcal{A}_{short}}\right|^{B^\pm \to \rho^\pm\gamma} = |R_{L/S}^{B^\pm \to \rho^\pm\gamma}| \frac{|V_{ub}V_{ud}|}{|V_{td}V_{tb}|} \simeq 0.1 \tag{4.24}$$

The neutral mode has a much smaller ratio

$$\left|\frac{\mathcal{A}_{long}}{\mathcal{A}_{short}}\right|^{B^0 \to \rho^0\gamma} \leq 0.02 \tag{4.25}$$

The smallness of the LD-contributions to the $B^0 \to \rho^0\gamma$ decay is supported by an analysis based on the soft-scattering of on-shell hadronic decay products $B \to \rho^0\rho^0 \to \rho\gamma$ [28], and implies that it is safe to neglect these contributions.

Including only colour-allowed LD-contributions, the relations 4.22 become

$$\frac{\Gamma(B^\pm \to \rho^\pm\gamma)}{2\Gamma(B^0 \to \rho^0\gamma)} = \frac{\Gamma(B^\pm \to \rho^\pm\gamma)}{2\Gamma(B \to \omega\gamma)} = 1 + \Delta(R_{L/S}) \tag{4.26}$$

with $R_{L/S} \equiv R_{L/S}^{B^\pm \to \rho^\pm\gamma}$ and

$$\Delta(R_{L/S}) = 2 \cdot R_{L/S} V_{ud} \frac{\rho(1-\rho) - \eta^2}{(1-\rho)^2 + \eta^2} + (R_{L/S})^2 V_{ud}^2 \frac{\rho^2 + \eta^2}{(1-\rho)^2 + \eta^2} \tag{4.27}$$

where η and ρ are Wolfenstein parameters.

The ratio of CKM suppressed decays to CKM allowed decays is also modified by the inclusion of LD-contributions. We continue to ignore the LD-contributions in $\Gamma(B \to K^*\gamma)$ because isospin violation and direct CP violation are both small [40]. The 30% uncertainty in the form factor ensures that the theoretical determination of

$$R_{K^*} = \frac{\Gamma(B \to K^*\gamma)}{\Gamma(B \to X_s\gamma)} \tag{4.28}$$

assuming SD-dominance is in agreement with experimental results from CLEO [41]. Thus,

$$\frac{\Gamma(B^\pm \to \rho^\pm\gamma)}{\Gamma(B^\pm \to K^{*\pm}\gamma)} = \kappa_u\lambda^2\left[(1-\rho)^2+\eta^2\right]\left(1+\Delta\left(R_{L/S}\right)\right) \tag{4.29}$$

The LD-effects are small, but non-negligible, introducing an uncertainty that is comparable to the $\sim 15\%$ uncertainty in the overall normalisation due to the $SU(3)$-breaking effects in κ_u

Since it is safe to neglect the colour-suppressed LD-contributions to neutral B meson decays the SD-dominated ratio is retained

$$\frac{\Gamma\left(B^0 \to \rho^0\gamma, \omega\gamma\right)}{\Gamma(B^0 \to K^*\gamma)} = \kappa_d\lambda^2\left[(1-\rho)^2+\eta^2\right] \tag{4.30}$$

This simplification suggests that these are the optimal ratios to measure. The form factors

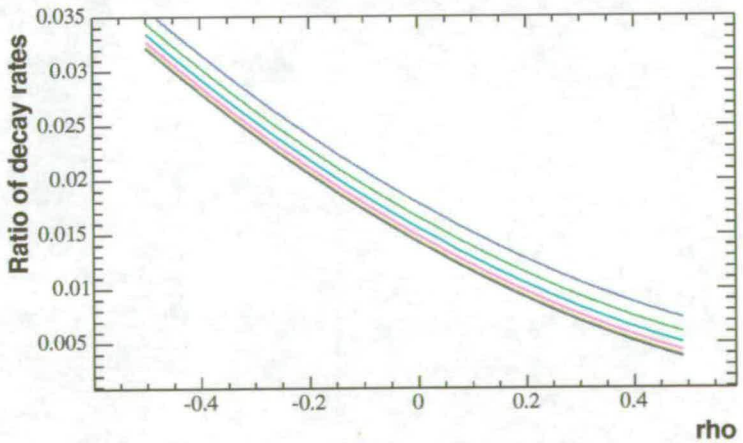

Figure 4-6. *The ratio of decay widths vs ρ for $\eta = 0, 0.1, 0.2, 0.3.0.4, 0.5$ ($\eta = 0$ is the bottom curve).*

have been calculated [23] and can be used to evaluate κ_d

$$\kappa_d \equiv \frac{\left|F_s(B_d \to \rho\gamma)\right|^2}{\left|F_s(B_d \to K^*\gamma)\right|^2}\Phi_d = \frac{\left|F_s(B_u \to \rho\gamma)\right|^2}{2\left|F_s(B_d \to K^*\gamma)\right|^2}\Phi_d \tag{4.31}$$

where Φ_d is the phase space factor

$$\Phi_d = \frac{\left(m_b^2 + m_d^2\right)}{\left(m_b^2 + m_s^2\right)} \frac{\left(m_{B^0}^2 - m_\rho^2\right)^3}{\left(m_{B^0}^2 - m_{K^*}^2\right)^3} \tag{4.32}$$

giving

$$\kappa_d = \frac{(0.24 \pm .04)^2}{2\,(0.32 \pm 0.05)^2} \times 1.02 = 0.29 \pm 0.07 \tag{4.33}$$

Selecting several values for η within the permitted range (equation 4.12) and plotting the ratio of neutral B meson decay widths vs ρ for these selections produces the graph in figure 4.6. It is clear that, while the ratio of decay widths has a strong dependence on ρ, the dependence on η is rather weak. It is also clear that an accurate measurement of this ratio would restrict the permitted values of η and ρ (see section 6.1). Finally, using the measured branching ratio $\mathcal{B}\left(B^0 \to K^*\gamma\right) = (4.23 \pm 0.63) \times 10^{-5}$ [42] and restricting the Wolfenstein parameters to the allowed range, the branching ratio for $B \to \omega\gamma$ is predicted to be $(0.6 \pm 0.4) \times 10^{-6}$.

4.7 Chapter summary

The Cabibbo-Kobayashi-Maskawa matrix element $|V_{ts}|$ can be constrained with a precise measurement of $\mathcal{B}\left(B \to X_s\gamma\right)$. By inverting this constraint, and using the current experimental bound on the CKM matrix elements, a prediction of $\mathcal{B}\left(B \to X_s\gamma\right) = (3.80 \pm 0.34) \times 10^{-4}$ can be made. Furthermore, the Wolfenstein parameters ρ and η can be constrained with precise measurements of $\mathcal{B}\left(B^0 \to K^*\gamma\right)$ and $\mathcal{B}\left(B \to \omega\gamma\right)$ or $\mathcal{B}\left(B^0 \to \rho^0\gamma\right)$. New Physics, such as super-symmetry, may have a large effect on the Branching Fractions of one-loop decays, so radiative penguins may provide the first indication of what lies beyond the Standard Model.

5

Search for Rare Radiative Penguin Decays

5.1 Introduction

This chapter presents the searches for three radiative Penguin decay modes, $B \to \omega\gamma$, $B \to \phi\gamma$, and $B^0 \to \phi K_S^0\gamma$. This chapter begins by providing an overview of the analysis procedure and very briefly describes the event processing that occurs before an individual analysis is performed.

The bulk of this chapter is dedicated to defining the event selection variables used in these analyses (section 5.6). Plots comparing the distributions of each variable for the samples of background and signal events are shown, and the merits of each variable discussed. Following the event selection, the extraction of signal events from data is presented (section 5.7). The result for each mode could either be a significant signal, leading to a measurement of the branching fraction, or no significant signal, leading to an upper limit on the branching fraction. In either case, the analysis is finished off by identifying the sources of systematic uncertainty and calculating the magnitude of the systematic and statistical uncertainties (section 5.9).

For these analyses, the following event samples were used; 82 fb^{-1} of on-peak data, 9.1 fb^{-1} of off-peak data , 95 fb^{-1} of simulated $B\overline{B}$ events, 61 000 simulated $B \to \omega\gamma$ events, 42 000 simulated $B \to \phi\gamma$ events, and 11 500 simulated $B^0 \to \phi K_S^0\gamma$ events.

5.2 Analysis Method

The full chain of data analysis can be summarised as consisting of seven basic steps:

Simple candidate reconstruction Charged tracks and neutral clusters are identified and categorised.

Event filter Events in the event store that have the general characteristics of a radiative penguin decay are identified.

Composite candidate reconstruction The charged tracks, neutral clusters and other objects within each event are used to form possible parent particles.

Background suppression Candidates failing to meet selection criteria are rejected.

Background estimation The number of background events that pass the selection is estimated.

Systematic uncertainty Sources of systematic uncertainty are identified and quantified.

Calculation of branching fraction or upper limit The number of events, efficiency of the candidate selection and the size of the data sample are used to calculate the branching fraction or upper limit.

5.3 Simple Candidate Reconstruction

Candidate reconstruction starts in Offline Prompt Reconstruction (OPR), a process which follows data collection and fills the database used for analysis. DCH and SVT hits are associated with charged tracks, while isolated EMC energy deposits become neutral clusters. These are classified by quality, and sorted into several lists of particle candidates. For completeness, the selection criteria applied to candidates included in the lists used by these analyses are given here, and in section 5.5.

The analyses presented in this thesis all draw from the same set of particle lists. All photons come from the list called `goodPhotonLoose`. This list is composed of isolated neutral clusters with a minimum energy of 0.03 GeV and a maximum lateral moment of 0.8.

The lateral moment of a shower in the EMC is defined as

$$\frac{\sum_{1=3}^{N} E_i r_i^2}{\sum_{i=3}^{N} E_i r_i^2 + E_1 r_0^2 + E_2 r_0^2} \tag{5.1}$$

where N is the number of crystals in the shower; E_i is the energy deposited in the i^{th} crystal, ordered such that $E_1 > E_2 > ... > E_N$; r_i is the distance between the centre of the i^{th} crystal and the center of the shower in a plane perpendicular to a line from the shower centre to the interact point and r_0 is the average distance between two crystals ($\approx 5\,\mathrm{cm}$). Electrons and photons distribute their energy in a few crystals so removing the two crystals containing the highest energy in the cluster from the sum in the numerator of equation 5.1 ensures that the corresponding lateral moment will be small. By contrast, when multiple particles strike the EMC too close together to be resolved, as is the case when a pi-zero decays to two photons close to the EMC, the shower energy will be distributed over a large number of crystals and the lateral moment will be high.

The highest energy photon in the events will also meet the criteria specified by the event filter (section 5.4). All charged pions and kaons are drawn from the `goodTracksLoose` list. This list is formed from charged tracks that have a transverse momentum greater than 0.1 GeV/c with a minimum of twelve DCH hits. The Distance of Closest Approach (DOCA) can be no more than 1.5 cm from the interaction point in the XY plane and no more than 10 cm in the Z direction.

5.4 Event Filter

An individual analysis at *BABAR* considers events recovered from a database filled by the event reconstruction software. During the reconstruction phase, events are tagged with a pattern of bits that describe the broad characteristics of the event. This allows an analysis to be restricted to a subset of the data, considerably decreasing processing times. One of these tag bits indicates that an event meets the requirements set by the Radiative Penguin Analysis Working Group. Such events have at least three charged tracks with minimum transverse momenta of 0.1 GeV/c and maximum momenta of 10 GeV/c. In addition these tracks are required to have a minimum of twenty hits in the DCH. The highest energy photon in the event has an energy, in the centre of mass system, in the range 1.5 GeV to 3.5 GeV. Additionally, the ratio of the Fox-Wolfram Second Moment to the Zeroth moment, R_2, for the event must be no greater than 0.9.

The ratio of the Second Fox-Wolfram Moment to the Zeroth moment provides a measure of the sphericity of an event by considering the momenta of all the charged and neutral decay products. R_2 is defined as the ratio $\frac{H_2}{H_0}$ where

$$H_l = \sum_{i,j} \frac{|\vec{p_i}||\vec{p_j}|}{E^2} P_l\,(cos\phi_{ij}) \tag{5.2}$$

The indices i and j run over all charged tracks and neutral clusters in the event. ϕ_{ij} is the angle between the directions of flight for particles i and j. P_l is the lth Legendre polynomial. E is the total energy of the event. When the event is very jet-like, the value of R_2 is close to one, but when the decay products are distributed spherically, this value tends to zero. Hence, a cut of $R_2 < 0.9$ removes events that are very jet-like.

5.5 Composite Candidate Reconstruction

The analysis software starts by using the simple candidate lists generated by OPR (section 5.3) to create composite candidate lists, which are then used to form the B meson candidates.

Pairs of photon candidates from the photon list are combined through a simple four-vector sum to produce a list of neutral pion candidates. Only candidates with a mass between 0.115 GeV/c^2 and 0.150 GeV/c^2 are included in the neutral pion list. K-Short candidates are similarly created from the four-vector sums of oppositely charged tracks, although these tracks are not drawn from the `goodTracksLoose` list, since it would not be appropriate to use tracks with a DOCA cut applied. The K-Short candidates are required to have a mass between 0.3 GeV/c^2 and 0.7 GeV/c^2, but no other cuts are applied. In particular the decision to apply a decay length cut is delegated to the author of a particular analysis.

5.5.1 Kaon Identification

Both the charged kaons and charged pions are drawn from the same candidate list generated by OPR, `goodTracksLoose`. When a candidate from this list is used to reconstruct another particle, kaon identification routines are used to establish whether the candidate is likely to be a pion or a kaon. The kaon identification uses dE/dX information from the SVT and DCH, and Čerenkov photons from the DRC to assign likelihoods to the particle identification hypotheses. Several different selectors are available that require different levels of confidence in a particular hypothesis [44].

In the analyses presented in this thesis, all charged kaons are required to pass the `kaonTight` selector. This selector uses SVT and DCH information to assign likelihoods for candidates with momenta below 0.5 GeV/c, and the DCH only for candidates with momenta between 0.5 GeV/c and 0.6 GeV/c. Above 0.6 GeV/c input from the DRC is required, and provides the most important information, but the DCH is also utilised. Requiring DRC information to be available for a track with momentum greater than 0.6 GeV/c to pass the `kaonTight` selector introduces a theta angular acceptance cut on these tracks. The `kaonTight` selector requires that the kaon likelihood be eighty times greater than the pion likelihood if the candidate momentum is greater than 2.7 GeV/c, and fifteen times greater if the candidate momentum is between 0.5 GeV/c and 0.7 GeV/c. For all other candidate momenta, the selector becomes a straight comparison of likelihoods. These values are chosen to ensure that the kaon mis-identification is kept below 5% for momenta up to 4 GeV/c.

All charged pions are required to **fail** the `notAPion` selector. This selector is intended to remove all the obvious pion candidates without effecting the kaon efficiency. Hence, a failure indicates that a track is an obvious pion and removes kaons efficiently. The selector uses SVT and DCH information to assign likelihoods for candidates with momenta below 0.7 GeV/c and the DRC for candidates with momenta above 0.6 GeV/c. For candidates with momenta below 0.5 GeV/c the candidate will be treated as a charged pion if the pion likelihood is ten times larger than the kaon likelihood. For all other momenta, this selector becomes a straight comparison of likelihoods.

5.5.2 Vector Meson Reconstruction

The dominant decay mode of the omega meson is to three pions, two oppositely charged and one neutral, (89%) [9]. The charged tracks are required to **fail** the `notAPion` selector. The decay vertex is calculated from the tracks and the neutral pion is constrained to originate from the same point. The `GeoKin` [45] vertex fitting algorithm is then applied to provide the mass of the omega candidate, along with the probability that a true vector meson decay could be reconstructed to give a vertex resembling the candidate vertex.

Phi mesons decay predominantly to two oppositely charged kaons (49%) [9]. The charged tracks are required to pass the `kaonTight` selector. For each pair of oppositely charged

kaons in the event the GeoKin [45] vertex fitting algorithm is used to calculate a vertex, a composite particle mass, and the probability that a true vector meson decay could be reconstructed to give a vertex resembling the candidate vertex.

5.5.3 B Reconstruction

B meson reconstruction is done using the four-vector sum of the daughter particle four-momenta. The omega and phi mesons decay strongly so their flight paths are negligible and the decay vertex can be taken to be the B meson decay vertex. The typical resolution on the B decay position, using the beam axis constraint, is 101 μm in x, 10 μm in y and 115 μm in z.

The complete set of reconstruction requirements is given in table 5-1.

Variable	Range	Units
Photon energy	1.5, 3.5	GeV
Lateral moment	< 0.8	
Number of Tracks	> 2	
Track transverse momentum	0.1, 10	GeV/c
XY distance of closest approach	< 1.5	cm
Z distance of closest approach	< 10	cm
Ratio of second to zeroth Fox-Wolfram moment	< 0.9	
Pi-zero mass	0.155, 0.150	GeV/c^2
K-short mass	0.3, 0.7	GeV/c^2
Beam Energy Substituted Mass (section 5.6.1)	5.2,5.3	GeV
ΔE (section 5.6.2)	-1.5, 0.5	GeV

Table 5-1. *Requirements on candidates used in B reconstruction.*

5.6 Background Suppression

The various candidate and event selection variables used in these analyses are defined here and plots comparing the distributions of these parameters for truth-matched simulated signal events, simulated $B\overline{B}$ events and off-peak data are presented. For presentation purposes the histograms of simulated signal and simulated $B\overline{B}$ event distributions have been scaled up to have the same number of events as the corresponding off-peak histogram (see table 5-2). At this stage no selection cuts have been performed.

Decay mode	# signal events	# $B\overline{B}$ events	# off-peak events
$B \to \omega\gamma$	5088 (61k)	61521 (99750k)	185861 (9555k)
$B \to \phi\gamma$	4668 (42k)	1538 (99750k)	2795 (9555k)
$B^0 \to \phi K_S^0\gamma$	662 (11.5k)	1207 (99750k)	3755 (9555k)

Table 5-2. *Number of events in histograms after reconstruction and filtering but before selection. Number of events in the initial sample is given in parentheses.*

5.6.1 Beam Energy Substituted Mass (M_{ES})

The B meson mass is given by

$$m_B = \sqrt{E_B^2 - p_B^2} \tag{5.3}$$

The accuracy with which the mass of a reconstructed B meson can be determined depends on the accuracy of the measurements of all the daughter particle energies. This can lead to a large uncertainty in the B meson mass. If the calculation is performed in the centre of mass frame then the B meson energy in equation 5.3 can be replaced with the beam energy, using the fact that the $\Upsilon(4S)$ decays to two particles of equal mass. This improves the accuracy of the calculated B meson mass, since the energy of the beams is quite well known.

$$M_{ES} = \sqrt{E_{Beam}^{*2} - p_B^{*2}} \tag{5.4}$$

The M_{ES} distributions for the three decay modes are shown in plots 5-1, 5-2 and 5-3. All three plots look very similar. In each case, the background samples follow the same ARGUS shape [46] (see section 5.7). The signal distribution has a very different shape, being sharply peaked about the B mass, 5.279 GeV/c^2. There is a small tail at low mass caused by energy losses as the neutral daughter particles, particularly the high energy photon, traverse the detector. In particular, energy is lost through pre-conversion of photons in the DRC and leakage of the shower energy in the EMC.

Unlike the other variables presented in this chapter, there are no cuts on M_{ES}. After all the other selection cuts have been performed, the M_{ES} distribution for the selected data is fitted to provide a signal yield. Full details are provided in section 5.7.

5.6.2 ΔE

ΔE is simply the difference between the expected B energy (E_{Beam}^*) and the measured B energy (E_B^*), which is derived from the measured energies of the decay products; where both E_{Beam}^* and E_B^* are measured in the centre of mass frame.

$$\Delta E = E_{Beam}^* - E_B^* \tag{5.5}$$

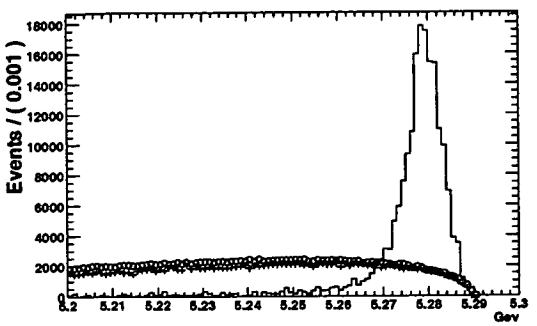

Figure 5-1. *Simulated signal (solid line), simulated $B\overline{B}$ (crosses) and off-peak data (open circles) $B \to \omega\gamma$ distributions in M_{ES}.*

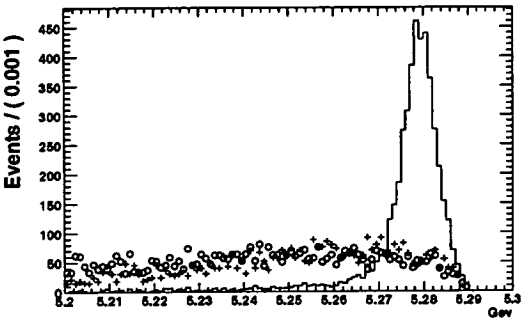

Figure 5-2. *Simulated signal (solid line), simulated $B\overline{B}$ (crosses) and off-peak data (open circles) $B \to \phi\gamma$ distributions in M_{ES}.*

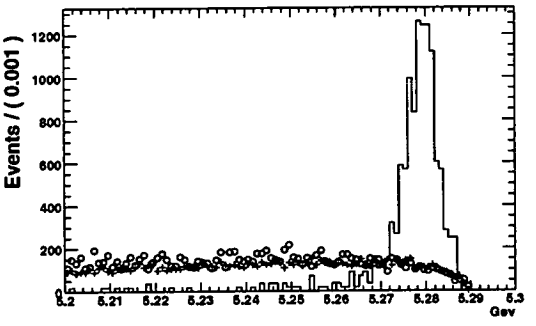

Figure 5-3. *Simulated signal (solid line), simulated $B\overline{B}$ (crosses) and off-peak data (open circles) $B^0 \to \phi K_S^0\gamma$ distributions in M_{ES}.*

The ΔE distributions for each of the decays modes are shown in figures 5-4, 5-5 and 5-6. The plots are all largely the same; the signal distribution is peaked around zero, with a low energy tail mostly due to energy losses from the high-energy photon. The background shape can be modelled as an exponential in the region around $\Delta E = 0$. The selection windows for all the variables are indicated on these plots by vertical (blue) lines. The method for setting these windows is given in section 5.6.11. For the ΔE cut the optimisation results in rejecting a significant portion of the signal sample (see table 5-6 for the selection efficiencies). Some analyses relax this cut to increase statistics, but the presence of significant background from other radiative Penguin decays at low ΔE motivated the retention of the tighter cut.

5.6.3 Meson Mass

Given that there may be many charged tracks and photons in a $B\overline{B}$ event, many phi, omega and K-short candidates can be formed, some of them fakes. To eliminate this combinatorial

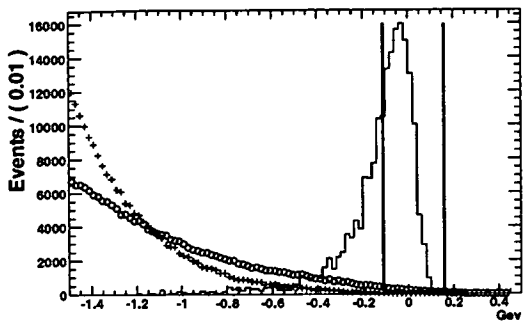

Figure 5-4. *Simulated signal (solid line), simulated $B\overline{B}$ (crosses) and off-peak data (open circles) $B \to \omega\gamma$ distributions in ΔE.*

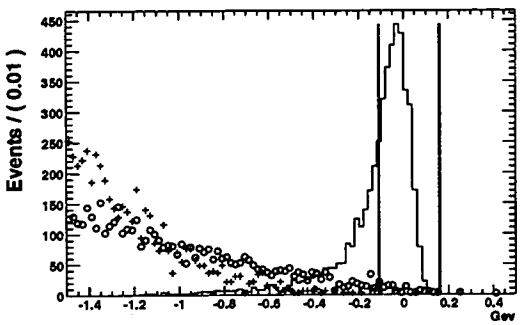

Figure 5-5. *Simulated signal (solid line), simulated $B\overline{B}$ (crosses) and off-peak data (open circles) $B \to \phi\gamma$ distributions in ΔE.*

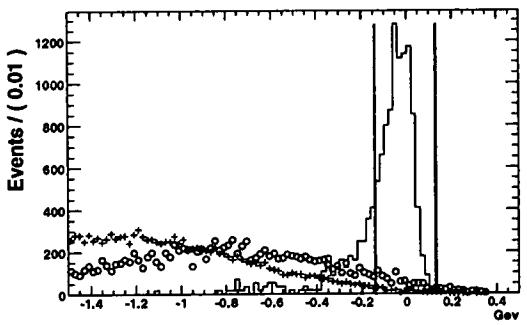

Figure 5-6. *Simulated signal (solid line), simulated $B\overline{B}$ (crosses) and off-peak data (open circles) $B^0 \to \phi K_S^0\gamma$ distributions in ΔE.*

background, meson candidates are selected by their mass. Random combinations of background particles will produce random invariant masses, whilst the recombination of daughter particles for a real meson will produce a particle with a mass close to the Particle Data Group value [9]. The PDG masses are $0.782\,\mathrm{GeV/c^2}$, for the omega meson; $1.020\,\mathrm{GeV/c^2}$, for the phi meson; and $0.498\,\mathrm{GeV/c^2}$, for the K-short meson.

Figures 5-7 and 5-8 show the omega and phi meson mass distributions for $B \to \omega\gamma$ and $B \to \phi\gamma$ respectively. Figures 5-9 and 5-10 show the phi and K-short meson mass distributions for $B^0 \to \phi K_S^0\gamma$. All four figures show the expected meson mass peak for the samples of simulated signal events, but the background samples produce very different distributions.

The absence of a significant omega mass peak in the background distributions of $B \to \omega\gamma$ (figure 5-7) indicates that the background for this mode is largely combinatorial, as opposed to being real omegas from some other decay process. In figures 5-8 and 5-9, however, the phi meson backgrounds show the same peak as the simulated signal phi meson. This indicates that

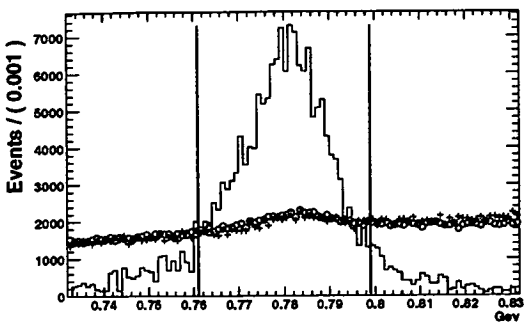

Figure 5-7. *Simulated signal (solid line), simulated $B\overline{B}$ (crosses) and off-peak data (open circles) $B \rightarrow \omega\gamma$ distributions in omega mass.*

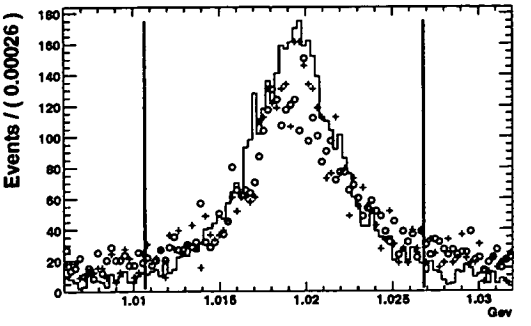

Figure 5-8. *Simulated signal (solid line), simulated $B\overline{B}$ (crosses) and off-peak data (open circles) $B \rightarrow \phi\gamma$ distributions in phi mass.*

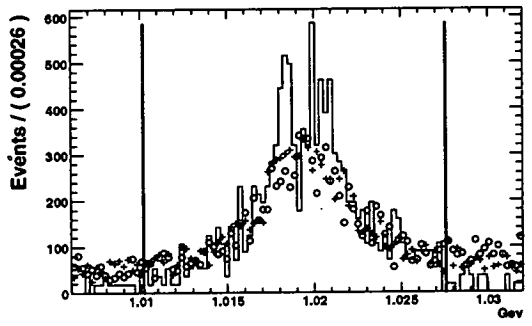

Figure 5-9. *Simulated signal (solid line), simulated $B\overline{B}$ (crosses) and off-peak data (open circles) $B^0 \rightarrow \phi K_S^0\gamma$ distributions in phi mass.*

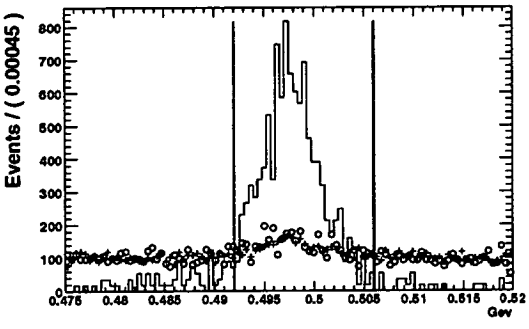

Figure 5-10. *Simulated signal (solid line), simulated $B\overline{B}$ (crosses) and off-peak data (open circles) $B^0 \rightarrow \phi K_S^0\gamma$ distributions in K-short mass.*

the background for this decay mode comes from real phi mesons, rather than combinatorial fakes. Hence the phi meson mass cut does not provide as good separation between signal and background as the equivalent omega mass cut. Figure 5-10 shows no significant K-short mass peak, indicating that there are very few real K-shorts in the background samples.

5.6.4 Helicity Angle

When the pseudo-scalar B meson decays to two vector particles, an omega or phi and a photon, angular momentum must be conserved. The spin of the photon must be balanced by the helicity of the vector meson. When the vector meson decays angular momentum must again be conserved. The helicity angle of the three-body omega decay, Θ_H, is defined as the angle between the B meson momentum (in the ω rest frame) and the normal to the plane defined by the three pions as illustrated in 5-11. In fact it is the cosine of this angle that is

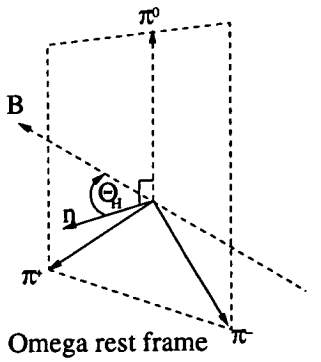

Figure 5-11. *The Omega Helicity angle is defined as the angle between the normal to the plane of the ω decay and the B meson momentum, in the ω rest frame.*

plotted, giving the distributions shown in figure 5-12. As expected, the signal distribution peaks around $cos\Theta_H = 0$. The background distributions exhibit a similar shape to signal, but are somewhat flatter.

The phi helicity angle is more simply defined than the omega helicity angle. It is the angle between the kaon direction and the B meson momentum in the phi rest frame. Despite the slightly different definitions, the signal distributions are comparable (figure 5-12 and figure 5-13). Note, however, that the background shapes are somewhat different. The background distributions for $B \to \phi\gamma$ (figure 5-13) have a completely different shape compared to the signal distribution. Based on these plots, the separation would be expected to be better for $B \to \phi\gamma$.

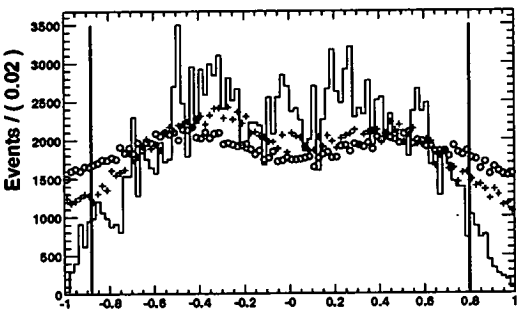

Figure 5-12. *Simulated signal (solid line), simulated $B\overline{B}$ (crosses) and off-peak data (open circles) $B \to \omega\gamma$ distributions in $cos\Theta_H$.*

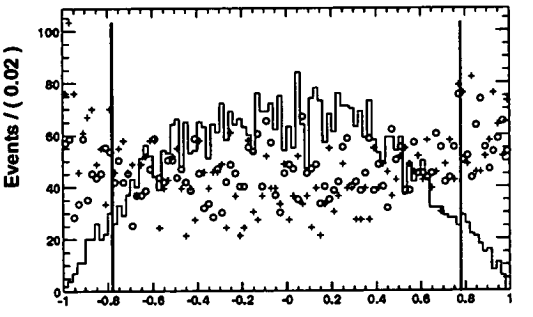

Figure 5-13. *Simulated signal (solid line), simulated $B\overline{B}$ (crosses) and off-peak data (open circles) $B \to \phi\gamma$ distributions in $cos\Theta_H$.*

For the three body mode, $B^0 \to \phi K_S^0\gamma$, the helicity depends on the spin of the ϕK_s system, which is likely to be either 1 or 2, depending on the resonant sub-structure. The $J = 1$ and $J = 2$ portions have different helicity distributions that will tend to obscure any structure

in the phi helicity distribution [47]. Since no model describing this system exists, this distribution is not used in the analysis of $B^0 \to \phi K^0_S \gamma$.

5.6.5 Dalitz Angle

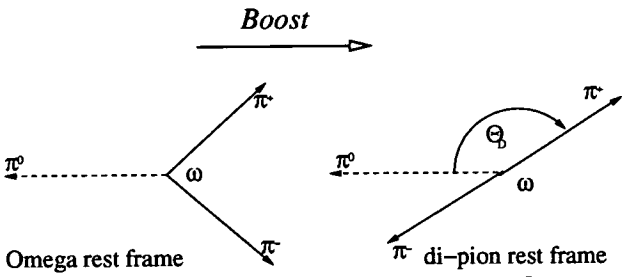

Figure 5-14. *Dalitz angle is defined as the angle between the π^0 and the π^+ in the di-pion rest frame.*

The three body decay of the omega produces three pions which are kinematically constrained. This can be used to reject combinatorial background. Treating the two charged pions as one pseudo-particle called a di-pion, the three pions can be boosted into the di-pion rest frame. In this frame the charged pions propagate back to back, and the line of flight of the neutral pion forms an angle with this axis. This is the Dalitz angle, Θ_D. The distributions of $cos\Theta_D$ are shown in figure 5-15. The signal distribution is peaked around zero, indicating that the momentum of the neutral pion tends to be perpendicular to the di-pion axis in the di-pion rest frame, but the background distributions are essentially flat.

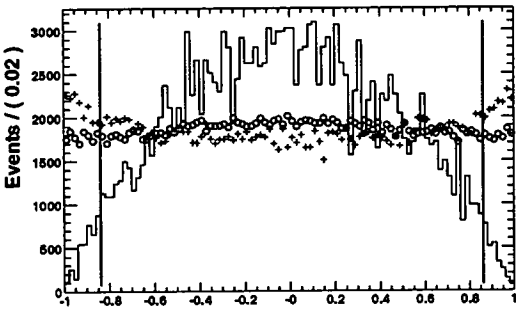

Figure 5-15. *Simulated signal (solid line), simulated $B\overline{B}$ (crosses) and off-peak data (open circles) $B \to \omega\gamma$ distributions in $cos\Theta_D$.*

5.6.6 χ^2 for Vertex Fit and Decay Distance

GeoKin, the algorithm used to calculate the decay vertex of a composite particle from the momentum vectors of its daughter tracks, produces a χ^2 value for each vertex. Events with a high χ^2 are more likely to be incorrectly combined background tracks. Figures 5-16, 5-17 and 5-18 show the χ^2 distributions for the three decay modes considered in this thesis.

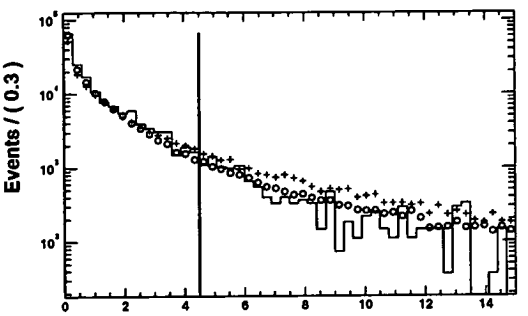

Figure 5-16. *Simulated signal (solid line), simulated $B\overline{B}$ (crosses) and off-peak data (open circles) $B \to \omega\gamma$ distributions in χ^2.*

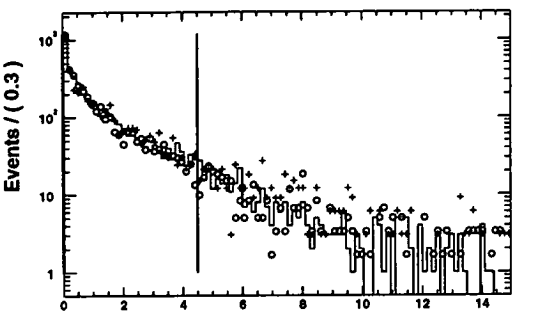

Figure 5-17. *Simulated signal (solid line), simulated $B\overline{B}$ (crosses) and off-peak data (open circles) $B \to \phi\gamma$ distributions in χ^2.*

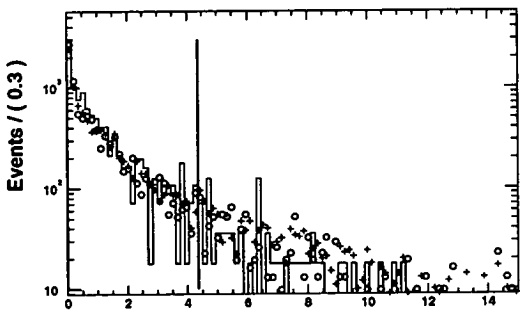

Figure 5-18. *Simulated signal (solid line), simulated $B\overline{B}$ (crosses) and off-peak data (open circles) $B^0 \to \phi K_S^0\gamma$ distributions in χ^2.*

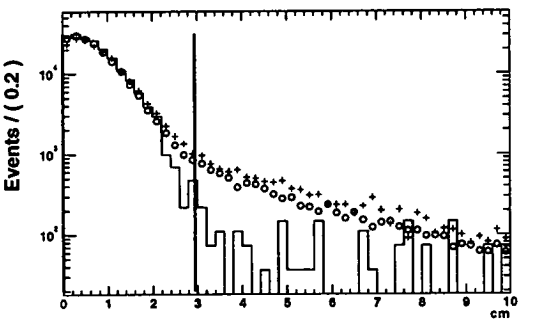

Figure 5-19. *Simulated signal (solid line), simulated $B\overline{B}$ (crosses) and off-peak data (open circles) $B \to \omega\gamma$ distributions in omega decay distance.*

A cut on the omega decay distance eliminates events where the reconstructed omega vertex is very far from the interaction point. The simulated signal, simulated $B\overline{B}$ and off-peak event distributions in decay distance for $B \to \omega\gamma$ are shown in figure 5-19. Reconstructed omega mesons with decay vertices far from the interaction point are likely to be second or third generation offspring of one of the original B mesons. A logical extension of the $B^0 \to \phi K_S^0\gamma$ analysis would be to include a minimum decay distance cut for the K-short to eliminate charged tracks from the primary B vertex.

5.6.7 Photon Production Angle

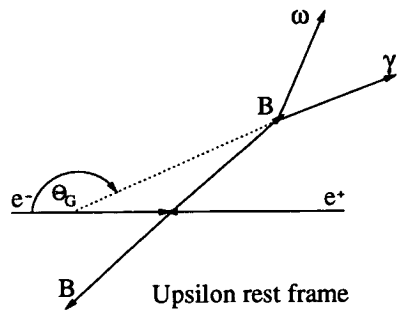

Figure 5-20. *Photon production angle is defined as the angle between the electron beam and photon line of flight in the $\Upsilon(4S)$ rest frame.*

The photon production angle, Θ_γ is defined as the angle between the electron beam and the photon line of flight in the centre of mass frame (see figure 5-20). The signal photon production angle distribution represents the acceptance of the EMC. The lack of events with very acute photon production angles is caused by decay products escaping detection by passing down the PEP-II beam-pipes.

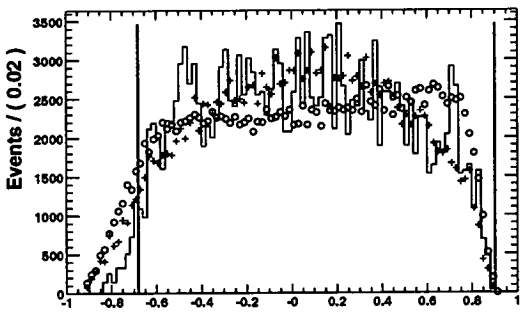

Figure 5-21. *Simulated signal (solid line), simulated $B\overline{B}$ (crosses) and off-peak data (open circles) $B \rightarrow \omega\gamma$ distributions in $cos\Theta_\gamma$.*

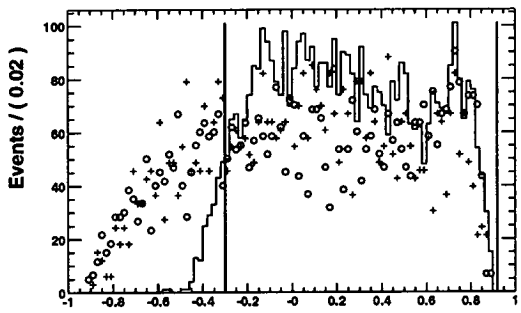

Figure 5-22. *Simulated signal (solid line), simulated $B\overline{B}$ (crosses) and off-peak data (open circles) $B \rightarrow \phi\gamma$ distributions in $cos\Theta_\gamma$.*

In contrast to the $B \rightarrow \omega\gamma$ mode (figure 5-21), the photon production angle for the $B \rightarrow \phi\gamma$ decay mode (figure 5-22) is very asymmetric. This is a direct result of the particle identification requirements on the phi daughter particles. The requirement that these daughters be positively identified as kaons restricts the track acceptance the region covered by the DRC. This leads to rejection of tracks in the more forward regions of the *BABAR* detector and produces a sample of phi's that tend to propagate backwards (in the centre of mass frame).

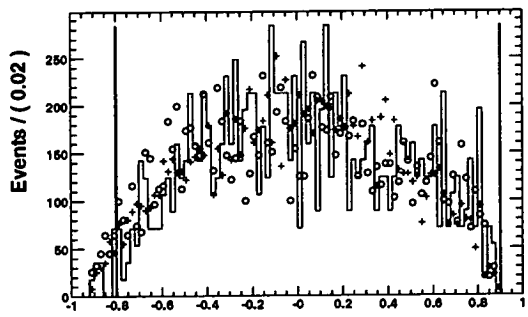

Figure 5-23. *Simulated signal (solid line), simulated $B\overline{B}$ (crosses) and off-peak data (open circles) $B^0 \to \phi K^0_S \gamma$ distributions in $cos\Theta_\gamma$.*

The kinematic constraints between the phi and the photon in a two body decay then produce a photon sample which tends to propagate forwards (in the centre of mass frame).

In contrast, the photon production angle for $B^0 \to \phi K^0_S \gamma$ (figure 5-23) is quite symmetric. The three body nature of the $B^0 \to \phi K^0_S \gamma$ decay breaks the kinematic link between the phi and photon directions, and thus the link between DRC acceptance and photon direction.

5.6.8 Neutral Pion and Eta Vetoes

Neutral pions and eta mesons both decay preferentially to two photons (99% and 39% respectively) [9]. Thus, high energy mesons can produce a high energy photon, causing an event to be erroneously selected as a radiative penguin decay. To protect against this, the high energy photon has neutral pion and eta vetoes applied.

The high energy photon is combined, in turn, with every other photon in the event that passes a minimum energy cut of 50(250) MeV for the neutral pion (eta) veto. If the resulting particle has an invariant mass close to the the Particle Data Group [9] value for either neutral pion (eta) mass of 0.135(0.547) GeV/c^2 then the B meson candidate is rejected. For all decay modes presented in this thesis the neutral pion veto range is [0.115, 0.155] GeV and eta veto range is [0.5073, 0.5873] GeV.

The three pairs of figures in this section show the distributions of the invariant masses of composites formed from pairs of photons in off-peak data events. One pair for each of $B \to \omega\gamma$ (5-24 and 5-25), $B \to \phi\gamma$ (5-26 and 5-27) and $B^0 \to \phi K^0_S \gamma$ (5-28 and 5-29). Unlike other plots in this chapter, the region between the vertical (blue) lines is a veto region, rather than an acceptance region.

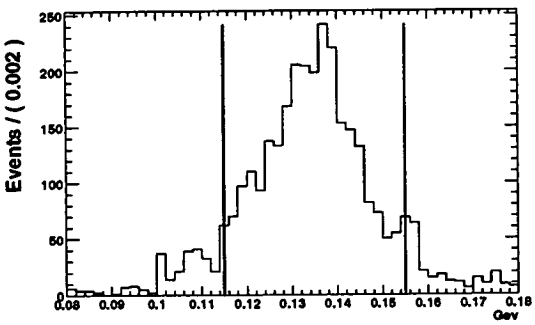

Figure 5-24. *Invariant mass of composites formed, using off-peak data, from the high-energy photon and each other photon in the event with energy greater than* 50 MeV. *Sample reconstructed as* $B \to \omega\gamma$.

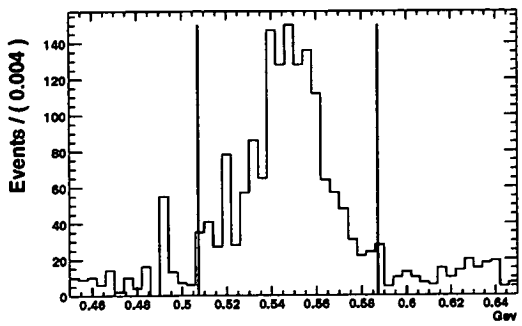

Figure 5-25. *Invariant mass of composites formed, using off-peak data, from the high-energy photon and each other photon in the event with energy greater than* 250 MeV. *Sample reconstructed as* $B \to \omega\gamma$.

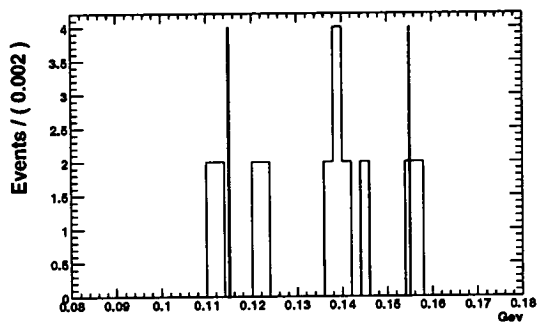

Figure 5-26. *Invariant mass of composites formed, using off-peak data, from the high-energy photon and each other photon in the event with energy greater than* 50 MeV. *Sample reconstructed as* $B \to \phi\gamma$.

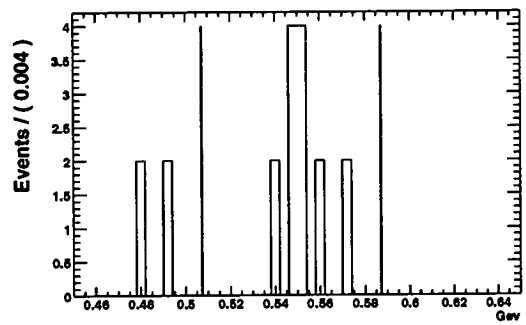

Figure 5-27. *Invariant mass of composites formed, using off-peak data, from the high-energy photon and each other photon in the event with energy greater than* 250 MeV. *Sample reconstructed as* $B \to \phi\gamma$.

5.6.9 Θ_T

Θ_T is defined to be the angle between the photon line of flight and the direction that is the vector sum of the momenta of all the decay products, charged and neutral, in the event that do not originate from the signal B candidate. For continuum events this angle is generally close to either 0 or π, reflecting the jet-like topology of the event. For $B\overline{B}$ events there should be no correlation between the photon line of flight from one B meson and the vector sum of the decay products of the other B. However, looking at the distributions of simulated signal, simulated $B\overline{B}$ and off-peak events for all three modes (figures 5-30, 5-31 and 5-32) it is apparent that some portion of the simulated $B\overline{B}$ event sample exhibits jet-like behaviour. The

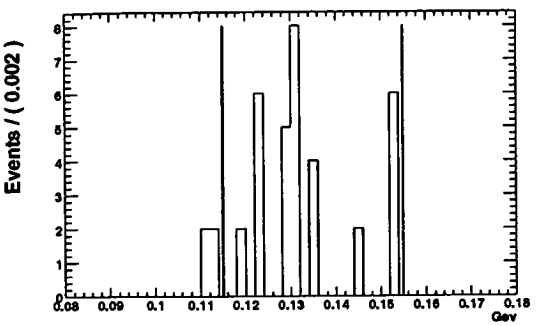

Figure 5-28. *Invariant mass of composites formed, using off-peak data, from the high-energy photon and each other photon in the event with energy greater than* 50 MeV. *Sample reconstructed as* $B^0 \to \phi K^0_S \gamma$.

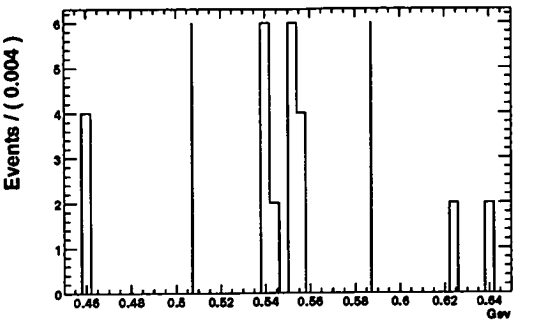

Figure 5-29. *Invariant mass of composites formed, using off-peak data, from the high-energy photon and each other photon in the event with energy greater than* 250 MeV. *Sample reconstructed as* $B^0 \to \phi K^0_S \gamma$.

correlation is introduced as a by-product of the mis-construction of the B meson candidate from the decay products of the two true B mesons in the event. For signal events the photon direction and the vector sum of the decay products of the non-signal B meson are uncorrelated, giving these events a flat $cos\Theta_T$ distribution.

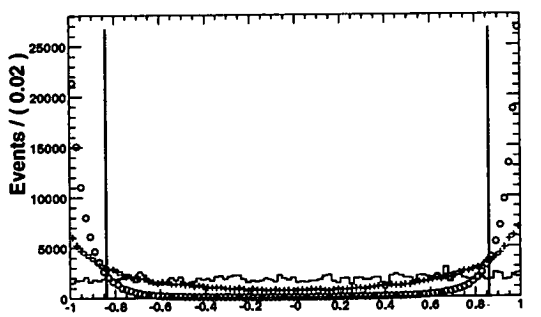

Figure 5-30. *Simulated signal (solid line), simulated* $B\overline{B}$ *(crosses) and off-peak data (open circles)* $B \to \omega\gamma$ *distributions in* $cos\Theta_T$.

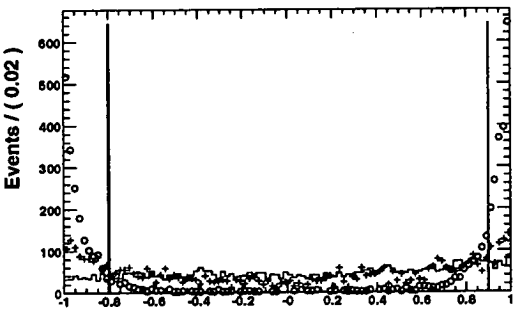

Figure 5-31. *Simulated signal (solid line), simulated* $B\overline{B}$ *(crosses) and off-peak data (open circles)* $B \to \phi\gamma$ *distributions in* $cos\Theta_T$.

5.6.10 Momentum Flow Cones Fisher Discriminant

Sets of correlated variables can be combined to reduce a complex set of interconnected cuts to a cut on a single variable. The single variable used is a Fisher discriminant (Appendix A). The Fisher discriminant used in these analyses is made up of eighteen momentum flow cones.

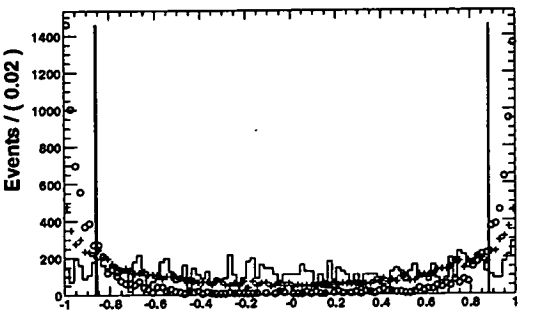

Figure 5-32. *Simulated signal (solid line), simulated $B\overline{B}$ (crosses) and off-peak data (open circles) $B^0 \to \phi K^0_S \gamma$ distributions in $cos\Theta_T$.*

Momentum flow is just the scalar sum of momenta for all particles passing through a region, in this case one of eighteen concentric cones centred on the photon line of flight. For this analysis the B candidate decay products are excluded from the sum and each of the eighteen cones subtends an angle of 10°.

Figures 5-33 through 5-41 show the nine forward momentum flow cones, the histograms for the backward plots are very similar, each labelled by the *inner* angle of the 10° cone. By simple visual comparison it is possible to see the difference between the jet-like continuum events and the isotropic signal events. Continuum events (green line) tend to have more momentum flowing through backward and forward cones whereas the signal events (black line) have momentum flowing equally through all cones.

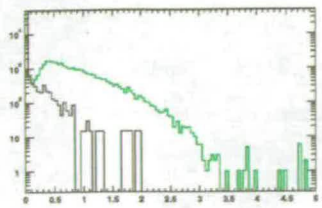

Figure 5-33. 0°

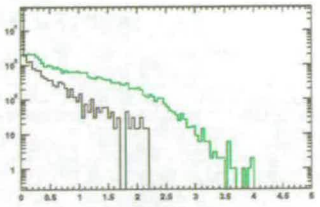

Figure 5-34. 10°

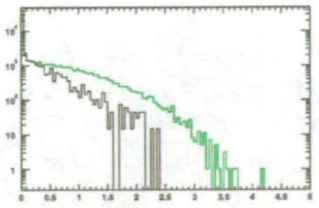

Figure 5-35. 20°

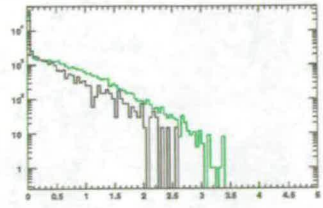

Figure 5-36. 30°

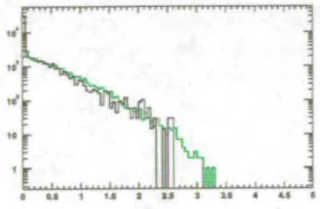

Figure 5-37. 40°

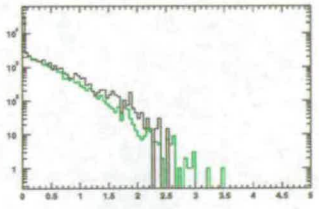

Figure 5-38. 50°

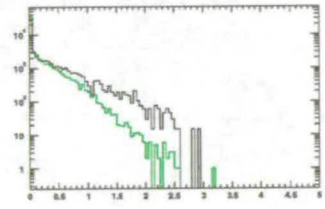

Figure 5-39. 60°

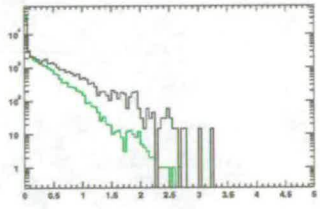

Figure 5-40. 70°

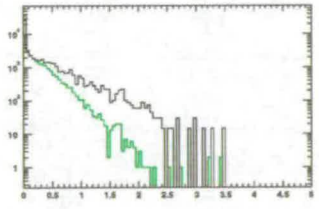

Figure 5-41. 80°

Distribution of $B \to \omega\gamma$ momentum flow through the nine forward cones for simulated signal (solid black) and off-peak data (dotted green).

Using the prescription in Appendix A, taking the off-peak data as a background sample and the simulated signal events as the signal sample, a set of eighteen weights is generated and the weighted sum of momentum cones for each event can be calculated. This weighted sum is the Fisher discriminant. The distributions of the Fisher discriminant for simulated signal events, simulated $B\overline{B}$ events and off-peak data are in figures 5-42, 5-43, and 5-44. The broad features of these plots are all largely the same. Recall that this Fisher discriminant is intended to separate the jet-like off-peak events from signal events. Thus, any $B\overline{B}$ events, made jet-like by the mis-identification of B meson daughters, that are removed by a cut on the Fisher discriminant should be viewed as an added bonus. The simulated signal events form a peak centered around -1, while the off-peak events form a peak centered around $-5 \to -4$. The simulated $B\overline{B}$ events lie between these two extremes, overlapping the signal peak. The vertical (blue) line marks the lower boundary of the acceptance region. The selection cut appears to be very tight, but it must be remembered that these histograms have been scaled to

have the same area on these plots and that the off-peak sample is in reality much larger than the simulated signal sample.

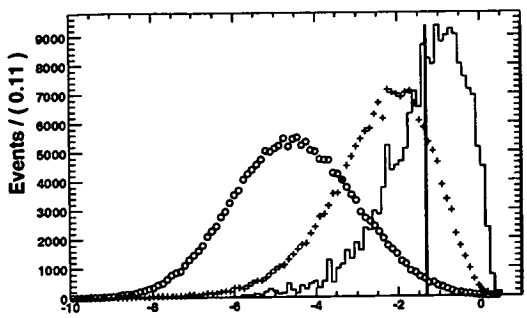

Figure 5-42. *Simulated signal (solid line), simulated $B\overline{B}$ (crosses) and off-peak data (open circles) $B \to \omega\gamma$ distributions of the Fisher discriminant.*

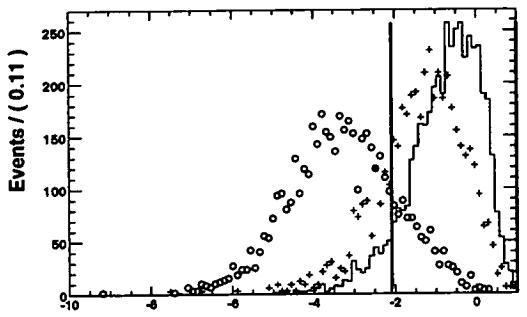

Figure 5-43. *Simulated signal (solid line), simulated $B\overline{B}$ (crosses) and off-peak data (open circles) $B \to \phi\gamma$ distributions of the Fisher discriminant.*

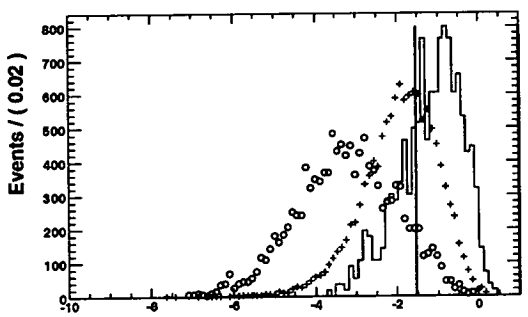

Figure 5-44. *Simulated signal (solid line), simulated $B\overline{B}$ (crosses) and off-peak data (open circles) $B^0 \to \phi K_S^0\gamma$ distributions of the Fisher discriminant.*

5.6.11 Cut Optimisation

The selection cuts are chosen to maximise the observed signal significance. For each mode, the three samples are scaled to the integrated luminosity of the on-resonance data sample used for the signal searches, $82\,\text{fb}^{-1}$. For this scaling the branching fractions for the three modes are assumed to be 1×10^{-6}, which gives the scale factors listed in table 5-3. The off-peak sample is scaled by a factor of 9.01 and the simulated $B\overline{B}$ sample is scaled by a factor of 0.86. The values of the cuts on each of the event variables is chosen to maximise the ratio

$$\frac{S^2}{S+B} \tag{5.6}$$

Mode	Scale factor
$B \to \omega\gamma$	1.48×10^{-3}
$B \to \phi\gamma$	2.16×10^{-3}
$B^0 \to \phi K_S^0\gamma$	3.94×10^{-3}

Table 5-3. *Scale factors for signal samples used in cut optimisation.*

where S is the number of truth-matched simulated signal events surviving the cut, and B is the number of background events surviving the cut. For all variables, except the Fisher discriminant, the number of background events is taken as the scaled sum of simulated $B\overline{B}$ events and off-peak data events combined. The Fisher discriminant cut is optimised using only off-peak data, since this variable is not designed to provide good separation between signal and $B\overline{B}$ events. Care has been taken to ensure that the cut variables are independent and can thus be optimised individually; each variable is optimised using the full set of reconstructed events with no selection cuts applied.

It transpires that the exact (indeed even the approximate) values of the scale factors is largely irrelevant since the cut values found using the method described above barely change as the multiplication factors are varied from unity to a factor of ten below the calculated values. As an example, some of the $B \to \omega\gamma$ cuts found using these different scale factors are given in table 5-4. The full set of selection cuts for all modes is as given in table 5-5.

Variable	No Scaling	Correct Scale Factors	Signal Scale Factor / 10
Vector meson mass	0.761 , 0.799	0.761 , 0.799	0.761 , 0.799
$cos\Theta_H$	-0.92 , 0.88	-0.88 , 0. 8	-0.88 , 0. 8
$cos\Theta_D$	-0.84 , 0.86	-0.84 , 0.86	-0.84 , 0.86
Vertex χ^2	0 , 4.5	0 , 4.5	0 , 4.5
Omega decay distance	0 , 2.35	0 , 2.95	0 , 2.95
$cos\Theta_G$	-0.68 , 0.9	-0.68 , 0.9	-0.68 , 0.9
$cos\Theta_T$	-0.84 , 0.86	-0.84 , 0.86	-0.84 , 0.86
ΔE	-0.17 , 0.16	-0.11 , 0.16	-0.11 , 0.16

Table 5-4. *Effect of varying scale factors on optimised selection cuts.*

5.6.12 B Candidate Selection Efficiency

The efficiency of the event selection has been broken down by cut and is presented in table 5-6. Note that these efficiencies are for the final states $B \to \pi^0\pi^+\pi^-\gamma$, $B \to K^+K^-\gamma$, and $B \to K^+K^-K_S^0\gamma$. The cuts are sequential from the top to the bottom of the table. For comparison the selection "efficiencies" for both background samples is given in tables 5-7 and 5-8.

Selection cuts	$B \to \omega\gamma$	$B \to \phi\gamma$	$B^0 \to \phi K_S^0\gamma$
Vector meson mass	0.761 , 0.799	1.01068, 1.0268	1.01016 , 1.02758
$cos\Theta_H$	-0.88 , 0.8	-0.78 , 0.78	-
$cos\Theta_D$	-0.84 , 0.86	-	-
Vertex χ^2	0 , 4.5	0 , 4.5	0 , 4.365
Omega decay distance	0 , 2.95	-	-
K-short mass	-	-	0.492 , 0.506
$cos\Theta_G$	-0.68 , 0.9	-0.3 , 0.92	-0.8 , 0.9
Neutral pion veto	0.115 , 0.155	0.115 , 0.155	0.115 , 0.155
Eta veto	0.5073, 0.5873	0.5073 , 0.5873	0.5073 , 0.5873
$cos\Theta_T$	-0.84 , 0.86	-0.8 , 0.9	-0.86 , 0.88
Fisher (lower bound)	-1.31	-2.08	-1.53
ΔE	-0.11 , 0.16	-0.11 , 0.16	-0.14 , 0.13

Table 5-5. *Selection criteria.*

Cut Efficiency (%)	$B \to \omega\gamma$	$B \to \phi\gamma$	$B^0 \to \phi K_S^0\gamma$
Reconstruction	8.34	11.11	5.76
Neutral pion veto	100.00	100.00	100.00
Eta veto	100.00	100.00	100.00
Vector meson mass	83.31	92.69	95.34
$cos\Theta_D$	96.61	-	-
Vertex χ^2	88.99	90.29	89.11
Decay distance	99.70	-	-
K-short mass	-	-	89.20
$cos\Theta_H$	95.11	93.05	-
Fisher	56.29	91.57	69.05
$cos\Theta_T$	98.92	89.45	93.97
$cos\Theta_G$	98.29	95.58	98.78
ΔE	64.03	65.11	76.16
Selection	23.80	39.69	36.99
Total efficiency	1.99	4.42	2.14

Table 5-6. *Selection efficiency from simulated signal events.*

5.7 M_{ES} Fits

After the event selection has been performed, the M_{ES} distribution of the remaining events is fit to an ARGUS (for background) plus Crystal Ball (for signal) shape. The Crystal Ball

Cut Efficiency (%)	$B \to \omega\gamma$	$B \to \phi\gamma$	$B^0 \to \phi K_S^0\gamma$
Reconstruction	0.062	0.002	0.001
Neutral pion veto	99.99	100.00	100.00
Eta veto	99.98	100.00	99.97
Vector meson mass	39.85	85.37	83.76
$cos\Theta_D$	83.58	-	-
Vertex χ^2	73.90	85.15	79.74
Decay distance	95.00	-	-
K-short mass	-	-	32.96
$cos\Theta_H$	87.56	69.86	-
Fisher	18.89	78.62	38.27
$cos\Theta_T$	98.49	82.90	95.75
$cos\Theta_G$	93.55	74.46	97.31
ΔE	0.23	0	3.40
Selection	0.008	0.000	0.03

Table 5-7. *Selection efficiency from simulated $B\overline{B}$ events.*

Cut Efficiency (%)	$B \to \omega\gamma$	$B \to \phi\gamma$	$B^0 \to \phi K_S^0\gamma$
Reconstruction	1.95	0.03	0.04
Neutral pion veto	98.70	99.49	98.93
Eta veto	99.27	99.49	99.46
Vector meson mass	41.14	82.43	82.43
$cos\Theta_D$	86.66	-	-
Vertex χ^2	80.23	87.28	81.33
Decay distance	97.53	-	-
K-short mass	-	-	34.77
$cos\Theta_H$	84.64	75.90	-
Fisher	1.44	17.66	10.59
$cos\Theta_T$	89.50	59.55	84.95
$cos\Theta_G$	91.34	77.99	96.20
ΔE	2.57	1.61	11.84
Selection	0.007	0.07	0.23

Table 5-8. *Selection efficiency from off-peak events.*

function is given by

$$f(M_{ES}) = A \cdot \left\{ \begin{array}{ll} exp\left(-\frac{(M_{ES}-\mu)^2}{2\sigma^2}\right), & M_{ES} > \mu - \alpha\sigma \\ \frac{(\eta/\alpha)^2 \cdot exp(-\alpha^2/2)}{[(\mu - M_{ES})/\sigma + \eta/\alpha - \alpha]^\eta}, & M_{ES} \leq \mu - \alpha\sigma \end{array} \right\} \tag{5.7}$$

where μ is the mean of the distribution and σ is the width while α and η describe the tail. The shape depends only weakly on η, and for these analyses η was fixed to be twenty. A controls

the relative scaling of the Crystal-Ball to ARGUS shape in the final fit shape. The ARGUS shape is given by

$$f(M_{ES}) = M_{ES}\sqrt{1-\left(\frac{M_{ES}}{M_0}\right)^2}\cdot exp\left(c\left(1-\left(\frac{M_{ES}}{M_0}\right)^2\right)\right)\cdot\theta(M_{ES}<M_0) \quad (5.8)$$

where M_0 is a fixed end-point, 5.29 GeV/c^2 in this case, and c is the ARGUS parameter.

The shape of the Crystal Ball function is fixed by fitting to the M_{ES} distribution of simulated signal events that passed the event selection[1]. The ARGUS shape parameter and the relative scaling between the ARGUS and Crystal Ball (A) are left free to be fixed when the fit to data is performed. The fits are all unbinned maximum log-likelihood fits performed using *RooFit* [48] and are permitted to give negative yields.

5.7.1 Signal Shape

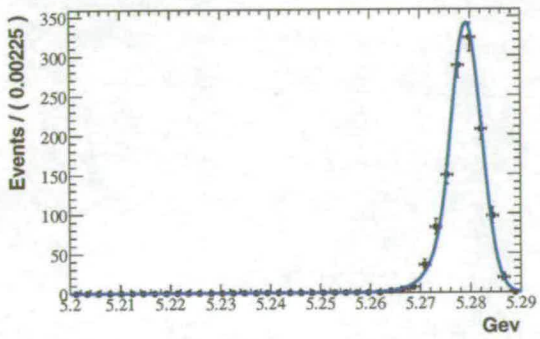

Figure 5-45. *Simulated $B \to \omega\gamma$ events, after event selection, fitted to a Crystal Ball shape.*

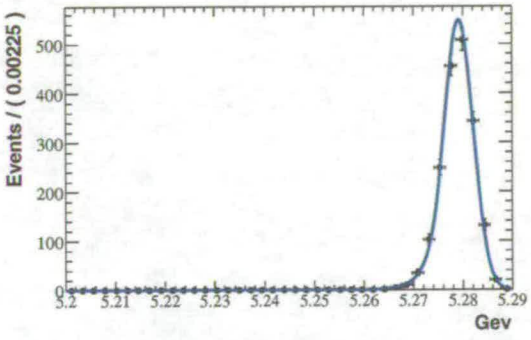

Figure 5-46. *Simulated $B \to \phi\gamma$ events, after event selection, fitted to a Crystal Ball shape.*

Figures 5-45, 5-46 and 5-47 show the simulated signal M_{ES} distribution after all cuts have been applied. Table 5-9 gives the Crystal Ball parameters for each fit. It has been established

Figure	Mode	Mean (μ)	Width (σ)	Tail α
5-45	$B \to \omega\gamma$	5.279	3.059×10^{-3}	1.284
5-46	$B \to \phi\gamma$	5.279	2.949×10^{-3}	1.400
5-47	$B^0 \to \phi K^0_S\gamma$	5.279	2.799×10^{-3}	1.173

Table 5-9. *Crystal Ball parameters for simulated signal fits.*

[1] When these fits are performed A = 1.

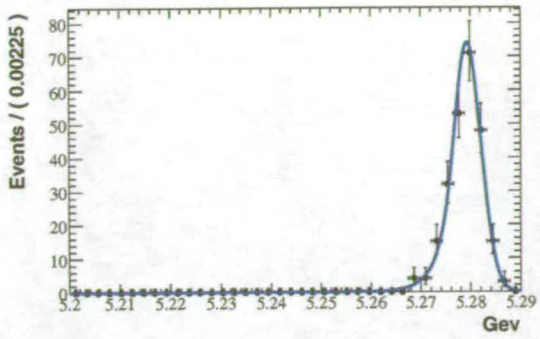

Figure 5-47. *Simulated $B^0 \to \phi K^0_S \gamma$ events, after event selection, fitted to a Crystal Ball shape.*

(for example [49]) that there is a discrepancy in the M_{ES} distribution due to incorrect modelling of the beam energy spread. The mean of the M_{ES} peak is overestimated, and the width is underestimated. By comparing the M_{ES} distributions for the $B \to K^* \gamma$ decay from data and simulation [49], the correction factors are found to be 0.4 MeV for the mean and 22% for the width. These corrections are applied to the fit parameters given in table 5-9 and the corrected parameters are used to fix the Crystal Ball shape used in the data fits.

5.7.2 Data

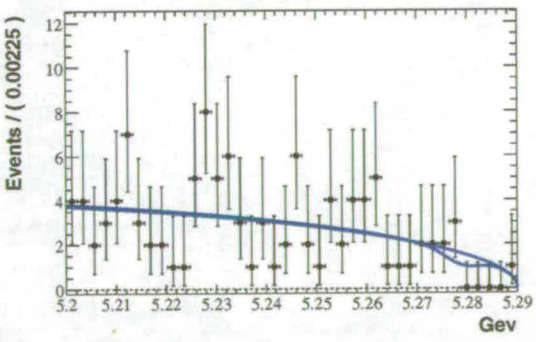

Figure 5-48. *Data passing the $B \to \omega\gamma$ selection criteria, fit to a Crystal Ball plus ARGUS shape.*

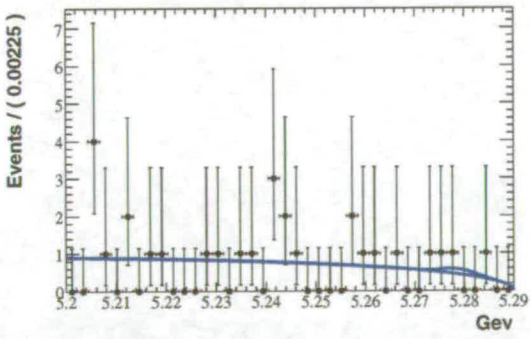

Figure 5-49. *Data passing the $B \to \phi\gamma$ selection criteria, fit to a Crystal Ball plus ARGUS shape.*

Figures 5-48, 5-49 and 5-50 show the M_{ES} distribution of the events selected from data. Fit to each is an ARGUS plus Crystal Ball line shape, where the Crystal Ball parameters have been fixed (section 5.7.1). The resulting ARGUS parameters (c) and signal yields are given in table 5-10. The uncertainties on the signal yeilds are determined by the uncertainties on the relative scaling (A) of the two components of the shape.

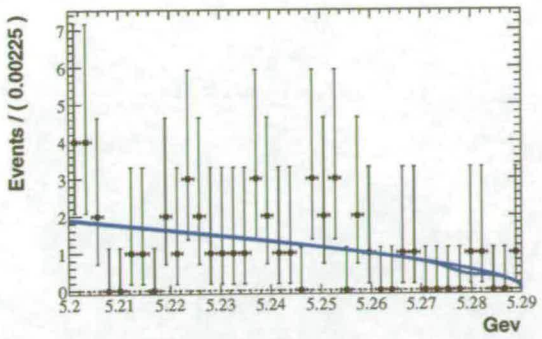

Figure 5-50. *Data passing the $B^0 \to \phi K^0_S \gamma$ selection criteria, fit to a Crystal Ball plus ARGUS shape.*

Figure	Mode	ARGUS parameter (c)	Events in fit region	Signal Yield
5-48	$B \to \omega\gamma$	-5.5 ± 11.0	108	-2.5 ± 3.2
5-49	$B \to \phi\gamma$	-9.8 ± 18.6	28	$+0.6 \pm 2.4$
5-50	$B^0 \to \phi K^0_S \gamma$	$+5.3 \pm 26.4$	47	-0.6 ± 1.8

Table 5-10. *ARGUS parameter and signal yield data fits.*

5.8 Signal Peak Background Estimation

Any non-zero yield listed in table 5-10 will not be entirely signal, some background events may also pass all the selection criteria and contribute to the signal peak. The background contribution to the signal peak can be calculated.

5.8.1 $B \to \omega\gamma$

Figure 5-51 shows the $M_{ES} \times \Delta_E$ distribution of the simulated $B\overline{B}$ and off-peak events that pass the event selection. The two simulated background events lying in the $B \to \omega\gamma$ signal box originated as $B \to K^*\gamma$ and $B^0 \to X_s\gamma(X_s \to K^{*-}\pi^+)$. Since the simulated $B\overline{B}$ sample is composed of many different decay modes, and may only hold a relatively small number of events from either of these decay modes, the event selection is repeated on pure samples of both these modes to gain a more accurate estimation of the number of expected background events. Figure 5-52 shows the $M_{ES} \times \Delta_E$ distribution of simulated $B \to K^*\gamma$ (green open circles) and $B^0 \to X_s\gamma$ (red crosses) events that pass the event selection. The two events from the $B^0 \to X_s\gamma$ sample remaining in the signal box are $X_s \to K^{*-}\pi^+$ and $X_s \to K^{*0}\pi^0$.

Not all the background events passing the selection contribute to the signal peak, some are accounted for in the ARGUS background shape. Simply counting the number lying in the signal box is only a crude approximation of the contribution to the signal peak. To gain a

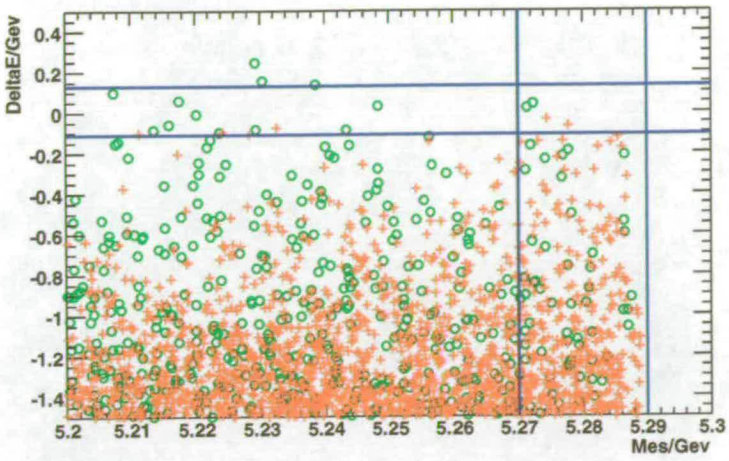

Figure 5-51. *Simulated $B\overline{B}$ events (red crosses) and off-peak data events (green open circles) remaining after $B \to \omega\gamma$ selection cuts have been applied.*

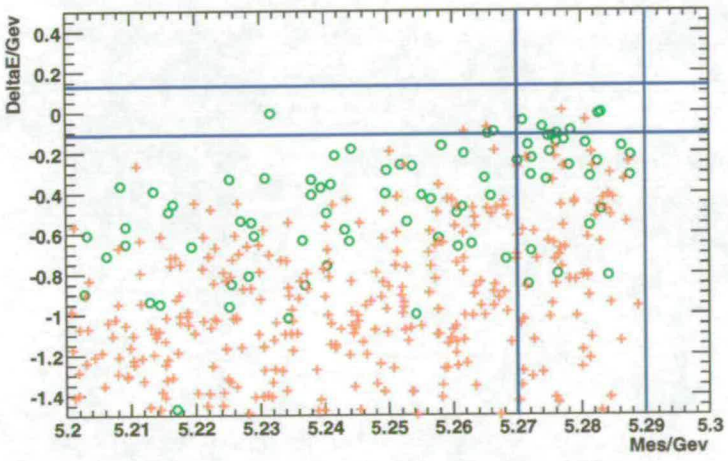

Figure 5-52. *Simulated $B \to X_s\gamma$ events (red crosses) and simulated $B \to K^*\gamma$ events (green open circles) remaining after $B \to \omega\gamma$ selection cuts have been applied.*

more precise measurement of the contribution to the signal yield the background samples are fit with the same shape as the data, with only the relative normalisation parameter allowed to float.

From the fit to the M_{ES} distribution of simulated $B \to X_s\gamma$ events passing the $B \to \omega\gamma$ selection (illustrated in figure 5-53), these events contribute to the ARGUS and Crystal Ball shapes in the ratio 2:1. Similarly, for the $B \to K^*\gamma$ sample the ratio is about 10:7. Using

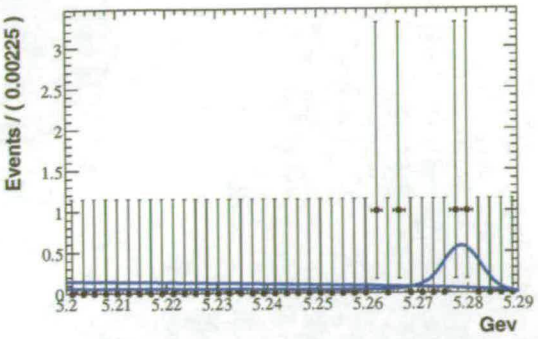

Figure 5-53. *Simulated $B \to X_s\gamma$ events passing the $B \to \omega\gamma$ selection criteria, fit to a Crystal Ball plus ARGUS shape, with the ARGUS shape also shown.*

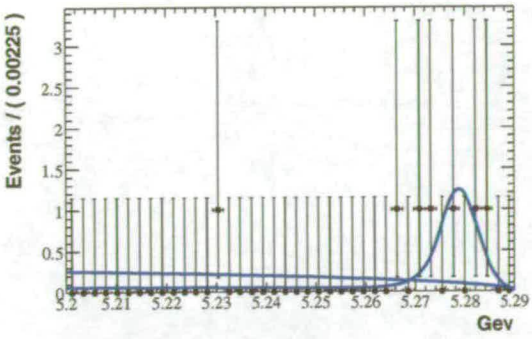

Figure 5-54. *Simulated $B \to K^*\gamma$ events passing the $B \to \omega\gamma$ selection criteria, fit to a Crystal Ball plus ARGUS shape, with the ARGUS shape also shown.*

the branching ratio and initial number of events for each decay, the total number of events in the fit region is scaled to give an estimation of the number of events expected in the fit region from $82\,\text{fb}^{-1}$ of data. After scaling to the correct luminosity, the expected number of

Sample	Initial	Branching Ratio	Scale Factor
$B \to K^*\gamma$	163000	4.2×10^{-5}	2.2×10^{-2}
$B \to X_s\gamma$	148000	4.3×10^{-4}	2.5×10^{-1}

Table 5-11. *Background scale factors for $B \to \omega\gamma$.*

background events for each background sample is given in table 5-12. The total number of background events expected in the signal peak is 0.78 ± 0.22.

Background sample	Events in fit	Expected Contribution
$B \to X_s\gamma$	4	$(3.3 \pm 1.6) \times 10^{-2}$
$B \to K^*\gamma$	7	$(7.5 \pm 2.0) \times 10^{-1}$

Table 5-12. *Signal peak background estimates for $B \to \omega\gamma$.*

The same technique verifies that the off-peak data does not contribute to the signal yield. The two events in the signal box shown in figure 5-51 will be completely contained by the ARGUS part of the shape.

5.8.2 $B \to \phi\gamma$

Neither the simulated $B\overline{B}$ sample, nor the off-peak data indicate any background contribution to the signal yield for $B \to \phi\gamma$.

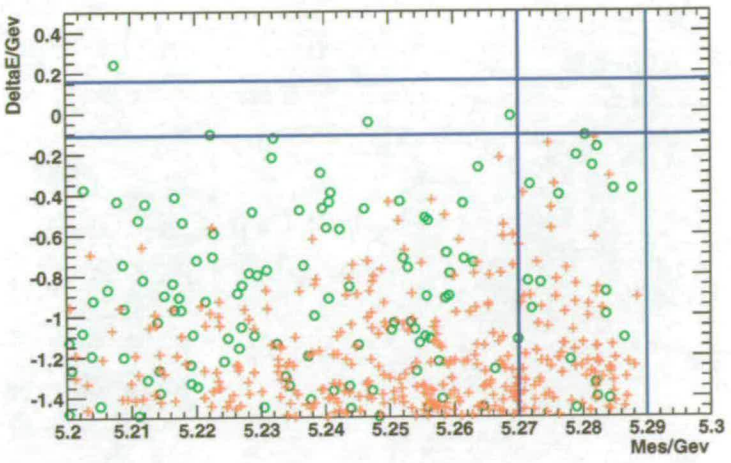

Figure 5-55. *Simulated $B\overline{B}$ (red crosses) and off-peak data (green open circles) events remaining after $B \to \phi\gamma$ selection cuts have been applied.*

5.8.3 $B^0 \to \phi K^0_S \gamma$

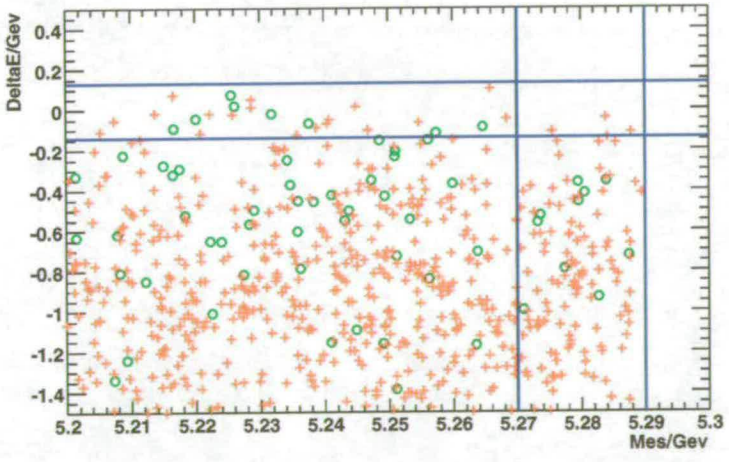

Figure 5-56. *Simulated $B\overline{B}$ (red crosses) and off-peak data (green open circles) events remaining after $B^0 \to \phi K^0_S \gamma$ selection cuts have been applied.*

Figure 5-56 shows the $M_{ES} \times \Delta_E$ distributions of simulated $B\overline{B}$ and off-peak events that pass the $B^0 \to \phi K^0_S \gamma$ event selection. There are three simulated $B\overline{B}$ events that pass all the selection cuts. One of these appears to come from a random combination of decay products from both B mesons. The other two arise from the mis-identification of a neutral meson as a high energy photon, $B \to \overline{K^0}\phi\eta$ and $B \to \phi K^0 \pi^0$. Since neither of these modes have been

exclusively simulated, the only guide to the number of expected background events comes from the generic $B\overline{B}$ sample.

The estimation of background contribution to the signal peak proceeds in a similar manner to that for $B \to \omega\gamma$. The expected number of background events, scaled to the correct luminosity, is given in table 5-13.

Background sample	Events in fit	Scale Factor	Expected Contribution
$B\overline{B}$	27	0.86	2.2 ± 0.9

Table 5-13. *Signal peak background estimates for* $B^0 \to \phi K_s^0\gamma$.

5.8.4 Branching Ratio Upper Limit

Given the signal yields from the selected data samples (table 5-10), it is clear that no significant signal has been observed in any of the modes so an upper limit to the branching fraction must be calculated rather than the branching fraction itself. A number of events, N, is found for which the probability that no signal would be observed, when in fact more than N events occurred, is less than 10%. The probability of observing n_0 events when N events occurred when λ background events were expected is given by equation 5.9 [39].

$$\epsilon(N) = \frac{e^{-(\lambda+N)} \sum_{n=0}^{n_0} \frac{(\lambda+N)^n}{n!}}{e^{-(\lambda)} \sum_{n=0}^{n_0} \frac{(\lambda)^n}{n!}} \tag{5.9}$$

The expected background, λ, is estimated by integrating the ARGUS functions described by table 5-10 over the full-width half-maximum of the signal peaks, that is over the range $5.283\,\text{GeV} < M_{ES} < 5.274\,\text{GeV}$ for all three modes. The number of observed events, n_0, is found by counting the number of events over the same range. This results in the 90% confidence level upper limits on the signal yield for each mode given in table 5-14. Using

Mode	Expected Background	Observed events	Upper Limit
$B \to \omega\gamma$	6.5	5	4.4
$B \to \phi\gamma$	1.7	3	5.2
$B^0 \to \phi K_s^0\gamma$	2.4	2	3.3

Table 5-14. *90% confidence level intervals for the Poisson signal mean, for all modes.*

the yield upper limits, y, from table 5-14; the selection efficiency, e, from table 5-6; the branching ratio for the chosen vector meson decay mode, b, which is $\mathcal{B}(\phi \to K^+K^-) = 0.492$ or $\mathcal{B}(\omega \to \pi^+\pi^-\pi^0) = 0.891$ [9] and the number of B mesons used for the analysis, n $= 88.887 \times 10^6$; the upper limits on the branching ratios for the three modes, U, can be found using the equation

$$U = \frac{y}{bne} \tag{5.10}$$

and the results are given in table 5-15. These upper limits will be increased by the systematic

Mode	Branching Fraction Upper Limit
$B \to \omega\gamma$	2.8×10^{-6}
$B \to \phi\gamma$	2.7×10^{-6}
$B^0 \to \phi K_s^0\gamma$	3.5×10^{-6}

Table 5-15. *Branching Fraction Upper Limits (90% confidence level).*

uncertainties calculated in the next section to give the final results shown in the conclusion to this chapter.

5.9 Systematic Uncertainties

Many of the systematic uncertainties associated with these analyses are common with other radiative penguin analyses. Indeed, some of these systematics have been exhaustively studied by specialised working groups. Where possible, this thesis builds on earlier work by other collaboration members and simply quotes the values calculated previously. Specifically, the common systematic uncertainties applicable to radiative Penguin studies are captured in [49] - [52]. The systematic uncertainties are combined with the upper limits calculated in section 5.8.4 by simply increasing the upper limit by the uncertainty.

Uncertainty (%)	$B \to \omega\gamma$	$B \to \phi\gamma$	$B^0 \to \phi K_s^0\gamma$
Vector Meson Mass	2.9	0.7	1.7
Photon Efficiency	1.3	1.3	1.3
Energy Scale	1.5	1.5	1.5
Energy Resolution	3.0	3.0	3.0
Neutral Pion Efficiency	2.6	-	-
Tracking Efficiency	2.4	2.6	2.6
K-short Efficiency	-	-	4.5
Particle Identification	2.0	1.4	1.4
B Counting	1.1	1.1	1.1
Total	7.7	6.6	6.8

Table 5-16. *Systematic uncertainties (%) for all modes.*

5.9.1 Vector Meson Mass Cut

The vector meson mass peak is dominated by experimental resolution[2]. Since this variable is cut on during the event selection, any discrepancy between simulated mesons and real mesons

[2]This is more true for the ϕ meson than the ω, but is the basis for estimating this systematic

measured in data must be accounted for in the systematic uncertainty. The widths and means

Sample	Peak (MeV/c^2)	Width (MeV/c^2)
Simulated Omega	783.2	9.27
Data Omega	783.2	10.15
Simulated Phi	1019.3	2.19
Data Phi	1019.5	2.76

Table 5-17. *Peak and width for vector meson mass distributions in simulation and data.*

of the mass peaks for omega and phi mesons in simulation and real data are given in table 5-17. The absolute mass cuts used in these analyses can be expressed in terms of the mean and the width of the mass peak, as shown in table 5-18. Assuming a Gaussian signal shape, this representation permits a calculation of the cut efficiency in data and simulated signal. The difference is the systematic uncertainty. The uncertainty on the phi modes is significantly

Mode	Data Cuts (σ)	Simulation Cuts (σ)
$B \to \omega\gamma$	-2.20, +1.60	-2.37, +1.72
$B \to \phi\gamma$	-3.12, +2.72	-4.05, +3.31
$B^0 \to \phi K_S^0\gamma$	-3.30, +3.00	-4.28, +3.67

Table 5-18. *Peak and width for vector meson mass distributions in simulation and data.*

lower than that of the omega mode because the phi mass cuts are much looser, when expressed in terms of the width of the mass peak; typically over 3 σ. This effect is partly caused by the narrowness of the phi peak, but the cuts are also looser because there is less combinatoric background to the phi modes (see section 5.6.3).

5.9.2 Neutral Systematics

The event selection for all three modes presented in this thesis begins with a series of criteria to be applied to the highest energy photon in the event (section 5.4). Following this, the reconstruction of the omega candidates in the $B \to \omega\gamma$ mode takes a list of neutral pion candidates as input. The selection criteria applied to these candidates are a source of systematic uncertainties in the selection efficiencies for these modes. The radiative penguin and neutrals working groups have spent considerable effort quantifying these uncertainties.

There are three systematic uncertainties that make a significant contribution to the overall uncertainty: the photon efficiency, the photon energy scale and the photon energy resolution. The photon efficiency is evaluated by comparing tau decays producing one or two neutral pions in data and simulation. The uncertainty in photon efficiency also leads directly to the neutral pion efficiency uncertainty quoted in table 5-16.

An inaccurate simulation of the photon energy will give an inaccurate calculation of the efficiency of the ΔE cut. Symmetric eta meson decays are used to measure the uncertainty in the energy scale. Symmetric decays are those in which both photons from the decay are within the same energy range. Minimal selection cuts are applied to the photons to maximise statistics and minimise bias. A minimum distance between the photons is required for lower energy samples, but relaxed for high energy photons where the two photons are kinematically constrained to be close. A second moment cut is also applied to remove merged neutral pions from the sample. Samples of symmetric eta mesons are then produced from data and simulated $B\overline{B}$ events. Differences in the measured eta masses for each photon energy range give a measure of the uncertainty on the energy scale for each range. The largest uncertainty is taken as the energy scale uncertainty. Given the uncertainty in the photon energy scale, the effects of this uncertainty on the signal efficiency are quantified by shifting the photon energy in the simulation and repeating the selection.

The same samples of eta mesons, and similar samples of symmetric neutral pion decays are used in the study of photon energy resolution. Differences in the widths of the mass peaks are caused by inaccurate modeling of the photon energy resolution in the simulation. The effect of the degradation of the resolution are examined by smearing the reconstructed energy of the photon in the simulation with a Gaussian distribution. The systematic on the selection efficiency comes from the change in selection efficiency with the smearing.

5.9.3 Tracking And Particle Identification Systematics

The tracking efficiency is provided by the *BABAR* tracking group. The efficiency is found by identifying tracks in the SVT and observing the fraction of these that are well reconstructed in the DCH. The systematic for the tracking efficiency has been found to be 1.2% for each charged pion in the event, and 1.3% for each charged kaon in the event.

The kaon identification has been extensively studied by the charged hadron ID group. The uncertainty resulting from the kaon PID in the DRC is derived from a sample of charged kaons kinematically selected in $D^{*+} \to D^0\pi^+, D^0 \to K^-\pi^+$ decays. These kaons are used to calculate the efficiency of cuts for true charged kaons as a function of momentum and dip angle. The efficiencies are found for both simulated and real events and compared to give the systematic uncertainty.

The use of the `notAPion` selector to identify obvious pions in the $B \to \omega\gamma$ analysis (section 5.5.1) is somewhat non-standard, but it has been used for other radiative Penguin analyses [52]. These other analyses have quantified the systematic error from the charged pion identification in the same manner as the charged kaons, using the charged pions from $D^{*+} \to D^0\pi^+, D^0 \to K^-\pi^+$ decays.

The systematic for the K-short efficiency is actually an additional systematic arising from tracking as it pertains to K-short reconstruction. Two samples of K-shorts are collected from data and simulation, one with a momentum cut $p < 1\,\text{GeV}$ and the other with no cuts. An

efficiency correction is calculated for each sample and the systematic uncertainty on the K-short efficiency is taken as the difference between the two efficiency corrections.

5.9.4 B Counting

The number of B mesons present in the data sample used in an analysis can be found from the data collection using a standard *BABAR* script, which is based on the approved *BABAR* B counting technique [53]. This same script provides the systematic and statistical uncertainties from the counting process. In summary, the B counting process compares the number of hadronic events in both on- and off-resonance data. Assuming that the increase in the ratio of hadronic events to muon pairs between the two samples is due to $\Upsilon(4S)$ production, the number of $\Upsilon(4S)$ mesons can be counted.

5.10 Chapter summary

The searches for three radiative Penguin decay modes, $B \to \omega\gamma$, $B \to \phi\gamma$ and $B^0 \to \phi K_S^0\gamma$ have been presented. No significant signal has been found in 82 fb^{-1} of data collected by the *BABAR* detector. Upper limits on the branching ratios, $\mathcal{B}$, were found to be $\mathcal{B}(B \to \omega\gamma) < 3.0 \times 10^{-6}$, $\mathcal{B}(B \to \phi\gamma) < 2.9 \times 10^{-6}$, and $\mathcal{B}\left(B^0 \to \phi K_S^0\gamma\right) < 3.8 \times 10^{-6}$, at the 90% confidence level with the systematic uncertainties included.

6

Conclusions

6.1 Calculation of Limit on Wolfenstein Parameters ρ and η

As part of the motivation for studying radiative one-loop decays it was shown (section 4.6) that the Wolfenstein parameters ρ and η could be related and constrained through the equation

$$\frac{\Gamma\left(B \to \omega\gamma\right)}{\Gamma\left(B^0 \to K^*\gamma\right)} = \kappa_d \lambda^2 \left[(1-\rho)^2 + \eta^2\right] \left(1 + \Delta\left(R_{L/S}\right)\right) \tag{6.1}$$

It was shown that for neutral B meson decays long-distance effects were of the order 2%, so for this calculation $\Delta\left(R_{L/S}\right)$ is taken to be zero.

At that time equation 6.1 was used, along with the branching ratio $\mathcal{B}\left(B^0 \to K^*\gamma\right) = (4.23 \pm 0.63) \times 10^{-5}$ [42] to predict the branching ratio for $B \to \omega\gamma$ to be $(0.6 \pm 0.4) \times 10^{-6}$, which is below the upper limit found in chapter 5. The calculation can be reversed and the measured upper limit, 3.7×10^{-6}, can be used to constrain ρ and η. Using the central value of the permitted range for $\lambda = 0.2225$ and the calculated value for $\kappa_d = 0.29$ (equation 4.33) equation 6.1 becomes an inequality, restricting ρ and η to an ellipse on the $\rho \times \eta$ plane.

$$(1-\rho)^2 + \eta^2 < 6.1 \tag{6.2}$$

This implies that $|V_{td}|$ is required to be less than 0.0276, which is not an improvement on the existing measurement of $|V_{td}| = 0.009 \pm 0.005$ [9].

6.2 Summation

This thesis is split into two distinct, yet equally important portions. The first half is dedicated to a description of the *BABAR* detector, focusing on the Data Acquisition system. This description leads to a discussion of the design, development and deployment of VMON, an application to monitor the Data Acquisition system. VMON has been instrumental to the process of upgrading the *BABAR* Data Acquisition system to handle the very high instantaneous luminosity of PEP-II, now more than twice the design luminosity, and has proved invaluable for isolating faults in the Data Acquisition system. Designers of future Data Acquisition systems, which will be even more powerful and complex than that of *BABAR*, would do well to build the kind of detailed monitoring provided by VMON into their systems from the outset.

The second half of this thesis describes the search for the exclusive radiative one-loop decays, $B \to \omega\gamma$, $B \to \phi\gamma$ and $B^0 \to \phi K_S^0\gamma$, using a sample of 89 million $B\overline{B}$ events collected by the *BABAR* detector. No significant signal is seen in any of the channels. Upper limits on the branching ratios, $\mathcal{B}$, were found to be $\mathcal{B}(B \to \omega\gamma) < 3.0 \times 10^{-6}$, $\mathcal{B}(B \to \phi\gamma) < 2.9 \times 10^{-6}$, and $\mathcal{B}\left(B^0 \to \phi K_S^0\gamma\right) < 3.8 \times 10^{-6}$, at the 90% confidence level.

The upper limit for $B \to \omega\gamma$ compares favourably with the limits set by the BELLE (4.4×10^{-6}) [54] and CLEO (9.2×10^{-6}) [55] collaborations. This upper limit approaches the region where it begins to limit the range of permitted values for the CKM matrix elements within the Standard Model. In scenarios beyond the Standard Model these results already provide significant constraints. As the *BABAR* detector continues to acquire data at an impressive rate, it is anticipated that $B \to \omega\gamma$ and $B^0 \to \phi K_S^0\gamma$ will be observed soon, providing additional constraints on the CKM matrix elements. Of course, it is always possible that the measured branching ratios will be incompatible with the Standard Model and the existing experimental constraints. Some form of New Physics would then be required to explain them.

A

Fisher Discriminant

A.1 Two-Dimensional Fisher : Pictorial Example

In a typical cut-and-count analysis distributions of single variables are used in the selection criteria. Occasionally groups of correlated variables can be used to distinguish background and signal events, as shown in figure A-1. Projecting the distributions onto a line across the plane reduces the two-dimensional problem to one dimension; simultaneously improving the separation between the two classes.

A.2 Derivation of an N-Dimensional Fisher

The Fisher discriminant, $\mathcal{F}$[56], is a linear combination of the original n variables, x_i,

$$\mathcal{F} = \sum_{i=1}^{n} \alpha_i \cdot x_i = \alpha \cdot x \tag{A.1}$$

Each of the two samples of events, signal (S) and background (B), are described by a set of n-dimensional vectors, s_k and b_k respectively. There is one vector for each event in the sample and the samples contain n_S and n_B vectors respectively. Note that there is no requirement $n_S = n_B$.

The two sets of events produce two sets of Fisher values

$$\mathcal{F}(S)_k = \alpha \cdot s_k \qquad \mathcal{F}(B)_k = \alpha \cdot b_k \tag{A.2}$$

which will combine to form a distribution with two peaks. The objective is to separate the two samples. Good separation occurs if the distance between the peaks is large when compared to their widths; when

$$D = \frac{\left(\bar{\mathcal{F}}(S) - \bar{\mathcal{F}}(B)\right)^2}{\sigma_s^2 + \sigma_b^2} \tag{A.3}$$

is large, σ_s and σ_b are the widths of the signal and background samples respectively. Maximising D, by requiring that its derivative is zero, provides the criteria for the calculation of α.

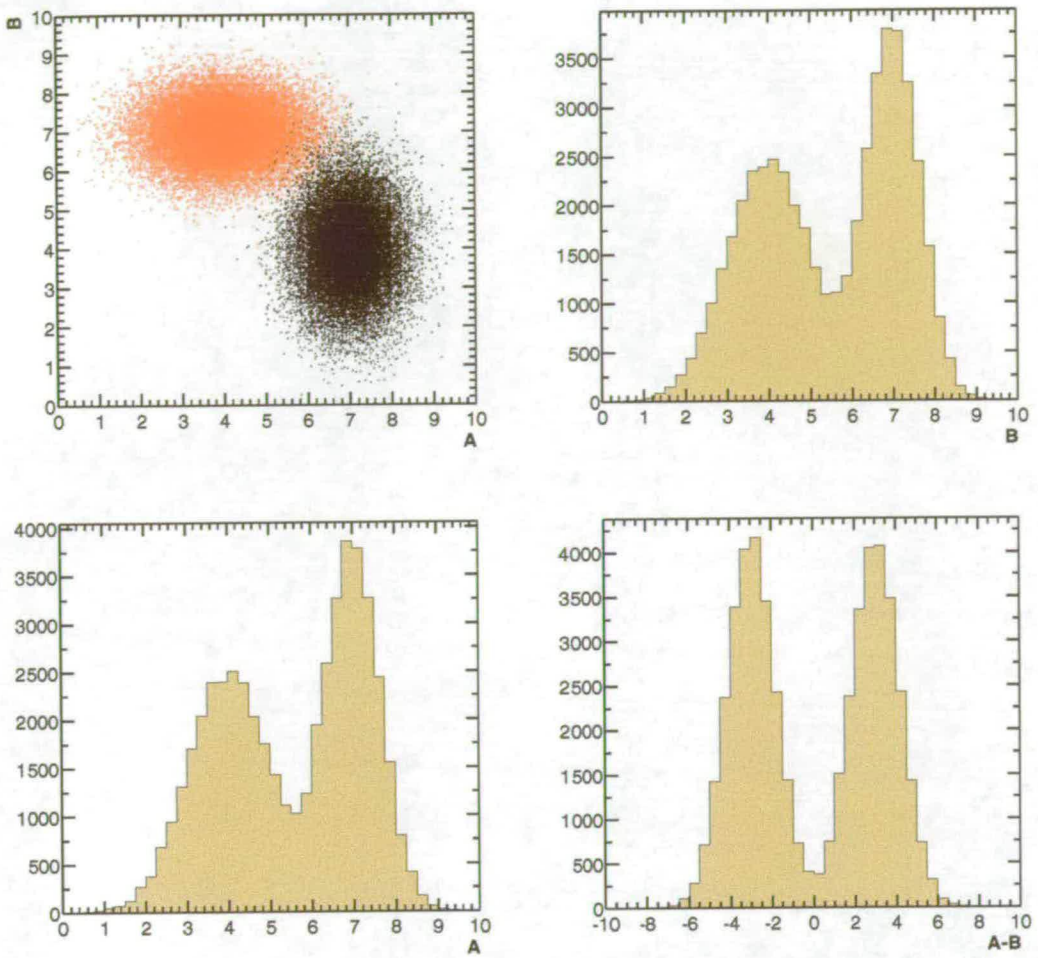

Figure A-1. *Illustration of a simple two dimensional fisher. Two classes of events are shown as two cluster on a two dimensional plane. The projections of these distributions onto each of the axes shows some separation but also considerable overlap. When the distribution is projected onto a line other than one of the axes, the separation is much improved.*

The means of the two Fisher peaks are,

$$\bar{\mathcal{F}}(S) = \alpha^T \cdot \bar{s} \qquad \bar{\mathcal{F}}(B) = \alpha^T \cdot \bar{b} \tag{A.4}$$

which leads to the difference of means

$$\bar{\mathcal{F}}(S) - \bar{\mathcal{F}}(B) = \alpha^T \cdot (\bar{s} - \bar{b}) \tag{A.5}$$

The widths of the two samples are given by

$$\sigma_s^2 = \sum_{k=1}^{n_s} \frac{\left(\mathcal{F}_k(S) - \bar{\mathcal{F}}(S)\right)^2}{n_s} \qquad \sigma_b^2 = \sum_{k=1}^{n_b} \frac{\left(\mathcal{F}_k(B) - \bar{\mathcal{F}}(B)\right)^2}{n_b} \tag{A.6}$$

The width can be written in matrix form, clarifying the α dependency

$$\sigma^2 = \sum_k \frac{[\alpha^T \cdot x_k - \alpha^T \cdot \bar{x}]^2}{n} = \sum_k \alpha^T \frac{(x_k - \bar{x})(x_k - \bar{x})^T}{n} \alpha = \alpha^T U \alpha \tag{A.7}$$

where the matrix U is the width matrix for the sample:

$$U = \sum_k \frac{(x_k - \bar{x})(x_k - \bar{x})^T}{n} \tag{A.8}$$

Putting this into equation A.3 gives

$$D = \frac{\alpha^T (\bar{s} - \bar{b})(\bar{s} - \bar{b})^T \alpha}{\alpha^T (U(S) + U(B)) \alpha} = \frac{\alpha^T B \alpha}{\alpha^T U \alpha} \tag{A.9}$$

Applying the requirement

$$\frac{\partial D}{\partial \alpha} = 0 \tag{A.10}$$

the yields

$$(\alpha^T U \alpha) B \alpha = (\alpha^T B \alpha) U \alpha \tag{A.11}$$

or

$$B\alpha = \lambda U \alpha \tag{A.12}$$

with $\lambda = \alpha^T B \alpha / \alpha^T U^{-1} \alpha$. Therefore

$$U^{-1} B \alpha = \lambda \alpha \tag{A.13}$$

This is an eigenvalue problem, and since B has the special structure $B = (\bar{s} - \bar{b})(\bar{s} - \bar{b})^T$, there exists one, and only one, nonzero eigenvalue with corresponding eigenvector

$$\alpha = U^{-1}(\bar{s} - \bar{b}) \tag{A.14}$$

References

[1] Anicius Manlius Severinus Beothius. *If you had kept quiet, you would have remained a philosopher.* Consolation of Philosophy, (526).

[2] V.L. Fitch J.H. Christenson, J.W. Cronin and R. Turlay. *Phys. Rev. Lett.*, 13(1964):138.

[3] The BABAR Collaboration. Observation of CP violation in the B^0 meson system. *Phys. Rev. Lett.*, 87(2001):091801.

[4] The BELLE Collaboration Observation of Large CP Violation in the Neutral B Meson System. *Phys. Rev. Lett.*, 87(2001):091802.

[5] A. D. Sakharov. *Journal of Exp. and Theor. Phys.*, 5(1967):24.

[6] G. C. Branco, L. Lavoura, J. P.Silva. CP Violation. *Oxford Univ. Press*, (1999).

[7] The BABAR Collaboration. The BABAR Detector. *Nucl. Instrum. Meth.*, A479(2002):1.

[8] D. Boutigny et al. BaBar technical design report. SLAC-R-0457.

[9] K. Hagiwara *et al.*. Review of particle physics. *Phys. Rev.*, D66(2002):010001.

[10] PEP-II: An Asymmetric B Factory. Conceptual Design Report(1993).

[11] P. J. Oddone. Linear Collider $B\overline{B}$ Factory Conceptual Design. In D. Stork, editor, *Proceedings of the UCLA Workshop*, page 243. World Scientific(1987).

[12] P. Clark. The BABAR Light Pulser System. *The University of Edinburgh, Ph.D. Thesis*, (2000).

[13] W. R. Stevens. UNIX Network Programming. *Prentice-Hall*, (1998).

[14] W. R. Stevens. Advanced Programming in the UNIX Environment. *Addison-Wesley*, (1993).

[15] R. Brun, F. Rademakers, N. Bunicic, V. Fine, P. Canal, S. Panacek. ROOT, An Object-Oriented Data Analysis Framework *http://root.cern.ch*

[16] H. Höcker, H. Lacker, S. Laplace, F. Le Diberder. A New Approach to a Global Fit of the CKM Matrix. *Eur. Phys. J.*, C21(2001):225.

[17] K. Lingel, T. Skwarnicki, J. Smith. Penguin Decays of B Mesons *hep-ex/9804015v1*, April 1998.

[18] J. L. Hewett, J. D. Wells. Searching for supersymmetry in rare B decays. *hep-ph/9610323v1*, October 1996.

[19] G. Buchalla, A. Buras, M. Lautenbacher. Weak decays beyond leading logarithms. *Rev. Mod. Phys.* 68(1996), No.4.

[20] A. Ali. Theory of rare B decays. *hep-ex/9709507v3*, October 1997.

[21] A. Ali, V. Braun, H. Simma. Exclusive Radiative B-Decays in the Light-Cone QCD Sum Rule Approach. *hep-ex/9401277*, January 1994.

[22] A. Ali, V. Braun. *Phys. Lett.*, B359(1995):223.

[23] S. Bosch, G. Buchalla. The Radiative Decays $B \to V\gamma$ at Next-to-Leading Order in QCD. *hp-ph/0106081v1*, June 2001.

[24] A. Buras, A. Kwiatkowski, N. Pott. On the Scale Uncertainties in the $B \to X_s\gamma$ Decay. *hep-ph/9707482v3*, April 1998

[25] A. Ali, A. Parkhomenko. Branching Ratios for $B \to K^*\gamma$ and $B \to \rho\gamma$ Decays in Next-to-Leading Order in the Large Energy Effective Theory. *hep-ph/0105302v3*, December 2001.

[26] T. Hurth, T Mannel. Direct CP Violation in Radative B Decays. *hep-ph/0109041v1*, September, 2001.

[27] M. Benke, T. Feldmann, D. Seidel Systematic approach to exclusive $B \to Vl^+l^-, V\gamma$ decays. *hep-ph/0106067v2*, July 2001.

[28] J. F. Donoghue, E. Golowich, A. A. Petrov. Final state rescattering as a contribution to $B \to \rho\gamma$ *Phys. Rev.*, D55(1997):2657.

[29] K. Chetyrkin, M. Misiak, M. Münz. Weak Radiative B meson Decay Beyond Leading Logarithms. *hep-ph/9612313v3*, February 1998.

[30] The *BABAR* Collaboration. Measurement of the Branching Fraction for Inclusive Semileptonic B Meson Decays. *Phys. Rev.* D67(2003):031101.

[31] T. Hurth, E. Lunghi. On Exclusive and Inclusive Rare B Decays: CKM Phenomenology and New Physics Reach. *hep-ph/0307142v1*, July 2003.

[32] The CLEO Collaboration. First Measurement of the Rate of the Inclusive Radiative Penguin Decay $B \to X_s\gamma$ *Phys. Rev. Lett*, 74(1995):2885.

[33] The ALEPH Collaboration. A Measurement of the Inclusive $b \to s\gamma$ Branching Ratio. *Phys. Lett.*, B429(1998):169.

[34] The BELLE Collaboration. A Measurement of the Branching Fraction for the Inclusive $B \to X_s\gamma$ Decays with BELLE. *Phys. Lett.*, B511(2001):151.

[35] The CLEO Collaboration. Branching Fraction and Photon Energy Spectrum for $b \to s\gamma$. *Phys. Rev. Lett*, 87(2001):251807.

[36] The *BABAR* Collaboration. Determination of the Braching Fraction for Inclusive Decays $B \to X_s\gamma$. 31^{st} International Conference on High Energy Physics(2002), Amsterdam.

[37] The *BABAR* Collaboration. $b \to s\gamma$ Using a Sum of Exclusive Modes. *hep-ex/0207074v1*, July 2002.

[38] S. Playfer. Radiative Penguin Decays. *hep-ex/0308004v1*, August 2003.

[39] S. Playfer. Private Communication. June 23, 2003.

[40] The BELLE Collaboration. Measurement of the $B \to K^*\gamma$ Branching Fractions and Asymmetries International Europhysics Conference of High Energy Physics(2003), Aachen.

[41] S. Playfer. Private Communication. July 18, 2003.

[42] The *BABAR* Collaboration. Measurement of $B \to K^*\gamma$ Branching Fractions and Charge Assymetries. *Phys. Rev. Lett.*, 88(2002):101805.

[43] A. Kagan, M. Neubert. *Euro. Phys. Jour. C*, 7, 5(1999).

[44] G. Mancinelli, S. Spanier. Kaon Selection at the *BABAR* experiment. *BABAR Analysis Document*, # 116v1, July 2001.

[45] The *BABAR* Collaboration. The *BABAR* Vertexing. *BABAR Analysis Document*, # 102v6, December 2001.

[46] ARGUS Collaboration. *Phys. Lett.*, B185(1987):218.

[47] S. Playfer. Private communication. August 4, 2003.

[48] W. Verkerke, D. Kirkby. http://roofit.sourceforge.net/

[49] *BABAR* Radiative Penguin Analysis Working Group. Measurement of $\mathcal{B}(B \to K^*\gamma)$ and Search for Direct CP Violation. *BABAR Analysis Document*, # 33v16, September 2001.

[50] F. Di Lodovico, S. Playfer, C. Jessop, Q. Guo, R. Schmitz, J. Tinslay. Measurment of Inclusive Rate $b \to s\gamma$ using the Sum of Exclusive Modes. *BABAR Analysis Document*, # 128v4, April 2000.

[51] F. Di Lodovico, A. Eichenbaum, E. Grauges, S. Playfer, T. Pulliam, J. Tinslay. Study of $b \to s\gamma$ using the Sum of Exclusive Modes. *BABAR Analysis Document*, # 220v15, July 2002.

[52] M. Convery, C. Jessop, H. Tanaka. Search for the Exclusive Radiative Decays $B \to \omega\gamma$ and $B \to \rho\gamma$. *BABAR Analysis Document*, # 354v11, January 2003.

[53] C. Hearty. Measurement of the Number of $\Upsilon(4S)$ Mesons Produced in Run 1 (B Counting). *BABAR Analysis Document*, # 134v1, January 2001.

[54] F. Di Lodovico. $\rho(K^*)\gamma, b \to d(s)\gamma$ Flavour Physics and CP Violation(2003), Paris.

[55] The CLEO Collaboration Study of Exclusive Radiative B meson decays. *Phys. Rev. Lett*, 84(2000):5283.

[56] R. A. Fisher. The use of multiple measurements in taxonomic problems. *Annals of Eugenics*, 7(1936):179.